Development of Flexible Ceramic Nanofiber Membranes for Energy and Environmental Applications

Muhammad Zobayer
Bin Mukhlish

March 2018

Graduate School of Science and Engineering

Kagoshima University

Japan

Development of Flexible Ceramic Nanofiber Membranes for Energy and Environmental Applications

（エネルギー及び環境応用のためのフレキシブル・セラミック・ナノファイバ膜の開発）

Thesis Submitted to Kagoshima University for the Award of the Degree of Doctor of Philosophy in Engineering

By

Muhammad Zobayer Bin Mukhlish

Supervisor: Prof. Dr. Yuji Horie

March 2018

Graduate School of Science and Engineering

Kagoshima University

Japan

ABSTRACT

The electrospinning technique has attracted a great attention because it is relatively simple and versatile method for producing continuous nanofibers (NFs) with unique properties. These NFs have a wide range of applications in various fields. In this thesis, we have developed a series of novel experimental techniques for the fabrication of electrospun ceramic NFs of different morphology with the aim of using them to flexible electronics or decontamination of organic dye from aqueous solution.

For the realization of flexible electronics, we have proposed a nonwoven mat of inorganic electrospun NFs of amorphous silica that is flexible and heat-resistive as a candidate to replace a glass or plastic substrate. We attempted to add electrical conductivity using indium tin oxide (ITO) to create self-standing, nonwoven flexible mats completely composed of inorganic ceramic materials. Two methods were tested to make the ITO-silica NF mats: electrospun silica-NF mats drop-coated by ITO and hybrid mats composed of ITO NFs and silica NFs fabricated by the dual-spinneret electrospinning technique. Our produced ITO-silica NF mats exhibited both mechanical flexibility and thermal stability, even after the heat treatment at 450–650 $^{\circ}$C. The sheet resistance was 15–113 Ω/sq. We attempted to apply the obtained nonwoven conductive mats to the flexible photoanode of dye-sensitized solar cells (DSSCs) and highlighted the problems in the existing application. However, these inorganic NF mats are expected to be excellent candidates to replace thick, heavy and rigid glass substrates, particularly in the field of flexible electronics.

For the purification of dye contaminated water, we have proposed flexible and self-standing membranes composed of electrospun alumina-silica NFs or alumina-silica/iron oxide core-sheath NFs. The hierarchical architecture of the membranes exhibiting high surface area and suitable pore-size distribution will provide sufficient active sites for the adsorption of dye, and the freestanding flexible nature of the membranes will contribute to the easy separation from water. The membranes were used as adsorbent for the removal of Reactive Red-120 (RR-120) dye from an aqueous system. Batch sorption experiments were carried out changing pH, adsorbent dosage and contact time. Furthermore, the kinetics and isotherm studies were also investigated. The sorption process was pH dependent and followed the Langmuir isotherm model. The maximum sorption capacity of the membrane was 1860.81 mg/g, which was several folds higher than the adsorption capacity of a number of recently studied potential adsorbents. Moreover, most of the dyes could be recovered from the dye-loaded membranes after adsorption, and the membranes could be reused as adsorbent.

The sorption kinetics was found to follow the intraparticle diffusion model. The high adsorption performance, excellent flexibility, easy recovery, and reuse characteristics of the membranes all favor their practical application in environmental remediation.

TABLE OF CONTENTS

CHAPTER 1

INTRODUCTION

1.1 Background of the Study

Energy and water are two inseparable commodities that govern the lives of humanity and promote civilization (Kalogirou 2005). As global population growth and standards of living for people continue to increase, clean and sustainable energy generation along with environmental concerns have emerged as the paramount issues and challenges for the mankind over the past decade. The worldwide concern regarding climate change and global warming can largely be attributed to the enormous amount of carbon dioxide gas released to the atmosphere mainly due to the burning of fossil fuels. The exponential energy demand (Uddin et al. 2013) is leading to increased installation of fossil fuel (such as oil, coal or gas) based power generating systems. Consequently, the limited resources of fossil fuel have been decreasing at an alarming rate together with high emission of greenhouse gases. Due to these factors such as the increasing energy requirement in the near future, the greenhouse effect and the approaching exhaustion of conventional energy resources, we will be forced to seek environment-friendly and cost-effective alternative renewable energy resources.

Among various renewable resources (such as solar, geothermal, wind, hydro and biomass), solar energy is a promising option which could be converted directly into electricity through solar cell. Moreover, the amount of attainable solar energy is much higher than the wind energy or biomass (Lewis 2007). Now a days, silicon based solar cells is dominating the photovoltaic market. However, the present cost of electricity from standard silicon-based photovoltaic cells is much higher than the current commercial prices of electricity generated by hydraulic power, nuclear and fossil fuels (Uddin et al. 2013). Therefore, it is necessary to develop efficient solar cells with low manufacturing cost. Dye-sensitized solar cell (DSSC) composed of transparent conductive oxide (TCO) substrate, semiconductor electrode, sensitizing dye and electrolyte has attracted worldwide attention and ranked as one of the promising candidates because of its low material and fabrication cost. Usually, TCO coated glass and plastic sheets, or metallic plates are used as conductive substrate in DSSC. However, lightweight and flexible substrates are desirable for cost-effective roll-to-roll production and also for fabricating the solar cell suitable for installing on curved surfaces or any other existing building structures. But glass substrates are heavy, rigid

and still expensive (Miettunen et al. 2012), whereas metallic substrates are flexible but unstable due to corrosion effect (Mehmood et al. 2014). The lightweight plastic substrates, on the other hand, are flexible, but they are unstable at high temperature (~450 °C) required to gain high quality photoelectrode. In this regard, we have developed mechanically flexible inorganic electrospun nanofiber (ES-NF) mats of ceramic materials such as indium tin oxide-silica (ITO-silica), suitable for application in DSSC as conductive, lightweight and thermally stable substrates.

Water is as important as energy for the development of good standards of life. However, rapid industrial growth and the worldwide population explosion have resulted in a large escalation of demand for fresh water, both for the household needs and for crops to produce adequate quantities of food. Added to this is the problem of pollution of rivers and lakes by industrial wastes containing a number of pollutants (Kalogirou 2005). One of the important classes of pollutants is dyes. Annually, a total of more than 7×10^5 tons of dyes are produced out of which azo dyes account for 60–70%. Over the years, the use of dyes has increased and is immensely used in industries like textile, cosmetics, pulp and paper, paint, pharmaceutical, food, carpet and printing. The discharge from these industries is highly colored as enormous amount of dyes remains unfixed during coloring and washing. The discharge of effluent without proper treatment can get mixed with surface and ground waters and eventually can enter the drinking water (Sarkheil et al. 2014). In addition, weathering of these dyes through oxidation, hydrolysis, anaerobic decoloration or other chemical reactions occurring in the wastewater phase can generate potential carcinogens which pose adverse effect on animal and human health (Absalan et al. 2011; Celekliet et al. 2012). Moreover, dye effluent if discharged untreated affects the photosynthesis of aquatic plants by blocking sunlight penetration and oxygen dissolution (Purkait et al. 2007). Therefore, removal of dyes from the colored effluent before discharging them to various water bodies has become a necessity for living Earth.

Various treatment methods such as biological, coagulation-flocculation, electrocoagulation, advanced oxidation, filtration, and adsorption have been reported for the treatment of dye containing wastewater (Ong et al. 2011). Adsorption has been found to be a superior technique in terms of effectiveness, cost, simplicity of design, and ease of operation (Khan et al. 2014). But many of the adsorbent materials show poor adsorption performance. In addition, problems of regeneration and difficulty in separation from the wastewater after use are another the two major concerns of using adsorbents. In this context, we have developed two types of flexible ceramic membrane prepared by electrospinning mentioned in

the next section and studied their potentiality for Reactive Red-120 (RR-120) dye removal from aqueous phase.

1.2 Electrospinning

1.2.1 Advantages of Nanofibers Prepared by Electrospinning

The natural fibers such as cotton, wool, animal or human hairs are not as small in fiber diameter as those of nanofibers (NFs). The diameter of such natural fibers may well be in the 10–20 micrometer range and above; human hair, for example, typically has a diameter around 50 micrometer (Wendorff et al. 2012). Fig. 1.1 shows NFs compared to a normal human hair.

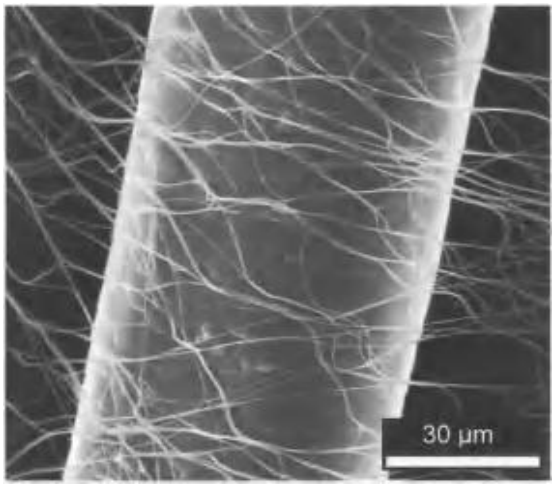

Fig. 1.1 SEM image of human hair–covered by electrospun NFs for comparison (Wendorff et al. 2012).

Fabrication of NF is one of the key advancements in modern nanotechnology. In recent years, various methods such as melt blowing, template synthesis, phase separation, self-assembly and electrospinning have been investigated for manufacturing polymeric NFs. Among these methods, electrospinning spinning is considered as the cheapest and the most straightforward benchtop technique for producing continuous NFs of hydrocarbons, metals, ceramics and composites with controllable diameters ranging from several micrometers down to a few nanometers (Mohammadzadehmoghadam et al. 2016). Moreover the electrospun NFs exhibit excellent properties such as high surface area per unit mass, high porosity (about 90%), light

weight, tunable pore size, flexibility in surface functionalities, high permeability, and high aspect ratio (Wendorff et al. 2012; Baji et al. 2010; Chronakis et al. 2005).

1.2.2 History

Electrospinning is an old technique. This fundamental method was revealed by Rayleigh in 1897, which was followed by Morton and Cooley that patented methods to disperse fluids using electrostatic forces (Mohammadzadehmoghadam et al. 2016). Reports concerning the fabrication of electrospun NFs date back to 1934 when Formhals (1934) filed the first patent on electrospinning. The technique was rediscovered in 1971 by Baumgarten (1971), when he made an apparatus to electrospin acrylic fibers with diameters in the range of 0.05–1.1 μm. Later, Doshi and Reneker (1995) conducted a detailed examination on electrospinning in 1995.

The first technical application of electrospinning was suggested for the nonwoven industry. Prior to the year 2000 electrospinning was the domain of a few specialists; the average number of papers and patents published per year on this topic was below 20. This situation has changed dramatically in recent years. In 2009 significantly more than 1200 papers and patents were published on electrospinning. It is estimated that more than 200 research groups in academia and industry work currently on this topic, the number of conferences or sessions at conferences devoted to electrospinning is continuously increasing. Most likely driven by the growing interest in nanomaterials more and more groups started to enter the field of electrospinning, which resulted in a dramatic increase of publications from a very few per year close to 3100 publications in 2014 (Fig. 1.2). With such a huge impact electrospinning is certainly among the very hot topics in materials science (Wendorff et al. 2012; Shi et al. 2015).

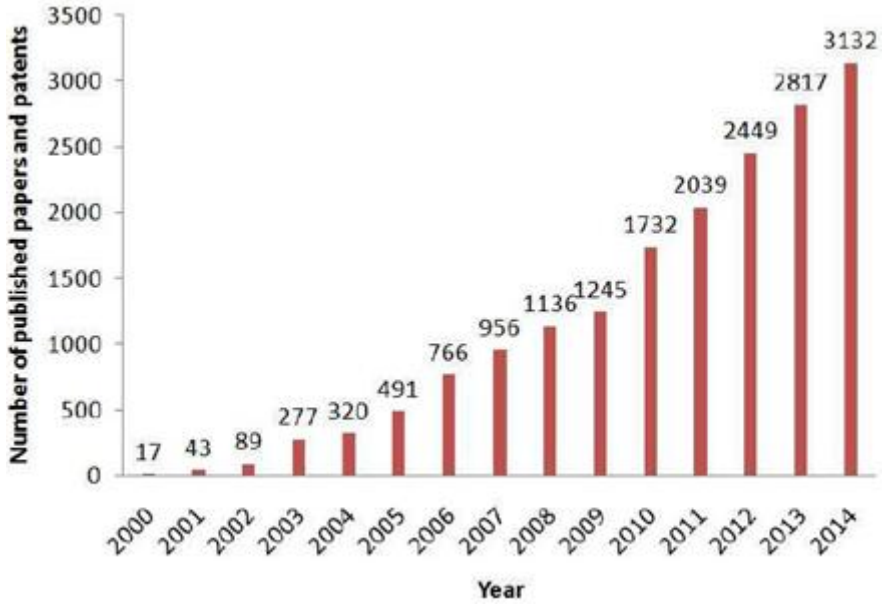

Fig. 1.2 The number of research publications and patents produced between 2000 and 2014 using electrospinning (Li et al. 2016).

1.2.3 Principle

Basically, an electrospinning system consists of three major components as shown in Fig. 1.3: a high voltage power supply (usually in the kV range), a syringe with a metallic needle, and a grounded collector (usually a metal screen, plate, or rotating mandrel). In electrospinning process, a polymer solution held by its surface tension at the end of a capillary tube is subjected to an electric field. Subsequently, a pendant droplet forms. When the repulsive electrostatic force starts to overcome the surface tension of the liquid, the pendant droplet will deform into a conical droplet known as the Taylor cone at the tip of the needle. As the electrostatic force overcomes the surface tension of the conical droplet, a fine, charged jet of polymer solution is ejected from the tip of the needle. The interaction between the electric field and the surface tension of the fluid stretches the jet stream and makes it undergo a whipping motion leading to the evaporation of the solvent. This causes the jet stream to be continuously elongated as a long and thin filament and then this filament solidifies and is eventually deposited onto a grounded collector, resulting in the formation of a uniform fiber (Shi et al. 2015; Bhardwaj and Kundu 2010). Fibers are deposited upon the grounded collector one on top of the other, layer by layer yielding a porous and nonwoven fibrous membrane.

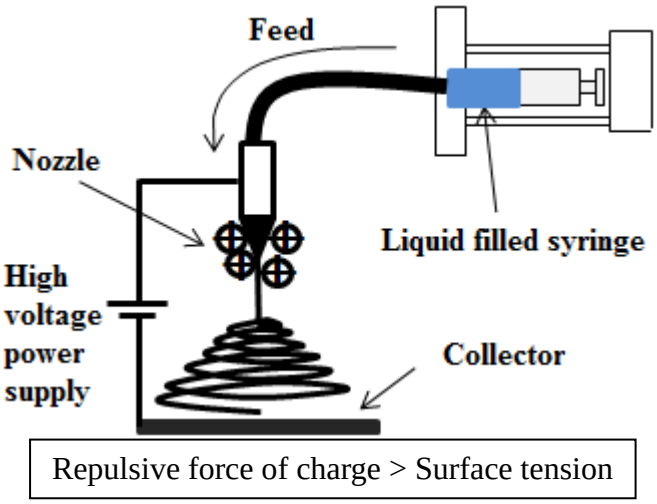

Fig. 1.3 Schematic of an electrospinning set up.

The electrospinning technique can also be used to produce core-sheath fibers using a spinneret with two (inner and outer) coaxial capillaries where a polymer solution (sheath) and a nonpolymer solution (core) or two different polymer solutions (core-sheath) are used as precursor solutions and cospun (Fig. 1.4). This technique was first used by Loscertales et al. (2002), where two dissimilar materials were delivered independently through the coaxial capillary and drawn to fabricate NFs in a core-shell configuration. In this process, the core and sheath precursor solutions are simultaneously fed through inner and outer capillaries, respectively, and the two precursor solutions reach the nozzle through their respective capillaries and form composite droplets. Due to electrostatic repulsions between the surface charges, the sheath liquid of the composite droplets is elongated thereby generating viscous stress. Then this viscous stress is transferred to the core layer and the core liquid is then rapidly stretched. A composite jet is thus formed. Core-sheath NFs are obtained after further stretching and solidifying the composite jet (Shi et al. 2015; Li and Xia 2004).

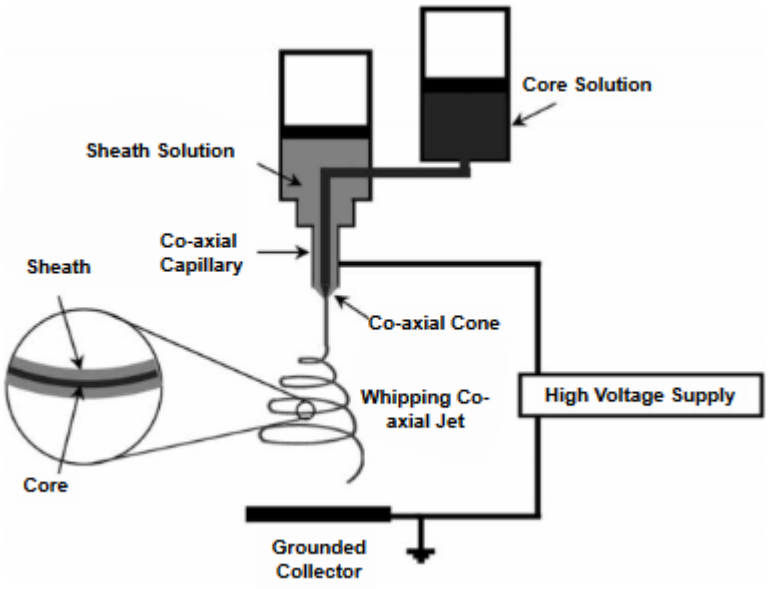

Fig. 1.4 Schematic diagram of coaxial electrospinning set-up for core-sheath fibers (Elahi et al. 2013).

1.2.4 Parameters of Electrospinning

The properties of electrospun NFs depend on a number of parameters. The influential process parameters include solution concentration, viscosity, feed rate, applied voltage, tip-to-collector distance, ambient temperature and humidity. These parameters can be briefly summarized as follows (Mohammadzadehmoghadam et al. 2016; Li et al. 2016; Shi et al. 2015; Li and Wang 2013; Yamashita 2007):

(a) Concentration of polymer solution

When the concentration of the polymer solution is too low, a misty spray will be formed and polymeric particles will be obtained. On the other hand, when the concentration is too high, no spinning will occur. Usually, a concentration of 5–10% solution on the weight basis is recommended. With suitable concentration, smooth NFs can be obtained.

(b) Solution viscosity

Viscosity of polymer solution determines solution spinnability. Over a certain range, reducing the viscosity results better spinnability, and smaller fiber diameter. The viscosity of

the solution should be within a certain range (5–20 Pa·s). If the solution viscosity is lower than a certain value, beaded fibers are produced; on further decreasing viscosity, electrospray occurs instead of electrospinning owing to the low viscosity and high surface tensions of the solution. When the polymer concentration or viscosity is too high, helix-shaped microribbons are formed.

(c) Feed rate

The feed rate of the polymer solution is another important process parameter. The diameter of the electrospun fiber increases with the increase in solution feed rate. But if the feed rate is too high, beaded fibers are formed owing to the short drying time prior to reaching the collector and low stretching forces.

(d) Applied voltage

Within the electrospinning process, applied voltage is the crucial factor. Only the applied voltage higher than the threshold voltage, charged jets ejected from Taylor Cone, can occur. The effect of applied voltage on the fiber diameter varies depending on other parameters such as polymer solution concentration and tip-to-collector distance. Usually, an increase in applied voltage decreases the fiber diameter. However, for some polymer solutions like polyvinyl alcohol (PVA) and polyethylene oxide (PEO), they do not follow this rule.

(e) Tip to collector distance

A minimum distance between needle tip and collector is required for enough time to evaporate solvents before the fiber reach the collector. Longer distance results thinner fibers. But when the distance is too far or close, beaded fibers are formed.

(f) Ambient temperature and humidity

High temperature and low humidity in the spinning area benefit the evaporation of solvent, and this is helpful to get smaller fiber diameters. But, when the temperature is too high, the spinneret may easily be blocked because of fast evaporation. As for the humidity, low humidity may dry the solvent totally and increase the velocity of the solvent evaporation. On

the contrary, high humidity will lead to the thick fiber diameter owing to the charges on the jet can be neutralized and the stretching forces become small.

1.2.5 Application of Electrospun Nanofibers

Electrospun NFs have been successfully applied in various fields, such as, nanocatalysis, biomedicine (e.g. tissue engineering, drug delivery, wound dressing and release control), protective clothing, filtration, adsorption, reinforcement of composite materials, biomedical, pharmaceutical, microelectronics (e.g. batteries, supercapacitors, transistors, sensors, solar cell, and display devices), healthcare, biotechnology, defense and security, space applications, and environmental engineering (Mohammadzadehmoghadam et al. 2016; Shi et al. 2015; Bhardwaj and Kundu 2010). An overview of NFs applied in various subjects and their application domain is shown in Fig. 1.5.

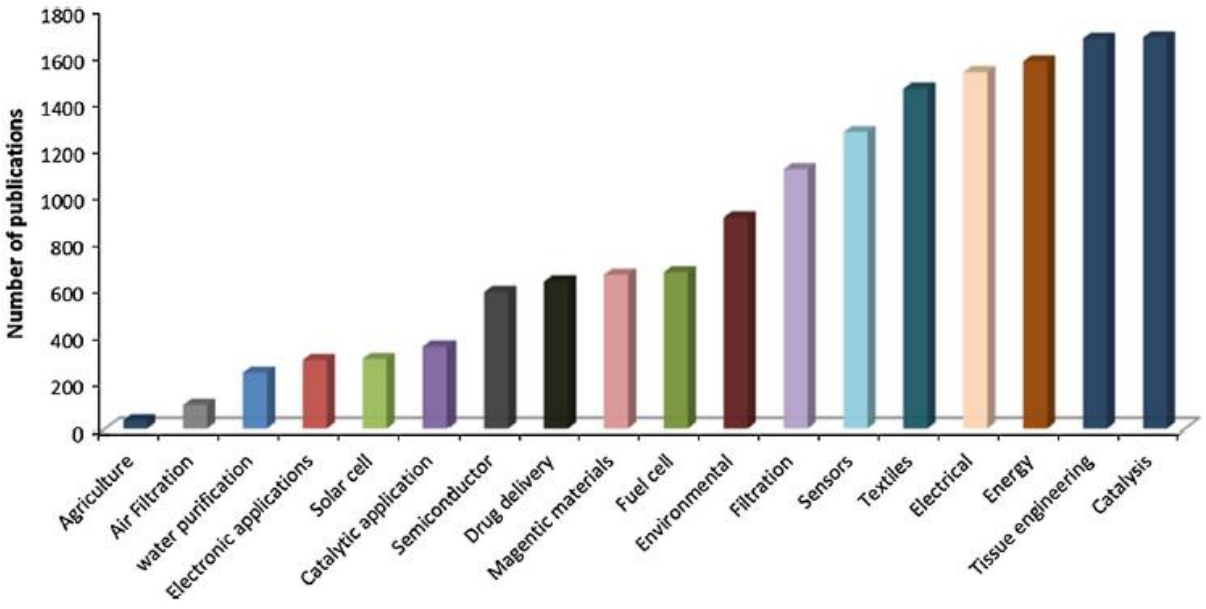

Fig. 1.5 Overview of the number of publications of NFs in various applications (Kaur et al. 2014).

Among various applications of electrospun NFs in Fig. 1.5, I have focused my attention on the following two subjects in my doctoral works.

(a) Application in DSSC

Electrospun NFs have been used in making photoanode and counter electrode of DSSC. TiO_2 anatase NFs prepared by electrospinning are commonly used as photoanode material. Electrospun NFs has lower grain boundaries compared to those of nanoparticles, which leads to better charge conduction and reduced charge-carrier recombination through NFs. Wang et al. (2014) prepared a self-standing nonwoven composite of hybrid nanofibrous TiO_2/SiO_2 mat and TiO_2 nanoparticles, and applied in photoanode of DSSC. They reported that the TiO_2 nanoparticles improve the dye loading, while the TiO_2 NFs enhance the electron transport and the SiO_2 NFs provide the strength and flexibility. Joshi et al. (2010) prepared electrospun carbon NFs and used as counter electrode of DSSC.

(b) Application in adsorption of pollutants from water

The elevated level of metal (such as copper, cadmium, and chromium) ions poses a serious pollution in water resources, and results a long term risk to human health and natural environment as these metal ions easily accumulate in living organisms. Owing to their high specific surface area, high porosity and controllable surface functionality, the electrospun NFs have great potential of adsorbing metal ions from aqueous solution. Two conventional methods for elimination of such pollutants are adsorption and filtration. Interestingly, electrospun NFs mats with a tunable small pore size and high surface area are able to offer both techniques (Thavasi et al. 2008). Polymers with functional groups which have affinity to metal ions are directly electrospun into NFs for metal ion adsorption. For example, electrospun wool keratin/silk fibroin blend NFs were prepared and used to chelate adsorb Cu (II) ions from water by Ki et al (2007). Another approach is to introduce functional materials to fiber surface using surface chemistry or coating techniques to improve adsorption capability (Fang et al. 2011). For example, Wu et al. (2010) prepared PVA/SiO_2 composite nanofibers functionalized by mercapto groups. The specific surface area of the NFs was higher than 290 m^2/g, and the maximum adsorption capacity of the NFs for Cu (II) adsorption was 489.12 mg/g.

Besides heavy metal ions, organic materials in drinking water can cause health hazards and also need to be removed. Kaur et al. (2006) prepared poly(methylmethacrylate) (PMMA) NF membrane functionalized with phenylcarbomylated and azidophenylcarbomylated B-cyclodextrins, and used to removal of phenolphthalein as a model organic molecule from water. The results obtained showed that the functionalized nanofibrous membranes could effectively adsorb the phenolphthalein molecules.

1.3 Dye-Sensitized Solar Cell (DSSC)

1.3.1 Basic Structure of DSSC

The typical structure of a DSSC is shown in Fig. 1.6. The actual dye-sensitized solar cell contains broadly five components: (1) a mechanical support coated with transparent conductive oxides (TCO); (2) the porous semiconductor film, usually TiO_2; (3) a sensitizer adsorbed onto the surface of the porous semiconductor; (4) an electrolyte containing a redox mediator; (5) a counter electrode consisting of a catalyst (usually Pt) layer deposited on TCO-coated substrate (Nazeeruddin et al. 2011).

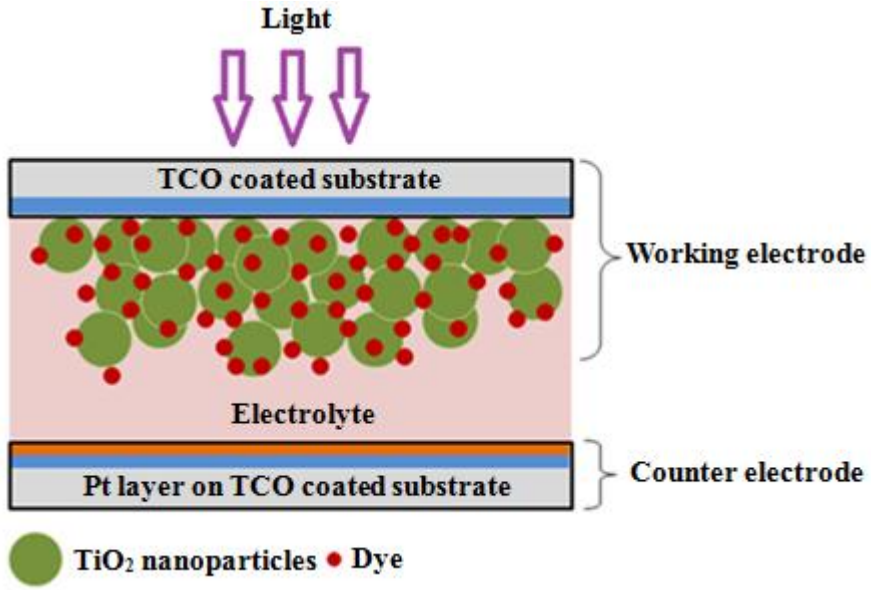

Fig. 1.6 Typical structure of a dye-sensitized solar cell.

(a) Transparent conductive substrate

In DSSC, two sheets of transparent conductive oxide (TCO) coated substrate are used, which act as current collectors and also provide a base for the deposition of the semiconductor or catalyst. Generally, FTO (fluorine tin oxide, SnO_2:F) and ITO (indium tin oxide, In_2O_3:Sn) are used as the conductive substrate. FTO and ITO substrates are composed of soda lime glass coated with fluorine tin oxide and indium tin oxide layers, respectively. FTO films exhibit a sheet resistance of 8.5 Ω/sq, while ITO films have a sheet resistance 18 Ω/sq (Mehmood et al. 2014). Upon sintering at 450 °C for 2 h, the sheet resistance of FTO remains constant, while that of ITO increases from 18 Ω/sq to 52 Ω/sq (Sima et al. 2010).

Alternative to rigid glass substrates, flexible plastic substrates such as PET (Polyethylene terephthalate) coated with ITO or PEN (Polyethylene naphthalate) coated with ITO are also used. However, limitations in the range of usability temperature restrict the application of polymers as substrates in DSSCs (Murakami et al. 2004; Ito et al. 2006; Weerasinghea et al. 2013). Metals such as stainless steel, tungsten, and titanium are used as substrates, but the high cost and corrosion caused by the electrolyte limit their use in DSSCs (Hashmi et al. 2011).

(b) Porous semiconductor film

The porous semiconductor, which provides a surface area for the adsorption of the dye, accepts electrons from the excited dye and conducts them to the external circuit to produce an electric current (Mehmood et al. 2014). Various metal oxides such as TiO_2, SnO_2, ZnO, Nb_2O_5, WO_3, and In_2O_3 have been used as semiconductor materials. However, none of them have shown superior efficiency than TiO_2 in terms of the efficiency of DSSCs (Fukai et al. 2007). The nanocrystalline TiO_2 is considered as an excellent semiconductor material for DSSCs due to its better morphological and photovoltaic properties when compared with other semiconductors (O'Regan and Grätzel. 1991). Of the two crystalline forms of TiO_2, anatase and rutile, the former is more stable and has larger specific surface area for adsorbing dye, and therefore anatase based DSSCs are more efficient (Park et al. 2000).

The recombination of injected electrons with the electrolyte is considered as the main loss path in DSSCs. In order to suppress the charge recombination, a thin insulating layer of metal oxides like SiO_2, Al_2O_3, and ZrO_2 is deposited on the semiconductor electrode which reduces the interaction between injected electrons to the semiconductor and the electrolyte

solution (Palomares et al. 2003). Another approach is the treatment of TCO-substrate (pre-treatment) and semiconductor film (post-treatment) with an aqueous solution of titanium tetrachloride ($TiCl_4$) (Vesce et al. 2010).

(c) Dye (Photosensitizer)

The sensitizing dye in a DSSC is anchored to the porous surface of the semiconductor. When the dye absorbs light, the photoexcited electron rapidly transfers to the conduction band (CB) of the semiconductor. An efficient photosensitizer should show intense absorption in the visible region (400 nm to 700 nm), have a high extinction coefficient, possess more negative LUMO (lowest unoccupied molecular orbital) than the CB of the semiconductor and more positive HOMO (highest occupied molecular orbital) than the redox potential of the electrolyte, and be stable in its oxidized form allowing it to be reduced by an electrolyte (Mehmood et al. 2014).

Dyes typically contain a light harvesting portion, acidic ligands (for example, carboxylic or phosphonic acid) to attach to the semiconductor surface, and ligands to increase the solubility in solution and reduce aggregation between dyes. Sensitizing dyes have traditionally been made from ruthenium based complexes such as N3, N719, C106 and CYC B11, which have fairly broad absorption spectra ($\Delta\lambda \approx 350$ nm) but low molar extinction coefficients (10,000–20,000 $M^{-1}cm^{-1}$). Ruthenium-based complexes work well and have been the most widely used dyes over the past two decades. Organic dyes generally have substantially higher molar extinction coefficients (50,000–200,000 $M^{-1}cm^{-1}$) than ruthenium-based complexes, but typically have narrower spectral bandwidths ($\Delta\lambda \approx$ 100–250 nm) (Hardin et al. 2012).

(d) Electrolyte

The electrolyte regenerates the dye after it injects electrons into the conduction band of the semiconductor and also acts as a charge transport medium to transfer positive charges toward the counter electrodes. Therefore, the electrolyte should have a high electrical conductivity and low viscosity for faster diffusion of electrons, good interfacial contact with the nanocrystalline semiconductor and the counter electrode, not causing desorption of the dye from the oxidized surface and the degradation of the dye, not absorbing light in the visible region (Mehmood et al. 2014).

Based on physical state, electrolytes can be classified into three types: liquid electrolytes, solid state electrolytes, and quasisolid state electrolytes. The liquid organic electrolytes consist of redox couple, solvent, and additives. Various redox couples such as Br^-/Br_3, $SCN^-/(SCN)_2$, $SeCN^-/(SeCN)_2$, and substituted bipyridyl cobalt (III/II) have been studied. But I_3^-/I^- is considered an ideal redox couple due to its good solubility, rapid dye regeneration, low absorbance of light in the visible region, suitable redox potential, and very slow recombination kinetics between injected electrons into the semiconductor and triiodide (I_3). Various types of solvents such as acrylonitrile (AcN), ethylenecarbonate (EC), propylene carbonate (PC), 3-methoxypropionitrile (MePN), and N-methylpyrrolidone (NMP), have been studied. To prevent charge recombination additives like 4-*tert*-butylpyridine (TBP), N-methylbenzimidazole (NMBI), and guanidinium thiocyanate (GuNCS) are used (Mehmood et al. 2014). Although this type of liquid electrolyte produces high efficient DSSCs, their volatile nature causes some difficulties in sealing and thus results poor performance in the long term stability.

In order to mitigate these problems, room temperature ionic liquids (RTIL) have been used as electrolyte. They consist of organic salts containing cations such as pyridinium, imidazolium, and anions from the halide or pseudohalide family (Zakeeruddin and M. Grätzel, 2009). Solid state or quasisolid state electrolytes have been developed to improve the long term stability of DSSCs. Replacement of the liquid type electrolyte with a solid material such as CuI, CuBr, and CuSC, or Spiro-OMeTAD has also been studied by several research groups (Fukui et al. 2006; Tennakone et al. 1999; Meng et al. 2003; O'Regan et al. 1998). A quasisolid state electrolyte is a composite of a polymer and a liquid electrolyte. Poly(vinylidene fluoride-cohexafluoropropylene) (PVDF-HFP) based polymer gel electrolytes and 3-methoxypropionitrile based quasi solid state gel electrolytes showed long term stability (Kang et al. 2003; Nguyen et al. 2009).

(e) Counter electrode

The function of counter electrode is to regenerate the electrolyte. The oxidized electrolyte moves towards the counter electrode where it accepts electrons arriving from the external circuit. In counter electrode, a catalyst is deposited on TCO substrate and platinum (Pt) is considered as an excellent catalyst because of its high exchange current density, good catalytic activity, and transparency. Alternative to Pt, graphene and conductive polymers are

also used as catalyst, but their electrical efficiencies are low when compared to Pt catalyst (Mehmood et al. 2014; Andrade et al. 2011).

1.3.2 Working Principle of DSSC

The operating principle of the dye-sensitized solar cell is shown in Fig. 1.7, and the charge separation process consists of the following steps (Nazeeruddin et al. 2011):
The first step is the absorption of a photon by the sensitizer S (Eq. (1.1)), leading to the excited sensitizer S^* which injects an electron into the conduction band of the semiconductor, leaving the sensitizer in the oxidized state S^+ (Eq. (1.2)).

$$S_{(adsorbed)} + h\nu \rightarrow S^*_{(adsorbed)} \tag{1.1}$$

$$S^*_{(adsorbed)} \rightarrow S^+_{(adsorbed)} + e^-_{(injected)} \tag{1.2}$$

The injected electron flows through the semiconductor network to arrive at the back contact and then through the external load to the counter electrode to reduce the redox mediator (Eq. (1.3)) which in turn regenerates the sensitizer (Eq. (1.4)). This completes the circuit.

$$I_3^- + 2 \cdot e^-_{(cathode)} \rightarrow 3I^-_{(cathode)} \tag{1.3}$$

$$S^+_{(adsorbed)} + \frac{3}{2} I^- \rightarrow S_{(adsorbed)} + \frac{1}{2} I_3^- \tag{1.4}$$

Some undesirable reactions resulting in losses in the cell efficiency occur. They are the recombination of the injected electrons either with oxidized sensitizer (Eq. (1.5)) or with the oxidized redox couple at the TiO_2 surface (Eq. (1.6)).

$$S^+_{(adsorbed)} + e^-_{(TiO_2)} \rightarrow S_{(adsorbed)} \tag{1.5}$$

$$I_3^- + 2 \cdot e^-_{(TiO_2)} \rightarrow 3I^-_{(anode)} \tag{1.6}$$

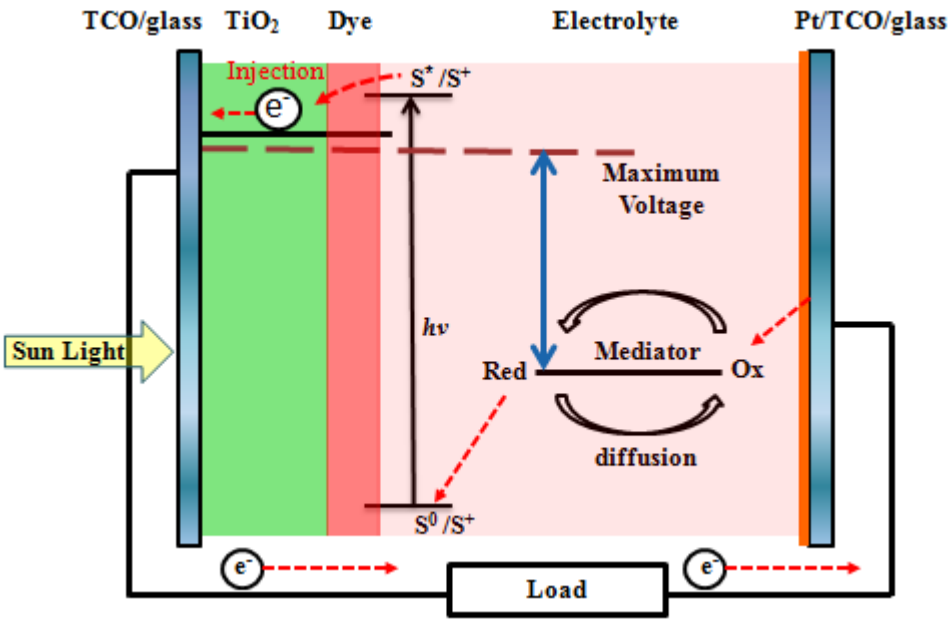

Fig. 1.7 Operating principles of dye-sensitized solar cell. S^0, S^+, S^* are the sensitizer in the ground, oxidized and excited state, respectively, and Red/Ox is the Redox mediator.

1.4 Basic Principle of Adsorption Technique

Adsorption is the process whereby molecules from the gas (or liquid) phase are taken up by a solid surface; it is distinguished from absorption which refers to molecules entering into the lattice (bulk) of the solid material. The adsorptive is the material in the gas or liquid phase capable of being adsorbed, whereas the adsorbate is the material actually adsorbed by the solid. The solid which exposes the surface sites responsible for the process, is called the adsorbent (Bolis 2013). Adsorption process can be classified into 'physical adsorption', where the attraction to the adsorbent surface is due to weak van der Waals forces; 'electrostatic adsorption' where ions in solution are attracted by a surface of the opposite electrical charge; and 'chemical adsorption' where there is a chemical bonding between adsorbent and adsorbate.

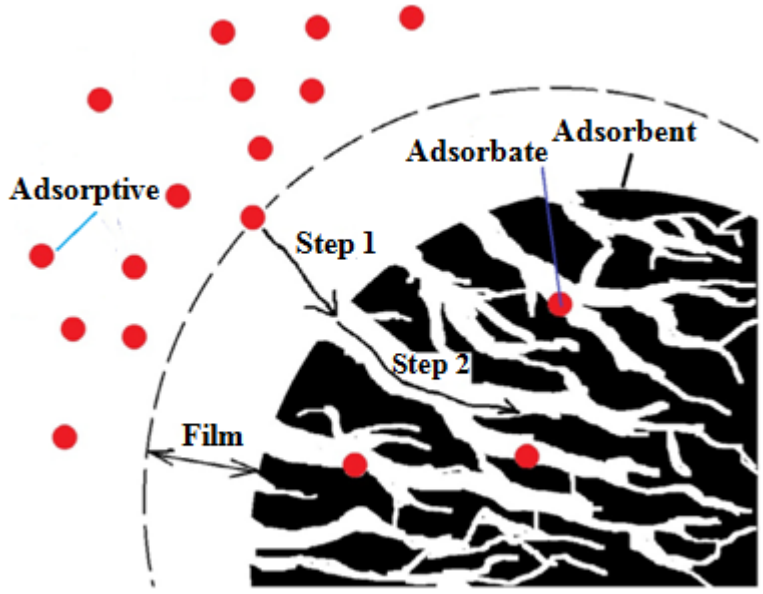

Fig. 1.8 Adsorption of an adsorptive molecule onto the internal surface of a porous adsorbent pellet. Step 1 is film diffusion, and Step 2 is pore diffusion (Tan et al. 2017).

The trajectory of an adsorptive molecule during adsorption is shown in Fig. 1.8. The sorption process can be described by the following steps (Tan et al. 2017; Ho et al. 2000):

Step 1: Film diffusion (external diffusion), which is the transport of adsorptive molecule from the bulk phase to the external surface of adsorbent.

Step 2: Pore diffusion [intraparticle diffusion (IPD)], which is the transport of adsorptive from the external surface into the pores.

Step 3: Surface reaction, which is the attachment of adsorptive to the internal surface of adsorbent. This step is typically very rapid compared with the first and second steps, and therefore poses negligible resistance.

1.5 Research Objectives

The major objectives of the studies presented in this thesis are summarized as follows:

- To develop suitable methods for the preparation of thermally stable, flexible and conductive NF mats of ITO-silica; to characterize the prepared ITO-silica NF mats; and to apply the ITO-silica NF mats as self-standing, light-weight substrates to the working electrode (WE) of DSSCs and reveal the problems in the application.

- To prepare flexible and self-standing fibrous membrane of electrospun alumina-silica NFs; to characterize the prepared alumina-silica NF membrane; and to apply the alumina-silica NF membrane for adsorptive removal of RR-120 dye from water.

- To prepare flexible and self-standing membranes of electrospun alumina-silica/iron oxide core-sheath NFs; to characterize the alumina-silica/iron oxide core-sheath NF membranes; and to investigate the adsorption performance of the prepared core-sheath NF membranes for the removal of RR-120 dye from aqueous solution.

References

Absalan, G., Asadi, M., Kamran, S., Sheikhian, L., & Goltz, D. M. (2011). Removal of reactive red-120 and 4-(2-pyridylazo) resorcinol from aqueous samples by Fe_3O_4 magnetic nanoparticles using ionic liquid as modifier. *Journal of Hazardous Materials*, 192, 476–484.

Andrade, L., Ribeiro, H. A., & Mendes, A. (2011). Dye-sensitized solar cells: an overview. *Encyclopedia of Inorganic and Bioinorganic Chemistry*, 1–20.

Baji, A., Mai, Y-W., Wong, S-C., Abtahi, M., & Chen P. (2010). Electrospinning of polymer nanofibers: effects on oriented morphology, structures and tensile properties. *Composites Science and Technology,* 70, 703–718.

Baumgarten, P. K. (1971). Electrostatic spinning of acrylic microfibers. *Journal of Colloid and Interface Science,* 36, 71–9.

Bhardwaj, N., & Kundu, S. C. (2010). Electrospinning: a fascinating fiber fabrication technique. *Biotechnology Advances,* 28, 325–347.

Bolis V. (2013). Fundamentals in adsorption at the solid-gas interface. concepts and thermodynamics. In: Auroux A. (eds) Calorimetry and Thermal Methods in Catalysis. *Springer Series in Materials Science,* vol 154. Springer, Berlin, Heidelberg.

Celekli, A., İlgün, G., & Bozkurt, H. (2012). Sorption equilibrium, kinetic, thermodynamic, and desorption studies of reactive red 120 on Chara contraria. *Chemical Engineering Journal,* 191, 228–235.

Chronakis I.S. (2005). Novel nanocomposites and nanoceramics based on polymer nanofibers using electrospinning process—A review. *Journal of Materials Processing Technology,* 167, 283–293.

Doshi, J. & Reneker, D.H.J. (1995). Electrospinning process and applications of electrospun fibers. *Journal of Electrostatics,* 35, 151–160.

Fang, J., Wang X., & Lin T. (2011). Functional applications of electrospun nanofibers, nanofibers-production, properties and functional applications. Dr. Tong Lin (Ed.), ISBN: 978-953-307-420-7, InTech.

Elahi, MD., F., Lu, W., Guoping, G., & Khan, F. (2013). Core-shell fibers for biomedical applications—A review. *Journal of Bioengineering & Biomedical Science,* 3, 1–14.

Formhals, A. (1934). Process and apparatus for preparing artificial threads. U.S. Patent No. 1, 975, 504.

Fukui, A., Komiya, R., Yamanaka, R., Islam, A., & Han, L. (2006). The influence of acid treatment of TiO_2 porous film electrode on photoelectric performance of dye-sensitized solar cell. *Solar Energy Materials & Solar Cells,* 90 (5), 649–658.

Fukai, Y., Kondo, Y., Mori, S., & Suzuki, E. (2007). Highly efficient dye-sensitized SnO_2 solar cells having sufficient electron diffusion length. *Electrochemistry Communications,* 9 (7), 1439–1443.

Hardin, B. E., Snaith, H. J., & McGehee, M. D. (2012). The renaissance of dye sensitized solar cells. *Nature Photonics,* 6, 162–169.

Hashmi, G., Miettunen, K., Peltola, T., Halme, J., Asghar, I., Aitola, K., Toivola, M., & Lund, P. (2011). Review of materials and manufacturing options for large area flexible dye solar cells. *Renewable and Sustainable Energy Review,* 15, 3717–3732.

Ho, Y. S., Ng J. C.Y., & McKay, G. (2000). Kinetics of pollutant sorption by biosorbents: review. *Separation & Purification Reviews,* 29 (2), 189–232.

Ito, S., Ha, N.-L. C., Rothenberger G,. Liska, P., Comte, P., Zakeeruddin, S. M., Péchy, P., Nazeeruddin, M. K., & Grätzel, M. (2006). High-efficiency (7.2%) flexible dye-sensitized solar cells with Ti-metal substrate for nanocrystalline-TiO_2 photoanode. *Chemical Communications,* 38, 4004–4006.

Joshi, P., Zhang, L., Chen, Q., Galipeau, D., Fong, H., & Qiao, Q. (2010). Electrospun carbon nanofibers as low-cost counter electrode for dye-sensitized solar cells. *ACS Applied Materials & Interfaces,* 2 (12), 3572–3577.

Kalogirou, S. A. (2005). Seawater desalination using renewable energy sources. *Progress in Energy and Combustion Science,* 31, 242–281.

Kang, M. G., Park, N. G., Kim, K. M., Ryu, K. S., Chang, S. H., & Kim, K. J. (2003). Highly efficient polymer gel electrolytes for dye-sensitized solar cells. Wcpec-3 proceedings, *3rd World Conference on Photovoltaic Energy Conversion,* Tokyo.

Kaur, S., Sundarrajan, S., Rana, D., Sridhar, R., Gopal, R., Matsuura, T., & Ramakrishna, S. (2014). Review: the characterization of electrospun nanofibrous liquid filtration membranes. *Journal of Materials Science,* 49 (18), 6143–6159.

Kaur, S., Kotaki, M., Ma, Z., Gopal, R., Ramakrishna, S., & Ng, S. C. (2006). Oligosaccharide functionalized nanofibrous membrane. *International Journal of Nanoscience,* 05 (01), 1–11.

Khan, M. M. R, Mukhlish, M. Z. B, Mazumder, M. S. I., Ferdous, K., Prasad, D. M. R., & Hassan Z. (2014). Uptake of indosol dark-blue GL dye from aqueous solution by water

hyacinth roots powder: adsorption and desorption study. *International Journal of Environmental Science and Technology,* 11 (4), 1027.

Ki, C. S., Gang, E. H., Um, I. C. & Park, Y. H. (2007). Nanofibrous membrane of wool keratose/silk fibroin blend for heavy metal ion adsorption. *Journal of Membrane Science,* 302 (1-2), 20–26.

Lewis, N. S. (2007). Toward cost-effective solar energy use. *Science,* 315 (5813), 798–801.

Li, H. & Yang, W. (2016). Electrospinning technology in non-woven fabric manufacturing. *Non-woven Fabrics*, Chapter 2, 33–54. http://dx.doi.org/10.5772/62200

Li, Z. & Wang C. (2013). One-Dimensional nanostructures: electrospinning technique and unique nanofibers. *SpringerBriefs in Materials,* 1–139. DOI: 10.1007/978-3-642-36427-3

Li, D. & Xia, Y. (2004). Direct fabrication of composite and ceramic hollow nanofibers by electrospinning. *Nano Letters*, 4 (5), 933–938.

Loscertales, I. G., Barrero, A., Guerrero, I., Cortijo, R., Marquez, M., Ganan-Calvo, A. M. (2002). Micro/nano encapsulation via electrified coaxial liquid jets. *Science,* 295, 1695–1698.

Mehmood, U., Rahman, S., Harrabi, K., Hussein, I. A., & Reddy, B. V. S. (2014). Recent Advances in Dye sensitized solar cells. *Advances in Materials Science and Engineering,* 2014, 1–12.

Meng, Q.-B., Takahashi, K., Zhang X.-T., Sutanto, I., Rao, T. N., Sato, O., Fujishima, A., Watanabe, H., Nakamori, T., & Uragami, M. (2003). Fabrication of an efficient solid state dye-sensitized solar cell. *Langmuir*, 19 (9), 3572–3574.

Miettunen, K., Halme, J., & Lund, P. (2012). Metallic and plastic dye solar cells. *Wires Energy and Environment,* 2, 104–120.

Mohammadzadehmoghadam, S., Dong, S. Y., Barbhuiya, S., Guo, L., Liu, D., Umer, R., Qi,

X. & Tang Y. (2016). Electrospinning: current status and future trends, in nano-size polymers: preparation, properties, applications. S. Fakirov, Editor. *Springer International Publishing*, Chapter 4, 89–154. DOI: https://doi.org/10.1007/978-3-319-39715-3_4

Murakami, T. N., Kijitori, Y., Kawashima, N., & Miyasaka, T. (2004). Low temperature preparation of mesoporous TiO_2 films for efficient dye-sensitized photoelectrode by chemical vapor deposition combined with UV light irradiation. *Journal of Photochemistry and Photobiology A: Chemistry*, 164, (1–3), 187–191.

Nazeeruddin, M. K., Baranoff, E., & Grätzel, M. (2011). Dye-sensitized solar cells: A brief overview. *Solar Energy*, 85, 1172–1178.

Nguyen, P. T., Degn, R., Nguyen, H. T., & Lund, T. (2009). Thiocyanate ligand substitution kinetics of the solar cell dye Z-907 by 3-methoxypropionitrile and 4-tertbutylpyridine at elevated temperatures. *Solar Energy Materials and Solar Cells*, 93, 1939–1945.

Ong, S., Keng, P., Lee, W., Ha, S., & Hung, Y. (2011). Dyes waste treatments. *Water*, 3, 157–156.

O'Regan, B. (1998). Large enhancement in photocurrent efficiency caused by UV illumination of the dye-sensitized heterojunction TiO_2/RuLL'NCS/CuSCN: initiation and potential mechanisms. *Chemistry of Materials*, 10 (6), 1501–1509.

O'Regan, B., & Grätzel, M., (1991). A low-cost, high-efficiency solar cell based on dye-sensitized colloidal TiO_2 films. *Nature*, 353 (6346), 737–740.

Palomares, E., Clifford, J. N., Haque, S. A., Lutz, T., & Durrant, J. R. (2003). Control of charge recombination dynamics in dye sensitized solar cells by the use of conformally deposited metal oxide blocking layers. *Journal of the American Chemical Society*, 125 (2), 475–482.

Park, N.-G., van de Lagemaat, J., & Frank, A. J. (2000). Comparison of dye-sensitized rutile- and anatase-based TiO_2 solar cells. *Journal of Physical Chemistry B*, 104 (38), 8989–8994.

Purkait, M. K., Maiti, A., DasGupta S., & S. De (2007). Removal of congo red using activated carbon and its regeneration. *Journal of Hazardous materials*, 145 (1–2), 287–295.

Sarkheil, H., Noormohammadi, F., Rezaei, A. R., & Borujeni, M. K. (2014). Dye pollution removal from mining and industrial wastewaters using chitson nanoparticles. International Conference on Agriculture, *Environment and Biological Sciences (ICFAE'14)*, Antalya (Turkey), 37–43.

Shi, X., Zhou, W., Ma, D., Ma, Q., Bridges, D., Ma Y., & Hu, A. (2015). Electrospinning of nanofibers and their applications for energy devices. *Journal of Nanomaterials*, 2015, 140716. doi:10.1155/2015/140716

Sima, C., Grigoriu, C., & Antohe, S. (2010). Comparison of the dye-sensitized solar cells performances based on transparent conductive ITO and FTO. *Thin Solid Films*, 519 (2), 595–597.

Tan, K. L., & Hameed B. H. (2017). Insight into the adsorption kinetics models for the removal of contaminants from aqueous solutions. *Journal of the Taiwan Institute of Chemical Engineers*, http://dx.doi.org/10.1016/j.jtice.2017.01.024

Thavasi, V., Singh, G., & Ramakrishna, S. (2008). Electrospun nanofibers in energy and environmental applications. *Energy Environmental Science*, 1, 205–221.

Tennakone, K., Perera, V. P. S., Kottegoda, I. R. M., & Kumara, G. R. R. A. (1999). Dye-sensitized solid state photovoltaic cell based on composite zinc oxide/tin (IV) oxide films. *Journal of Physics D: Applied Physics*, 32 (4), 374–379.

Uddin, T., Nicolas, Y., Olivier, C., & Toupance, T. (2013). Low temperature preparation routes of nanoporous semi-conducting films for flexible dye-sensitized solar cells. Nanotechnology for Sustainable Energy Chapter 6, *ACS Symposium Series*, 1140, 143–172.

Vesce, L., Riccitelli, R., Soscia, G., Brown, T. M., di Carlo, A., & Reale, A. (2010). Optimization of nanostructured titania photoanodes for dye-sensitized solar cells: study and

experimentation of $TiCl_4$ treatment. *Journal of Non-Crystalline Solids*, 356 (37–40), 1958–1961.

Wang, X., Xi, M., Fong, H., & Zhu, Z.(2014). Flexible, transferable, and thermal-durable dye-sensitized solar cell photoanode consisting of TiO_2 nanoparticles and electrospun TiO_2/SiO_2 Nanofibers. *ACS Applied Materials & Interfaces*, 6 (18), 15925–15932.

Wendorff, J. H., Agarwal, S., & Greiner, A. (2012). Electrospinning: materials, processing, and applications. First Edition. Wiley-VCH Verlag GmbH & Co. KGaA.

Weerasinghea, H. C., Huanga, F., & Chenga, Y.-B. (2013). Fabrication of flexible dye sensitized solar cells on plastic substrates. *Nano Energy*, 2 (2), 174–189.

Wu, S., Li, F., Wang, H., Fu, L., Zhang, B., & Li, G. (2010). Effects of poly(vinyl alcohol) (PVA) content on preparation of novel thiol-functionalized mesoporous PVA/SiO_2 composite nanofiber membranes and their application for adsorption of heavy metal ions from aqueous solution. *Polymer*, 51 (26), 6203–6211.

Yamashita, Y. (2007). Electrospinning, the latest in nanotechnology (Seni-sha Osaka).

Yum, J.-H., Baranoff, E., Wenger, S., Nazeeruddin, M. K., & Gratzel, M. (2011). Panchromatic engineering for dye-sensitized solar cells. *Energy and Environmental Science*, 4 (3), 842–857.

Zakeeruddin, S. M. & Grätzel, M. (2009). Solvent-free ionic liquid electrolytes for mesoscopic dye-sensitized solar cells. *Advanced Functional Materials*, 19 (14), 2187–2202.

CHAPTER 2

SELF-STANDING CONDUCTIVE ITO-SILICA NANOFIBER MATS FOR USE IN FLEXIBLE ELECTRONICS AND THEIR APPLICATION IN DYE-SENSITIZED SOLAR CELLS

2.1 Introduction

In most photovoltaic devices such as perovskite solar cells (Kojima et al. 2009*;* Li et al. 2006) and dye-sensitized solar cells (DSSCs) (O'Regan et al. 1991)**,** a photovoltaic mesoporous layer of titanium dioxide (TiO_2) is developed on a glass substrate covered by a transparent conducting oxide (TCO) layer. The drawbacks of this type of substrates relate mainly to their rigidity, weight, and frangibility, which limit the potential integration of photovoltaic devices in portable electronics and their conformability to any surface, including curved ones (Brown et al. 2014). Moreover, the commonly used TCO-coated glass substrates account for as much as 60% of the total material costs of device (Kalowekamo et al. 2009; Kroon et al. 2006). Alternative, low-cost, light-weight and flexible plastic substrates such as indium tin oxide (ITO) coated polyethylene terephthalate (PET) or ITO coated polyethylene naphthalate (PEN) have been investigated for the fabrication of DSSC electrodes (Mehmood et al. 2014; Miettunen et al. 2012).

A major challenge for making photovoltaic devices on flexible plastic substrates is the temperature limitation in producing the TiO_2 mesoporous layer because most plastic substrates limit the thermal treatment to approximately 150 $^{\circ}$C (Weerasinghe et al. 2013). Such a layer is usually fabricated on a TCO-coated glass substrate using a TiO_2 slurry containing various solvents and organic binders. The electrode is then sintered at 450–550 $^{\circ}$C to remove the binders in the film and to form effective inter-particle chemical bonding between TiO_2 nanoparticles and that with the TCO layer on the substrate via a solid state diffusion mechanism. Such a high temperature process cannot be realized with plastic substrates (Weerasinghe et al. 2013; Uddin et al. 2013). Difficulties such as decreased adhesion of the TiO_2 film with the substrate and poor electrical contact between TiO_2 particles arise when plastic substrates are used in a low temperature process (Carreras et al. 2007). Although metals such as stainless steel, tungsten, and titanium can be used as thermally durable and flexible substrates, the high cost and corrosion caused by the

electrolyte in DSSCs prohibit the use of metals as substrates (Mehmood et al. 2014; Hashmi et al. 2011).

To overcome the problems relating to glass and plastic substrates, low cost, light-weight and flexible inorganic substrates are desirable. In this paper, we proposed a nonwoven mat of inorganic electrospun nanofibers (NFs) as one candidate to replace the glass or plastic substrates. Iskandar et al. (2010) fabricated ITO-NFs on an ITO glass substrate using the electrospinning technique and used a TCO substrate of DSSCs. They revealed that ITO-NFs are effective in improving the performance of DSSCs due to the reduction of grain boundaries in the TiO_2 mesoporous layer, efficient high charge collection, and rapid electron transport, as was also observed with electrospun NFs of niobium doped TiO_2 (Horie et al. 2013). Therefore, alternative to a TCO-coated glass or plastic substrate, we proposed self-standing nonwoven mats of supporting flexible electrospun NFs of silica hybridized with conductive NFs of ITO.

In the present work, self-standing, mechanically flexible nanofiber (NF) mats of ITO-silica suitable for application in photovoltaic devices as a heat-resistive light-weight substrate were prepared. The aims of our study were (a) to develop novel and suitable methods for the preparation of thermally stable, flexible and conductive NF mats; (b) to characterize the prepared NF mats with several physical methods (bending, sheet resistance, SEM and XRD); and (c) to apply the NF mats as self-standing, light-weight substrates to the working electrode (WE) of DSSCs and reveal the problems in the application. We made the conductive and flexible NF mats using two different innovative approaches: (1) a drop-coating of silica ES-NF mats using an ITO solution, and (2) ITO-silica hybridized NF mats using simultaneous electrospinning of ITO-NFs and silica NFs on a rotating drum collector. After a thorough review of the available literature, to the best of our knowledge, this is the first time ITO-silica complex NF mats with outstanding flexibility have been prepared and applied as thermally stable conductive substrates in producing photo electrodes of DSSCs.

2.2 Materials and Methods

2.2.1 Materials

Tetraethylorthosilicate (TEOS, 98%), dimethyl sulfoxide (DMSO, 99.9%) and polyvinyl pyrrolidone (PVP, M_w = 1,300,000) were purchased from Sigma-Aldrich. Ethanol (99.5%), N,N-dimethyl formamide (DMF, 99.5%), hydrochloric acid (HCl), indium (III) chloride

tetrahydrate ($InCl_3$-$4H_2O$), tin (IV) chloride pentahydrate ($SnCl_4$-$5H_2O$) and polyvinyl pyrrolidone (PVP, M_w = 360,000) were obtained from Wako. Solutions of 5 M indium chloride and 5 M tin chloride were prepared separately by adding the required amount of ethanol to $InCl_3$-$4H_2O$ and $SnCl_4$-$5H_2O$, respectively, and stored for further use.

2.2.2 Drop-coating of ITO on Silica NF Mat

The fabrication of a drop-coated ITO-silica NF mat (Mat-1) was accomplished by the preparation of a silica-NF mat using the electrospinning method followed by drop-coating with an ITO solution. Fig. 2.1 shows the preparation procedure of the ITO-silica NF mat using the drop-coating method. Silica precursor solutions were prepared by a method modified from the reference (Xi et al. 2014). For the preparation of silica NFs, 1.6 mL TEOS, 0.6 mL HCl (0.1 M) and 0.5 mL ethanol were mixed together followed by magnetic stirring for 4 h and then added to another solution that was made by dissolving 1.0 g PVP (M_w = 360,000) in a mixed solvent of 6.8 mL DMF and 1.18 mL DMSO. The resulting mixture was then stirred for 5 h to obtain the silica spin dope.

The spin dope was loaded into a plastic syringe equipped with a 23 gauge needle made of stainless steel, and a nanofiber sheet of silica/PVP was prepared using an electrospinning apparatus (MECC NANON-05) on a flat piece of aluminum foil. The electrospinning process was conducted in air under an applied voltage of 22.5 kV and feed rate of 2.3 mL/h for 30 min. The as-spun nanofiber sheet on the aluminum foil was kept in air for 24 h to allow complete hydrolysis of the TEOS precursor. The self-standing and flexible mat of silica-NFs was obtained after calcination in a furnace at 650 $^{\circ}$C for 2 h at a heating rate of 2 $^{\circ}$C/min.

The ITO solution for the drop-coating (ITO solution-1) was made by mixing 3.533 mL $InCl_3$-$4H_2O$ (5 M), 0.623 mL $SnCl_4$-$5H_2O$ (5 M) and 2.173 mL ethanol. The atomic ratio of Sn in the solution was set as 15%. The conductive mat was then made by drop-coating the ITO solution-1 on calcined silica-NF mat using a syringe, followed by calcination in a furnace at 450 $^{\circ}$C for 2 h at a raising rate of 2 $^{\circ}$C/min.

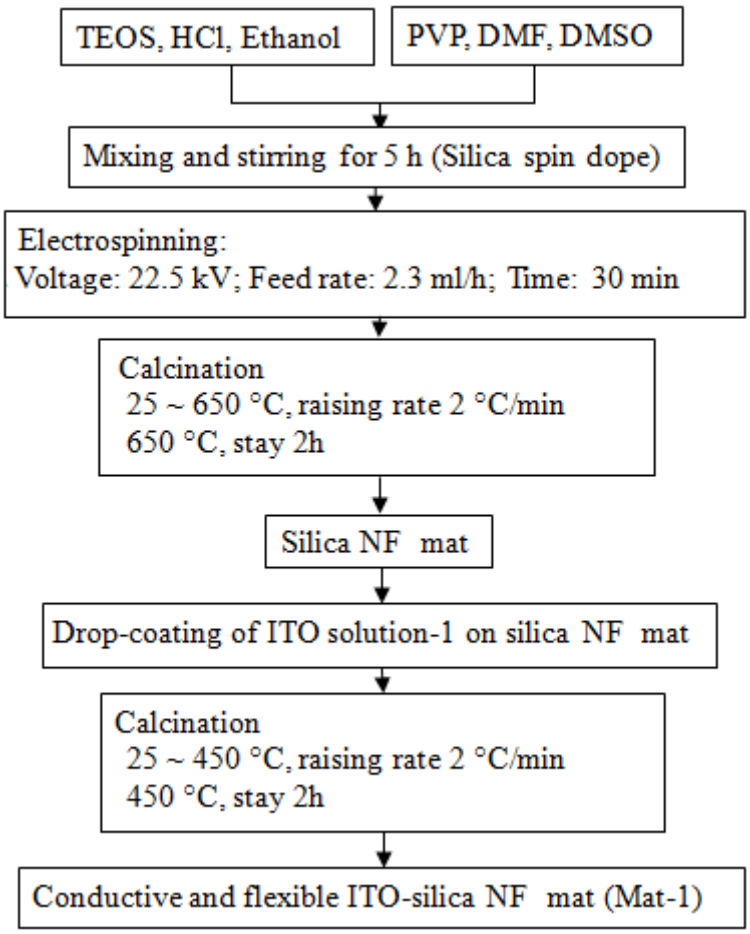

Fig. 2.1 Preparation procedure for a conductive and flexible ITO-silica NF mat (Mat-1) using the drop-coating method.

2.2.3 ITO-Silica Mixed NFs on Drum Collector

The hybrid-NF mat of ITO-silica (Mat-2) was prepared using the dual-spinneret electrospinning technique, and the preparation procedure is shown in Fig. 2.2. To make the ITO spin dope (ITO solution-2), 3.533 mL of 5 M $InCl_3$-$4H_2O$ solution, 0.623 mL of 5 M $SnCl_4$-$5H_2O$ solution and 8.502 mL of ethanol were mixed together first. Another solution was prepared by dissolving 1 g of PVP (M_w = 1,300,000) in a mixture solvent of 4.21 mL DMF and 2.53 mL ethanol followed by stirring for 2 h (solution-3). Afterwards, ITO solution-2, solution-3 and DMF were mixed together at a volume ratio of 4:12:5 followed by stirring for 2 h to obtain the ITO spin dope for electrospinning of ITO-NFs.

The preparation method of the silica spin dope is exactly the same as Mat-1 mentioned in the previous subsection. The two syringes equipped with 27 gauge stainless

steel needles were loaded with an ITO spin dope or silica spin dope and were placed vertically on a grounded drum collector. The two spin dopes were then electrospun simultaneously on aluminum foil on the rotating drum collector (100 rpm) under a feed rate of 0.8 mL/h and 0.4 mL/h for ITO and silica, respectively, applying a voltage of 19 kV. By a successive electrospinning, a "triple-layer structure" of the ITO-silica NF mat was obtained with the following order: (1) only silica NFs were spun for 20 min to obtain a strong supporting layer of silica NFs; (2) silica and ITO were spun simultaneous for 40 min to obtain a thick conductive layer; and (3) only ITO-NFs were spun for 4 min to obtain good electrical contact with the TiO_2 mesoporous layer fabricated on the ITO-silica NF mat. The as-electrospun mat was put under ambient conditions for 24 h to complete the sol-gel reactions of ITO and TEOS; thereafter, this hybrid mat was peeled off from the aluminum foil and calcined at 650 $^{\circ}$C for 2 h with a heating rate of 2 $^{\circ}$C/min.

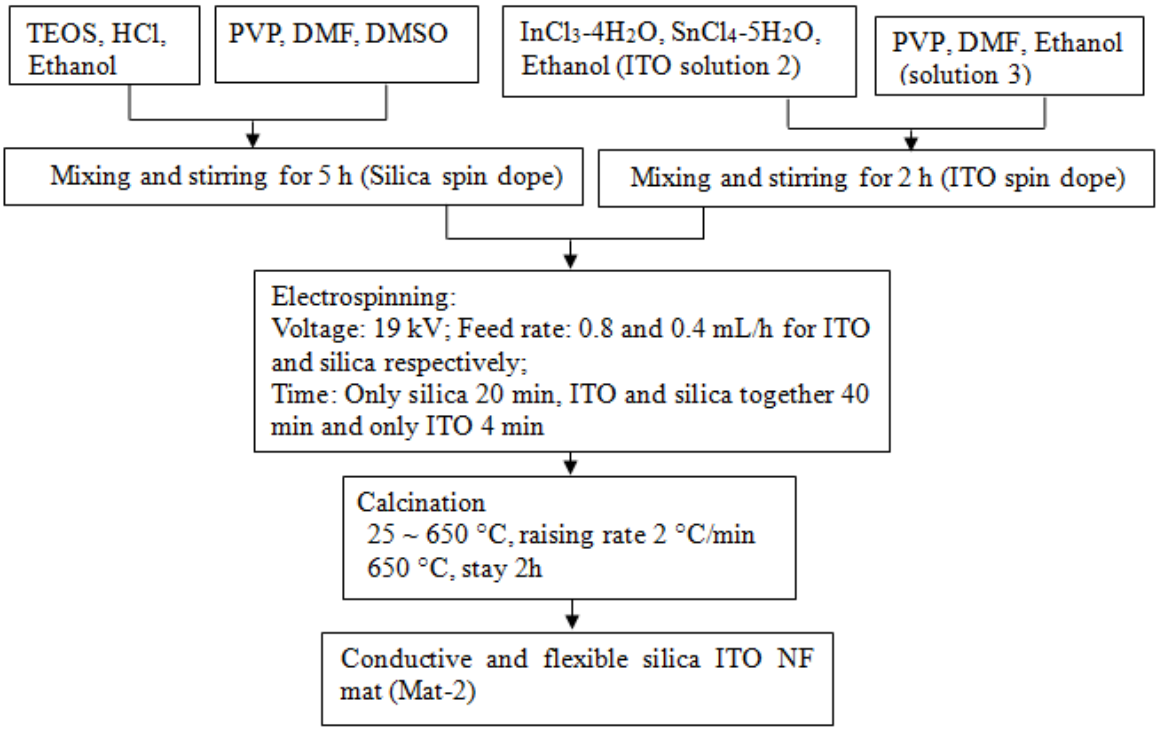

Fig. 2.2 Preparation procedure for a conductive and flexible ITO-silica NF mat (Mat-2) on a drum collector.

2.2.4 Fabrication of DSSC

Two types of ITO-silica NF mats, *i.e.* Mat-1 and Mat-2, were used as conductive/self-standing substrates for the fabrication of working electrodes (WE) in DSSC-1 and DSSC-2, respectively. Fig. 2.3 shows the schematic illustration of the cell structure in which the prepared ITO-silica NF mat accompanied with a TiO_2-dye layer was used as WE. A TiO_2 paste containing TiO_2 nanoparticles of PST-18R (JGC Catalysts and Chemicals, grain size ~20 nm) was soaked in the prepared ITO-silica NF mats. The squeegee method was used to ensure a uniform distribution of TiO_2 nanoparticles and uniform thickness of WE. After resting at room temperature for 10 min, the TiO_2-coated mats were calcined successively under 200 $^{\circ}$C -5 min and 450 $^{\circ}$C -30 min on hot-plate in air. The prepared mats were then sensitized with an N719 dye solution (0.3 mM in ethanol, Dyesol) at 40 $^{\circ}$C for 20 h and used as WE in DSSCs. The FTO/glass covered by a platinum layer with a sputter coater was used for the counter electrode (CE). A thin (~30 µm) polyester fiber net was used as spacer between WE and CE. A plastic (polyethylene) cover was used to encapsulate the electrolyte solution (Dyesol, EL-HSE).

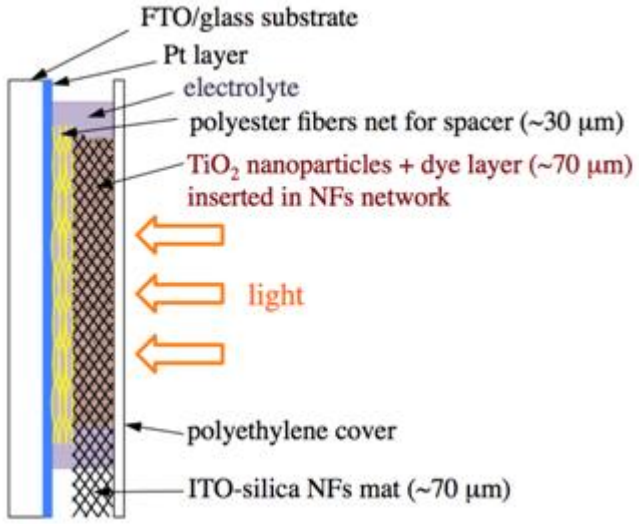

Fig. 2.3 Schematic illustration of a DSSC device made of an ITO-silica NF mat as a conductive and self-standing substrate. The photovoltaic measurements were carried out under simulated AM1.5 illumination at 100 mW/cm^2 irradiated from the right side of the cell.

2.2.5 Characterization of ITO-Silica NF Mats and DSSCs

(a) Current-voltage measurements (*J-V* curve)

The photovoltaic characteristics of DSSCs were obtained by conventional *J-V* measurements irradiating simulated AM 1.5 illumination at 100 mW/cm^2 (Bunkoukeiki, KP-3202) from the right side of the illustration shown in Fig. 2.3.

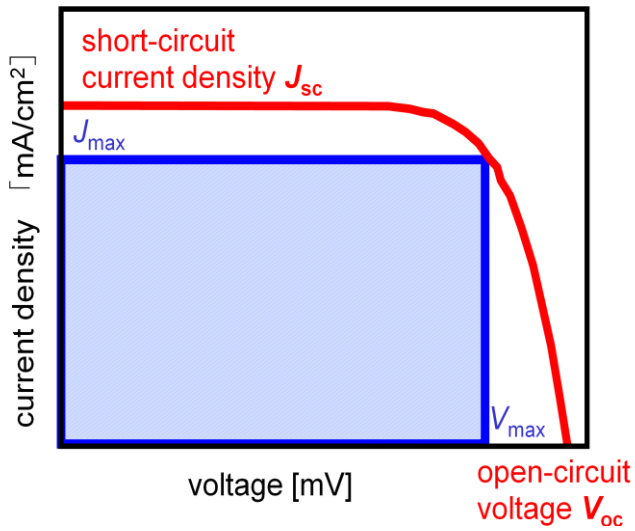

Fig. 2.4 Typical solar cell *J-V* curve and its characteristic parameters.

Fig. 2.4 shows the typical *J-V* characteristic curve. The parameters of a DSSC are defined as follows.

Short-Circuit Current density (J_{sc}):

The maximum current density (mA/cm^2) that can run through the solar cell when the voltage across the cell is zero (i.e., when the solar cell is shot circuited) is termed the short-circuit current density, J_{sc}.

The Open-Circuit Voltage (V_{oc}):

The open-circuit voltage, V_{oc}, is the maximum photovoltage that can be obtained from the solar cell and corresponds to the voltage where current under illumination is zero.

Fill Factor (FF):

The fill factor (FF) is a measure of the maximum power output from a solar cell and is defined as the ratio of the maximum power obtained from the solar cell to the product of V_{oc} and J_{sc}:

$$FF = \frac{J_{max} \times V_{max}}{J_{sc} \times V_{oc}} \quad (2.1)$$

Where J_{max} and V_{max} correspond to current and voltage values, respectively; at which the maximum power output is achieved. FF represents the squareness of the *J-V* curve and is a dependent on the series and shunt resistances of the solar cell. To achieve high fill factor, the series resistance has to be as small as possible, while the shunt resistance needs to be as high as possible.

Efficiency (η):

The overall performance of the DSSC can be estimated in terms of cell efficiency (η) which can be defined as the ratio of maximum electric power output to the radiation power incident on the solar cell surface and expressed as:

$$\eta = \frac{J_{sc} \cdot V_{oc} \cdot FF}{W_{ph}} \quad (2.2)$$

Where J_{sc} is the short-circuit current density (mA/cm^2), V_{oc} the open-circuit voltage (V), FF is the fill factor and Wph the incident light power. The efficiency of the solar cell is estimated under a set of internationally recognized standard condition such as at'AM1.5 Global'solar irradiation and at a temperature of 25 °C.

(b) Electrochemical impedance spectroscopy (EIS)

The electrochemical impedance spectra (EIS) of the fabricated DSSCs were measured by applying a superimposed open-circuit voltage of V_{oc} as bias and ac voltage of 10 mV, in the frequency range of 0.1 Hz-100 kHz using a frequency response analyzer (Solartron, SI 1280) under simulated AM 1.5 illumination.

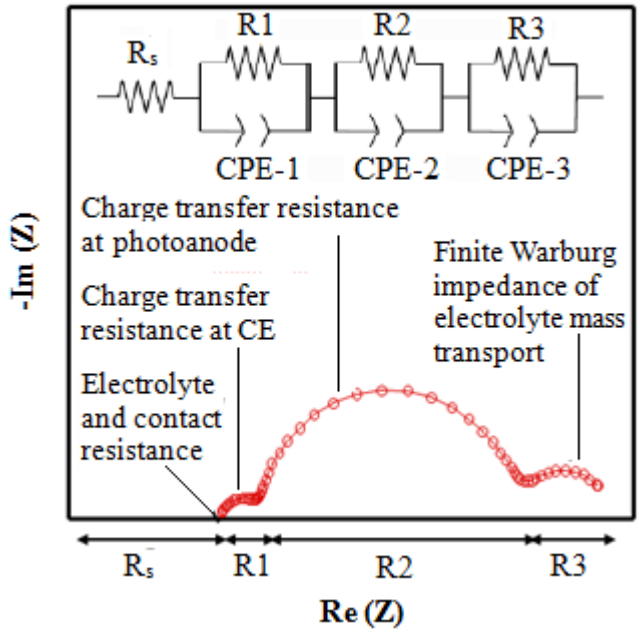

Fig. 2.5 Typical Nyquist plot of DSSC.

Electrochemical impedance spectroscopy (EIS) is used to investigate the charge transfer resistance and interfacial capacitances that are present in a DSSC internal equivalent circuit including contact resistances. The results of impedance spectroscopy are usually presented in the form of a Nyquist plot. The Nyquist plot represents the imaginary impedance, which results from the capacitive and inductive character of the cell as a function of the real impedance. Fig. 2.5 shows a typical Nyquist plot for DSSC which has three characteristic semicircles. From the plot, impedance elements in DSSC are determined for the equivalent circuit shown in the inset of Fig. 2.5, where R1 is generally assigned to the impedance related to the charge transport at the surface of Pt counter electrode, R2 is assigned to the charge transport at TiO_2/dye/electrolyte interface, R3 is related to the diffusion resistance of the redox species in the electrolyte, R_s is the ohmic resistance of DSSC which is mainly attributed to the sheet resistance of TCO, and CPE is the constant phase element (Horie et al. 2013).

2.3. Results and discussion

2.3.1 Properties and Morphology of ITO-Silica NF Mats

Figs. 2.6(a)–(d) show the SEM images of two types of ITO-silica NF mats: an ITO-coated silica-NF mat (Mat-1) and a hybrid NF mat of ITO-silica (Mat-2). In Mat-1, the surface of

silica NFs as well as the inter-NF space was filled with ITO. The average diameter of uncovered silica NFs was ~275 nm. In contrast, the nonwoven sheet of Mat-2 was formed with a mixture of the network of ITO-NFs and silica-NFs; and the diameter was ~74 nm and ~152 nm for ITO-NFs and silica-NFs, respectively. In both cases, NFs were not aligned even though they were prepared on a rotating drum collector. Because the interspace among NFs becomes narrow and the flexibility of the mats was lost by the alignment of NFs, the rotating speed was set as small as 100 rpm to prevent the alignment of NFs.

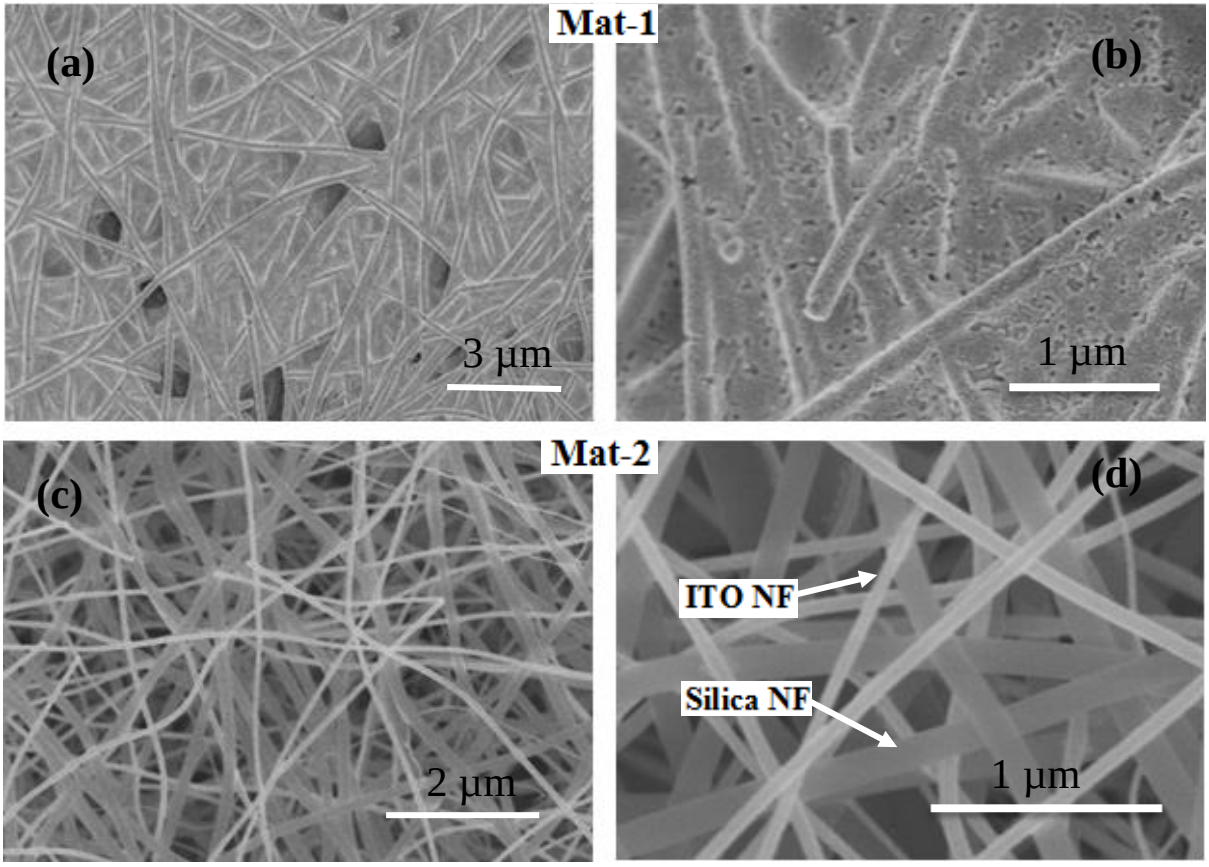

Fig. 2.6 SEM images of self-standing ITO-silica NF mats: (a), (b) ITO coated silica NF mat (Mat-1) and (c), (d) hybrid NF mat of ITO/SiO_2 (Mat-2).

Fig. 2.7 shows the test of flexibility of the self-standing ITO-silica NF mats of Mat-1 and Mat-2. The free-standing ITO-silica NF mats could be bent down to a radius of 9 mm without any fracture, whereas a bending radius of ~10 mm is often sufficient for most envisioned applications (Baca et al. 2008). No crack was found upon bending, indicating excellent bendability and flexibility of the NF mats. Because ITO itself is brittle and sensitive to tensile and compressive stress during bending (Brown et al. 2014), the ITO-NF mat alone

is also very fragile and cannot be freestanding. In the complex form of ITO and silica-NFs, however, the amorphous silica NFs facilitate the stress during bending and retain the integrity of the mat. Thus, the NF mats have sufficient mechanical strength to be used as self-standing substrate in DSSCs.

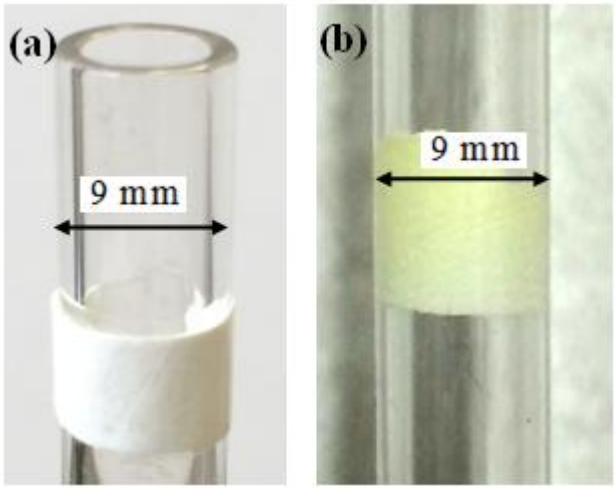

Fig. 2.7 Test of the flexibility of ITO-silica NF mats wound on a tube 9 mm in diameter: (a) Mat-1 and (b) Mat-2.

The sheet resistance of the NF mats in a 1×1 cm^2 area and ~70 μm thick was measured using the van der Pauw method with four-point probes at room temperature. The ITO-coated silica NF mat (Mat-1) exhibited a sheet resistance of 15.3 Ω/sq, which is comparable with that of ITO/polymer substrates (~10–16 Ω/sq) (Brown et al. 2014; Miettunen et al. 2012; Murakami et al. 2004). Mat-2, consisting of both ITO-NFs and silica-NFs had a higher sheet resistance than Mat-1, at 113 Ω/sq. This may be due to the small cross section of each ITO NF in the NF network of Mat-2 as found in the SEM images.

2.3.2 XRD Analysis

The XRD spectra of the ITO-silica NF mats are presented in Fig. 2.8. In the XRD pattern of Mat-1 of Fig. 2.8(a), sharp diffraction peaks due to the rhombohedral structure of indium oxide (In_2O_3) were observed. The values of the interplanar spacing and lattice parameter obtained for this sample matched well with the standard data (Park et al. 2004; JCPDS # 22-336). For Mat-2 in Fig. 2.8(b), the crystal structure of ITO in the mat was determined to be a cubic bixbyite In_2O_3 structure. The interplanar spacing and lattice parameter values obtained

for this sample showed a good agreement with the standard data (Hamberg et al. 1986). No phases corresponding to other tin compounds were detected in any of the two mats, showing that Sn atoms were successfully doped in In_2O_3. The silica-NFs in the mats were amorphous because the calcination temperature 650 °C was far below the temperature (>1000 °C) required for amorphous silica to transform into a crystalline phase (Liu et al. 2008).

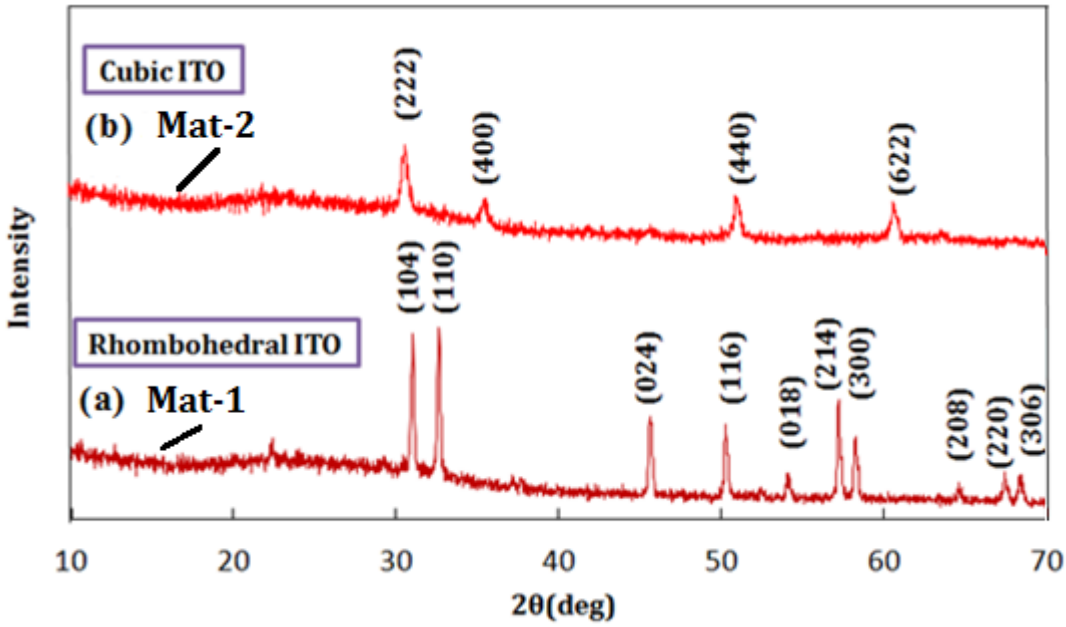

Fig. 2.8 XRD spectra of ITO-silica NF mats: (a) Mat-1 and (b) Mat-2.

The cubic and rhombohedral structures are polymorphs of In_2O_3 (Seo et al. 2006). Cubic In_2O_3 has a C-type rare-earth structure with a lattice parameter of 1.0117 nm and 16 formula units per unit cell. In contrast, rhombohedral In_2O_3 has a corundum structure (a = 0.5487 nm, c = 1.452 nm, $\alpha = \beta = 90^\circ$, $\gamma = 120^\circ$) with six formula units per unit cell. The cubic structure is known to have a lower density and be relatively stable under lower atmospheric pressure than the rhombohedral structure. During the calcination of a hybrid-NF mat of ITO-silica (Mat-2), the crystallization of ITO is accompanied with the decomposition of a polymer in ITO-NFs containing PVP. Because the wide space around the ITO-NFs gives lower atmospheric pressure than the case of drop-coated ITO-silica NF mat (Mat-1), a different crystal structure should appear.

According to the report for the electrical conductivity of nanocrystaline powder (Seo et al. 2006), the conductivity of cubic ITO, 0.65 S/cm, is more than two times higher than that of the rhombohedral structure, 0.26 S/cm. This shows that the difference in the sheet

resistance between Mat-1 and Mat-2 is not related to the difference in the crystal structure. The different ITO structure observed in ITO-silica NF mats might be due to the difference in the process for the formation of the ITO layer in Mat-1 and ITO NFs in Mat-2. Because the density of ITO ingredient in as-electrospun NFs is low including polymer chains, the cubic phase is considered to grow during the formation process of ITO crystals in calcination compared to the rhombohedral phase, with a higher packing factor and larger density (Seo et al. 2006).

2.3.3 Cross Sectional View of TiO_2-loaded NF Mats

Figs. 2.9(a) and (b) show the SEM images of the cross section of TiO_2-loaded NF mats of DSSC-1 and DSSC-2 made from Mat-1 and Mat-2, respectively. Both for the mats, it was found that the thickness of the mat in DSSC-1 and DSSC-2 was ~70 μm, and TiO_2 nanoparticles were penetrated into the mats.

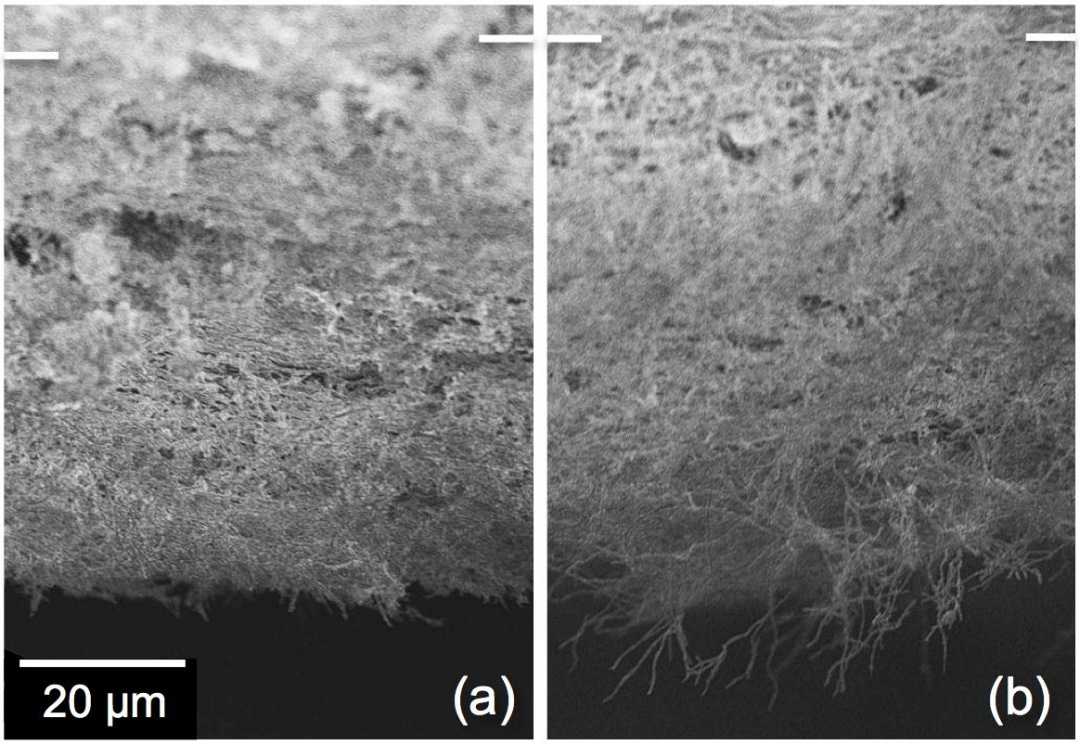

Fig. 2.9 SEM images of the cross section of TiO_2-loaded NF mats of (a) DSSC-1 and (b) DSSC-2 made from Mat-1 and Mat-2. The white bars near the top of the figures show the border with the top face, and the thickness of the mats was ~70 μm.

2.3.4 Photovoltaic Characteristics and EIS Analysis for DSSCs

Figure 2.10 shows the current-voltage (*J*-*V*) characteristic curves obtained for DSSC-1 and DSSC-2 made of Mat-1 and Mat-2, respectively. The values of the photovoltaic parameters, such as short-circuit current density (J_{sc}), open-circuit voltage (V_{oc}), fill factor (FF), and efficiency (η), obtained for the prepared DSSCs are summarized in Table 2.1. For comparison, the parameters obtained for the conventional DSSC with a typical structure ~10 μm thick using an FTO/glass substrate (Horie et al. 2013) are shown in the table. The parameters for conventional DSSC were obtained in our laboratory using the same dye, electrolyte, TiO_2 paste, measurement system, etc. The difference is only the structure and the thickness of the photoelectrode.

DSSC-1 with drop-coated ITO-silica mat (Mat-1) exhibited a J_{sc} of 7.67 mA/cm^2 and yielded an efficiency of 1.51%. Again, DSSC-2, in which Mat-2 was used as a substrate for photoelectrode, showed a J_{sc} of 1.85 mA/cm^2 and efficiency of 0.35%. To examine the stability of prepared DSSC, the same measurements were repeated for about two days. As shown in Fig.2.11, the efficiency showed an increase at the beginning and a good stability after that. The increase of the efficiency is well known behavior for DSSCs (Joly et al. 2014; Gao et al. 2016), and is explained by the activation of the electrode because of the improved penetration of the ionic liquid electrolyte through the complete thickness of the electrode. However, the efficiency was lower than the conventional DSSC prepared on an FTO/glass substrate. From Table 2.1, the large difference in efficiency is mainly attributed to low FF values in both DSSCs using flexible ITO-silica NF mats. Such low FF values are often explained by the existence of a large series resistance and/or small shunt resistance (Wu et al. 2007).

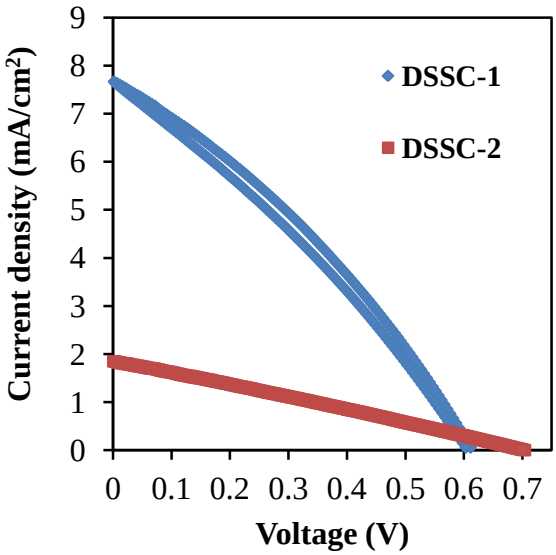

Fig. 2.10 *J-V* characteristic curves obtained for DSSC-1 and DSSC-2 made of Mat-1 and Mat-2, respectively.

Table 2.1 Photovoltaic parameters and impedance elements of the DSSCs prepared in this study together with those in a conventional DSSC with a typical structure using an FTO/glass substrate (Horie et al. 2013). The value of R_p of the conventional one is the sum of three parallel resistance components obtained from the EIS spectrum

Cell	**Photovoltaic parameters**				**Impedance elements**	
	V_{oc} (V)	J_{sc} (mA/cm^2)	FF	η (%)	R_s (Ω)	R_p (Ω)
DSSC-1	0.61	7.67	0.32	1.51	88.43	198
DSSC-2	0.70	1.85	0.27	0.35	377	955
FTO/glass (Horie et al. 2013)	0.71	11.25	0.71	5.62	2.7	7.3

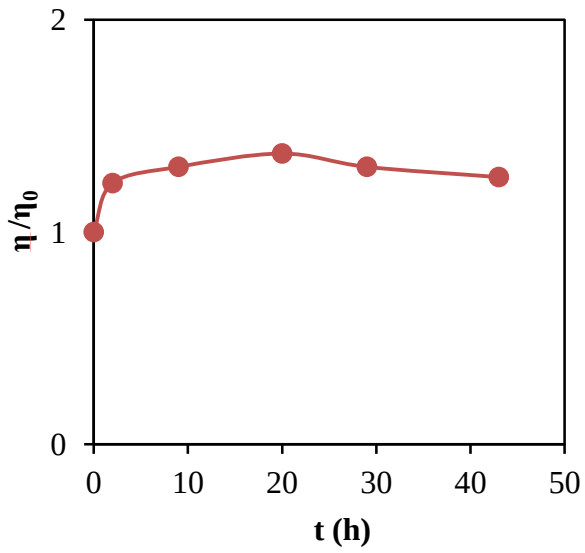

Fig. 2.11 Time variation of the efficiency η of Mat-2. The efficiency η is normalized with the initial value η_0.

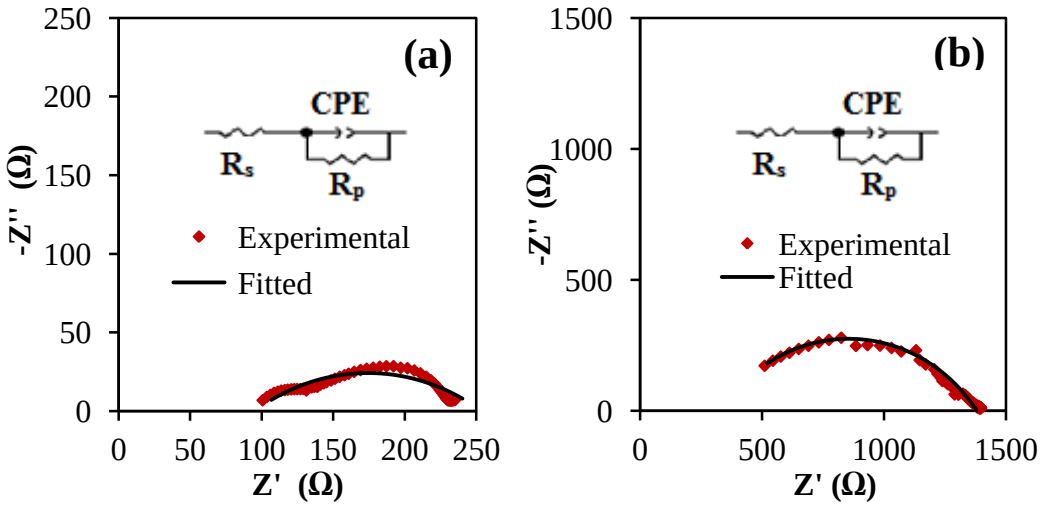

Fig. 2.12 Electrochemical impedance spectra (EIS) for (a) DSSC-1 and (b) DSSC-2. The dots represent the experimental values, whereas the lines represent the fitted values. Insets show the equivalent circuits used for the parameters fitting.

The electrochemical impedance spectra (EIS) obtained for DSSC-1 and DSSC-2 are shown in Figs. 2.12 (a) and (b), respectively. In typical TiO_2-based standard DSSCs, it is known that three semicircles corresponding to the individual impedance components at electrochemical interfaces in DSSCs are observed in the Nyquist plot (Horie et al. 2013; Lee

et al. 2015; Han et al. 2004; Hoshikawa et al. 2005). However, fewer semicircles were found in Figs. 2.12 (a) and (b). This might be attributed to the similar magnitude of time constants at each electrochemical interface, and some of the three circles overlap. Such dissimilarity with standard DSSCs should be related to the complicated electrode structure using conductive NF mat. Because it was difficult to separate the three electrochemical components from the spectra in Figs. 2.12 (a) and (b), impedance elements in DSSCs were determined using the simplest equivalent circuit shown in the inset of Figs. 2.12 (a) and (b), in which one overall semicircle is found in the Nyquist plot. In the equivalent circuit, R_s, CPE and R_p indicate the ohmic series resistance, constant phase element and charge-transfer resistance of DSSC, respectively.

These determined values are summarized in Table 2.1 together with those obtained for a conventional DSSC using an FTO/glass substrate (Horie et al. 2013). The value of R_p of the conventional DSSC is presented by the sum of three parallel resistance components obtained from the EIS spectrum. Because for both DSSC-1 and DSSC-2 the values of R_s and R_p were much larger than those of conventional DSSCs, the low FF values are mainly attributed to the large resistances in the cells. In addition, the lower value of V_{oc} of DSSC-1 and the low J_{sc} might imply the existence of a direct leak current from the surface of ITO to electrolyte. Another factor for reducing J_{sc} is the small amount of TiO_2 nanoparticles penetrated into the interspace of NFs network. In our method for making a photosensitive mesoporous layer of TiO_2 after making the NF mat, NFs themselves disturb the penetration of TiO_2 nanoparticles. Although it is difficult to estimate the amount of penetrated TiO_2 nanoparticles, the amount of dye adsorbed on the surface of TiO_2 nanoparticles should be reduced even though the thickness is approximately seven times larger than the conventional one. In addition, because the incident light is strongly scattered inside the complex structure of the thick photoelectrode, the effective amount of dye for light absorption should be reduced. The small R_p value was given by the suppression of the photocarriers excitation due to the reduction in light absorption.

From Table 2.1, it is also apparent that the performance of DSSC-1 was more than four times larger than that of DSSC-2, and this could also be related to the smaller resistances of R_s and R_p in DSSC-1 than DSSC-2. The difference in the resistance components is caused by the difference in sheet resistance between Mat-1 and Mat-2. Because the large sheet resistance is due to the small cross section of each ITO-NF in the NFs network, one method to improve the performance of the DSSC is to enlarge the cross section of ITO by increasing the diameter of ITO-NFs, or increasing the thickness of the ITO layer on silica-NFs.

2.4. Conclusions

For the first time, we succeeded in preparing self-standing ITO-silica NF mats with excellent flexibility and thermal durability (>400 °C) using the electrospinning method. The drop-coated ITO-silica NF mat (Mat-1) exhibited a sheet resistance of 15.3 Ω/sq, which is comparable to the sheet resistance of ITO/polymer substrates. The hybrid-NF mat of ITO-silica NFs (Mat-2) had a higher sheet resistance of 113 Ω/sq than Mat-1. These NF mats passed the flexibility test of bending down to a radius 9 mm.

The prepared ITO-silica NF mats were successfully applied as thermally stable light-weight substrates to produce working electrodes of DSSCs. However, the efficiency of these DSSCs was lower than that of conventional DSSC prepared on an FTO/glass substrate. The large difference in the efficiency was mainly attributed to low FF values for DSSCs using flexible ITO-silica NF mats. From the measurements of EIS, the low FF values were found to have originated from the large sheet resistance of the ITO-silica mats, which is related to the small cross section of the ITO layer or ITO-NFs. Therefore, to improve the performance of DSSCs, it is necessary to reduce the sheet resistance of ITO-silica mats and to prevent a leak current by forming a thin blocking layer of TiO_2 or Al_2O_3 to cover the surface of the ITO-silica mats. Nevertheless, this inorganic NF mat is expected to be an excellent candidate to replace thick, heavy and rigid glass substrates, particularly in the field of flexible electronics.

References

Baca, A. J., Ahn, J. H., Sun, Y., Meitl, M. A., Menard, E., Kim, H. S., Choi, W. M., Kim, D. H., Huang, Y., & Rogers, J. A. (2008). Semiconductor wires and ribbons for high-performance flexible electronics. *Angewandte Chemie International Edition,* 47, 5524–5542.

Brown, T. M., De Rossi, F., Di Giacomo, F., Mincuzzi, G., Zardetto, V., Reale, A., & Di Carlo, A. (2014). Progress in flexible dye solar cell materials, processes and devices. *Journal of Materials Chemistry A,* 2, 10788–10817.

Carreras, E. S., Chabert, F., Dunstan, D. E., & Franks, G. V. (2007). Avoiding "mud" cracks during drying of thin films from aqueous colloidal suspensions. *Journal of Colloid and Interface Science,* 313, 160–168.

Gao, Y., Li, X., Hu, Y., Fan, Y., Yuan, J., Robertson, N., Hua, J., & Marder, S. R. (2016). Effect of an auxiliary acceptor on D–A–π–A sensitizers for highly efficient and stable dye-sensitized solar cells. *Journal of Materials Chemistry A,* 4, 12865–12877.

Han, L., Koide, N., Chiba, Y., & Mitate, T. (2004). Modeling of an equivalent circuit for dye-sensitized solar cells. *Applied Physics Letters,* 84, 2433–2435.

Hoshikawa, T., Yamada, M., Kikuchi, R., & Eguchi, K. (2005). Impedance analysis of internal resistance affecting the photoelectrochemical performance of dye-sensitized solar cells. *Journal of the Electrochemical Society,* 152, E68–E73.

Hashmi, G., Miettunen, K., Peltola, T., Halme, J., Asghar, I., Aitola, K., Toivola, M., & Lund, P. (2011). Review of materials and manufacturing options for large area flexible dye solar cells. *Renewable and Sustainable Energy Reviews,* 15, 3717–3732.

Hamberg, I., & Granqvist, C. G., (1986). Evaporated Sn-doped In_2O_3 films: Basic optical properties and applications to energy-efficient windows. *Journal of Applied Physics,* 60, R123–R159.

Horie, Y., Watanabe, T., Deguchi, M., Asakura, D., & Nomiyama, T. (2013). Enhancement of carrier mobility by electrospun nanofibers of Nb-doped TiO_2 in dye sensitized solar cells. *Electrochim. Acta,* 105, 394–402.

Iskandar, F., Suryamas, A. B., Kawabe, M., Munir, M. M., Okuyama, K., & Nishitani, T. (2010). Indium tin oxide nanofiber film electrode for high performance dye sensitized solar cells. *Japanese Journal of Applied Physics,* 49, 010213.

JCPDS, Powder Diffraction File, Joint Committee on Powder Diffraction Standards card # 22-336 for rhombohedral In_2O_3.

Joly, D., Pellejà, L., Narbey, S., Oswald, F., Chiron, J., Clifford, J. N., Palomares, & E., Demadrille, R. (2014). A robust organic dye for dye sensitized solar cells based on

iodine/iodide electrolytes combining high efficiency and outstanding stability. *Scientific Reports*, 4, 4033.

Kalowekamo, J., & Baker, E. (2009). Estimating the manufacturing cost of purely organic solar cells. *Solar Energy,* 83, 1224–1231.

Kojima, *A.*, Teshima, K., Shirai, Y., & Miyasaka, T. (2009). Organometal halide perovskites as visible-light sensitizers for photovoltaic cells. *Journal of the American Chemical Society,* 131, 6050–6051.

Kroon, J. M., Bakker, N. J., Smit, H. J. P., Liska, P., Thampi, K. R., Wang, P., Zakeeruddin, S. M., Gratzel, M., Hinsch, A., & Hore S. et al. (2006). Nanocrystalline dye-sensitized solar cells having maximum performance. *Progress in Photovoltaics: Research and Applications,* 15, 1–18.

Lee, J. S., Kim, K. H., Kim, C. S., & Choi, H. W. (2015). Achieving enhanced dye-sensitized solar cell performance by $TiCl_4/Al_2O_3$ doped TiO_2 nanotube array photoelectrodes. *Journal of Nanomaterials,* 2015, Article ID 545818, 1–6.

Li, X., Bi, D., Yi, C., Décoppet, J. D., Luo, J., Zakeeruddin, S.M., Hagfeldt, A., & Grätzel, M. (2016). A vacuum flash–assisted solution process for high-efficiency large-area perovskite solar cells. *Science,* 10.1126/science.aaf8060.

Liu, Y., Sagi, S., Chandrasekar, R., Zhang, L., Hedin, N. E., & Fong, H. (2008). Preparation and characterization of SiO_2 nanofibers. *Journal of Nanoscience and Nanotechnology,* 8, 1528–1536.

Mehmood, U., Rahman, S., Harrabi, K., Hussein, I. A., & Reddy, B. V. S. (2014). Recent advances in dye sensitized solar cells. *Advances in Materials Science and Engineering,* 2014, 1–12.

Miettunen, K., Halme, J., & Lund, P. (2012). Metallic and plastic dye solar cells. *Wires Energy and Environment*, 2, 104–120.

Murakami, T. N., Kijitori, Y., Kawashima, N., & Miyasaka, T. (2004). Low temperature preparation of mesoporous TiO_2 films for efficient dye-sensitized photoelectrode by chemical vapor deposition combined with UV light irradiation. *Journal of Photochemistry and Photobiology A: Chemistry*, 164, 187–191.

O'Regan, B., & Grätzel, M. (1991). A low-cost, high-efficiency solar cell based on dye-sensitized colloidal TiO_2 films. *Nature*, 353, 737–740.

Park, Y., Seo, K., Lee, J., Kim, J., Cho, S., O'Conner, C. J., & Lee, J. (2004). Phase transformation behavior of nanocrystalline ITO powders during heat-treatment: oxygen partial pressure effect. *Journal of Electroceramics*, 13, 851–855.

Seo, K.-H., Lee, J.-H., Kim, J.-J., Bertoni, M. I., Ingram, B. J., & Mason, T. O. (2006). Synthesis and electrical characterization of the polymorphic indium tin oxide nanocrystalline powders. *Journal of the American Chemical Society*, 89, 3431–3436.

Uddin, T., Nicolas, Y., Olivier, C., & Toupance, T. (2013). Low temperature preparation routes of nanoporous semi-conducting films for flexible dye-sensitized solar cells. Nanotechnology for Sustainable Energy Chapter 6 (ACS Symposium Series Vol.1140, 2013) 143–172.

Weerasinghe, H., Huang, F., & Cheng, Y. (2013). Fabrication of flexible dye sensitized solar cells on plastic substrates. *Nano Energy*, 2, 174–189.

Wu, J., Chen, G., Yang, H., Ku, C., & Lai, J. (2007). Effects of dye adsorption on the electron transport properties in ZnO-nanowire dye-sensitized solar cells. *Applied Physics Letters*, 90, 213109.

Xi, M., Wang, X., Zhao, Y., Zhu, Z., & Fong, H. (2014). Electrospun ZnO/SiO_2 hybrid nanofibrous mat for flexible ultraviolet sensor. *Applied physics letters*, 104, 133102.

CHAPTER 3

FLEXIBLE ALUMINA-SILICA NANOFIBROUS MEMBRANE AND ITS HIGH ADAPTABILITY IN REACTIVE RED-120 DYE REMOVAL FROM WATER

3.1 Introduction

Synthetic dyes are extensively used in various industries such as textiles, leather, printing, and paper in order to color their products and these factories generate a large volume of dye-contaminated wastewater. More than 700,000 tons of various dye materials are annually produced in the world (Riera-Torres et al. 2010) and about 15% of these dyes is lost during dyeing process and released in effluents (Celekli et al. 2010). Discharge of the dye-contaminated wastewaters into the water bodies can cause detrimental effects on aquatic life because dyes tend to suppress photosynthetic activity in aquatic habitats by preventing penetration of sunlight (Nourmoradi et al. 2015). Moreover, azo dyes, which constitute about 60–70% of the textile dyestuffs, are identified as carcinogenic and mutagenic compounds and pose a serious threat to aquatic organisms as well as human life (Noorimotlagh et al. 2014). Further, reactive dyes, a prominent class of azo dyes, are highly persistent in natural environment (Celekli et al. 2012) and are reported to be the most problematic compared to other forms of dyes, as they tend to pass through conventional treatment systems unaffected (Geethakarthi and Phanikumar 2011; Aksu 2005). Therefore, development of a suitable method for the removal of these recalcitrant pollutants from wastewater prior to discharge into aquatic ecosystems has become a necessity for living earth.

The traditional techniques used for the removal of reactive dyes from wastewater include membrane filtration, chemical coagulation (Zafar et al. 2015), biological treatment (Gowri et al. 2014), electrochemical treatment (Vijayaraghavan et al. 2013) and adsorption (Dos Santos et al. 2016), and each of these methods has inherent limitations (Khan et al. 2016). However, adsorption has been found to be one of the most applied techniques for dye removal due to its low cost, high efficiency and easy operation, and it does not generate harmful substances (Absalan et al. 2011).

Several types of natural and synthetic adsorbents have been studied for the removal of reactive dyes from colored wastewater (Demarchi et al. 2013; Cardoso et al. 2010; Karcher et al. 2001; Aksu 2005; Kittinaovarat et al. 2010). Recently, much attention has been paid to develop nanoadsorbents with the aim of high adsorptive capacity and low cost (Hou et al.

2012; Shi et al. 2017; Absalan et al. 2011; Poursaberi and Hassanisadi 2013; Hu et al. 2010; Khoshhesab and Ahmadi 2016). Nanostructured adsorbents exhibited remarkable advantages owing to their higher surface areas and much more surface active sites than bulk materials (Wu et al. 2012). Unfortunately, two defects have seriously restricted their practical applications. First, nanoadsorbents, especially nanoparticles, are very easy to aggregate, depriving them of their unique and excellent properties. Second, the high surface energy and the small size of nano range make them very difficult to be separated from the liquid phase after use, which restricts their recyclable applications and causes secondary pollution (Wu et al. 2012; Xu et al. 2012). Therefore, alleviating the agglomeration and developing nanostructured adsorbents with easy solid-liquid separation properties become very important. One important approach is to fabricate continuous nanofiber (NF) membranes, because they can be separated from the liquid phase more easily than powders (Xu et al. 2012).

Alumina (Al_2O_3) is an important ceramic material and has been used in many fields including high-temperature filtration, thermal insulation, composite reinforcement, catalyst support and adsorption (Xu et al. 2001; Li et al. 2015). Among various metal oxides, the oxides of aluminum (Al) have large advantages because of their low cost, extensive availability, thermal stability and remarkable adsorption capacity (Mahapatra et al. 2013). In past few years, alumina materials with different morphologies such as powders (Khoshkhan and Saleh 2014), spherical granule (Liu et al. 2008), short fibers (Xu et al. 2014; Deng et al. 2008), and nanorod (Dabbagh and Shahraki 2013) have been prepared, and up to now, there are few reports on the flexible and continuous alumina NFs having small diameter. Continuous alumina fibers with different diameters such as 150 nm (Azad 2006), 550 nm (Dai et al. 2002), 300–400 nm (Zhang et al. 2012) and 1.45 μm (Li et al. 2015) prepared from various precursors have been reported. The flexibility of fibers as well as their adsorption performance can be improved by decreasing the diameter of fibers (Tan and Lim 2004; Chen et al. 2007; Tsai et al. 2008) and suppressing the phase transformation of alumina from amorphous to crystalline state. Alumina undergoes the crystallization to the alpha phase on heating concomitantly with a great decrease in its surface area (Horiuchi et al. 2001). The addition of silica was found to be effective in suppressing the phase transformation maintaining the large surface area of alumina even after heating (Horiuchi et al. 2001).

However, inorganic NFs are usually fragile, and their application is limited in the practical field, because they are easy to be collapsed into powders or tiny pieces. In this study, we adopted the electrospinning method that is a simple and versatile technique for producing continuous inorganic ceramic NFs (Li et al. 2006) and their hierarchically fibrous membrane.

For the inorganic material with a function of adsorption, we adopted amorphous alumina-silica to get self-standing and flexible membrane of ultrafine NFs with sufficient mechanical strength, because flexible membrane of amorphous silica was already obtained by the electrospinning (Mukhlish et al. 2017).

Among dyes used in textile industries, Reactive Red-120 (RR-120) is one of the frequently used reactive azo dyes (Paul et al. 2011; Celekli et al. 2013). Different adsorbents such as ionic liquid-Fe_3O_4 nanoparticles (Absalan et al. 2011), jute fiber carbon (Senthilkumaar et al. 2006), *Spirogyra majuscule* powder (Celekli et al. 2013), pistachio husk (Celekli et al. 2010), cetylpyridinium-bentonite powder (Tabak et al. 2010), waste tea carbon (Auta 2012), chitosan/modified montmorillonite beads (Kittinaovarat et al. 2010), and clay (Errais et al. 2011) have been used to remove RR-120 dye from colored effluents.

In this study, we have applied the fibrous membrane of ultrafine alumina-silica NFs prepared by the electrospinning to the adsorptive removal of RR-120 dye from water. The hierarchical architecture of the membrane will exhibit high surface area and suitable pore-size distribution, and provide sufficient active sites for the adsorption of dye. Furthermore, the freestanding membrane with excellent flexibility has an advantage in the application to the environmental remediation because of the easy separation from the water. To our best knowledge, there is no report on the adsorption of RR-120 dye onto electrospun NFs. The adsorption tests such as effect of pH, adsorbent dosage and contact time on the sorption of RR-120 dye onto alumina-silica NFs were explored in batch experiments. The adsorption isotherm and kinetic studies were also carried out to elucidate the adsorption mechanism. Desorption studies were conducted to reveal the possibility of recovery of adsorbent and adsorbate.

3.2 Materials and Methods

3.2.1 Materials

Polyvinyl pyrrolidone (PVP, M_w = 360,000), formic acid (98.0%), acetic acid (97.7%), hydrochloric acid (HCl), sodium hydroxide (NaOH), and aluminum powder were obtained from Wako. Tetra ethyl ortho silicate (TEOS, 98%) and Reactive Red-120 (RR-120) dye were purchased from Sigma-Aldrich whereas Triton X-100 (TX) was obtained from Alfa Aesar. The chemical structure and some properties of the RR-120 dye are presented in Fig. 3.1 and Table 3.1, respectively. The stock solutions of RR-120 (300 mg/L) were prepared in distilled

water, and working solutions were obtained by appropriate dilution.

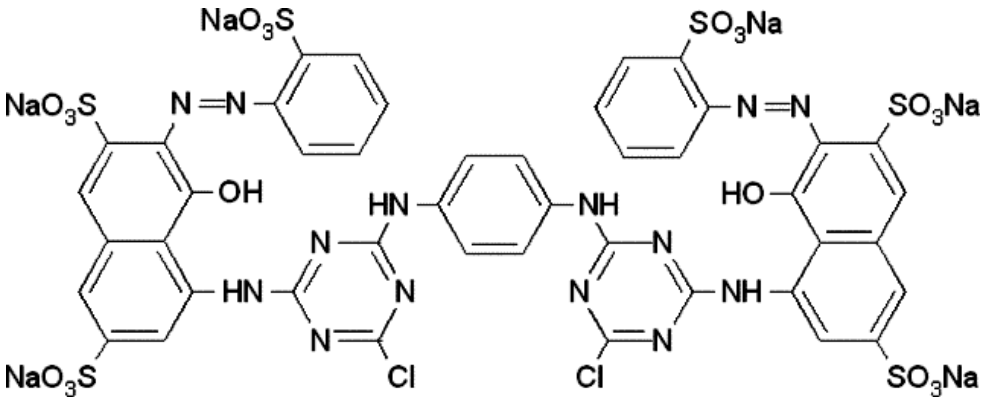

Fig. 3.1 Schematic structure of RR-120 dye (Bazrafshan et al. 2013).

Table 3.1 The general characteristics of RR-120 (Bazrafshan et al. 2013)

Characteristics	Reactive Red-120
Chemical formula	$C_{44}H_{24}C_{l2}N_{14}Na_6O_{20}S_6$
Color index name	Reactive Red-120
Formula weight	1469.98 g/mol
Wavelength of maximum absorbance λ_{max}	515 nm

3.2.2 Preparation of Alumina-Silica NF Membrane

Aluminum precursor solution was prepared by the reaction of aluminum powder with acetic acid and formic acid in aqueous medium. At first, formic acid, acetic acid and water were mixed at a volume ratio of 1:1:3 (solution A). Then, 1g of aluminum powder was added into 30 mL of solution-A followed by heating at 85 $^{\circ}$C under reflux for about 72 h. Then, the solution was filtered to remove a small amount of residual impurities. The resulting filtrate solution (solution B) was used as precursor for the preparation of alumina NFs.

For the preparation of alumina-silica spin dope, 2.5 mL solution B, 0.1 mL TEOS, 0.25 g PVP and 0.4 mL TX were mixed together followed by magnetic stirring for 2 h. The spin dope was filled into a plastic syringe equipped with a 23-gauge needle made of stainless steel, and a nanofibrous membrane was made by an electrospinning apparatus (MECC NANON-05) on a flat piece of aluminum foil. The electrospinning process was conducted in

air under applied voltage 30 kV, humidity < 30% and feed rate 0.5 mL/h for 30 min. The as-spun nanofibrous membrane on the aluminum foil was immediately dried in an oven, because the wet gel NFs can easily join each other forming thick connections which may become centers of crack formation during subsequent calcination (Chakrabarty et al. 2001).

The self-standing and flexible membranes of alumina-silica NFs were obtained after calcination in a furnace at 800 or 900 °C for 2h at a heating rate of 2 °C/min. During calcination, solvents and organic components present in the as-electrospun PVP/alumina precursor's composite NFs were eliminated and inorganic NFs were achieved.

3.2.3 Characterization of NF Membrane

The structure and morphology of the alumina-silica nanofibrous membrane was observed by field-emission scanning electron microscope (FE-SEM, Hitachi SU-70) and X-ray diffractometer (XRD, PANalytical X'Pert PRO MPD). The elemental compositions of the fibers were checked by energy-dispersive X-ray (EDX, Hitachi SU-70) spectroscopy analysis. For the wet gel fibers, thermal behavior of the electrospun NFs was investigated by a thermogravimetric and differential scanning calorimetry (TG-DSC, PerkinElmer STA 6000) analysis to investigate the condition of calcination.

3.2.4 Determination of Surface Charge and pH at the Point of Zero Charge

The surface charge Q and the pH at the point of zero charge pH_{pzc} of alumina-silica NFs in aqueous phase were analyzed with different system pH values by using the titration method (Kiefer et al. 1997). Seven milligrams of alumina-silica NFs was taken into 50 mL 0.1M KNO_3 solution, and agitated with magnetic stirrer. Then, the pH value of the solution was measured after an equilibrium time of 10 min. The titration was conducted with 0.1M NaOH or 0.1M HCl. The surface charge Q of alumina-silica NFs was estimated from the experimental titration data using the equation (Kiefer et al. 1997),

$$Q = \frac{1}{w}(C_A - C_B - [\mathrm{H}^+] - [\mathrm{OH}^-]) \qquad (3.1)$$

where w is the dry weight of adsorbent in aqueous system (g/L), C_A is the concentration of added acid in aqueous system (mol/L), C_B is the concentration of added base in aqueous system (mol/L), and $[H^+]$ and $[OH^-]$ are, respectively, the concentration (mol/L) of H^+ and

OH^- at different equilibrium pH of the system.

3.2.5 Batch Sorption Experiments

The batch sorption experiments were carried out by soaking alumina-silica NFs membrane calcined at 800 °C in 20 mL of RR-120 dye solution. After adsorption, the adsorbent was taken out from the solution, and the residual dye concentration in the supernatant liquid was analyzed using a UV-vis spectrophotometer (Hitachi U-3900) by measuring the absorbance at a wavelength of maximum absorbance (λ_{max} = 515 nm).

The influence of dye solution pH on the adsorptive removal of RR-120 using alumina-silica NFs membrane was investigated over the pH range of 2 to 11. In this study, the pH of initial dye solution (100 mg/L) was adjusted at a desired value by using 0.1 M HCl or NaOH, and the adsorbent mass was maintained at 20 mg for 20 mL dye solution. The effect of the adsorbent mass on the removed amount of RR-120 dye was studied by immersing alumina-silica NFs weighed in the range of 2.8–20 mg into 20 mL dye solution with initial concentration 100 mg/L. All the experiments were carried out at an optimum pH of 3. Equilibrium studies were performed by immersing 2.8 mg alumina-silica NFs into 20 mL dye solution with different initial concentrations of 71–190 mg/L at pH of 3. Each experiment was carried out for 80 h for the attainment of adsorption equilibrium, and the dye concentrations in the samples were estimated from the residual dye concentration in the supernatant liquid as mentioned earlier.

Sorption kinetics experiments were carried out by soaking 2.8 mg alumina-silica NFs in 20 mL dye solution with an initial concentration of 74.26 mg/L at pH of 3. Samples were withdrawn from the dye solution at different time intervals for the measurement of concentrations. The adsorption density defined as the amount of dye (RR-120) adsorbed per unit weight of adsorbent (alumina-silica NFs) was calculated by using the following equations:

$$q_e = \frac{(C_o - C_e)V}{W}, \tag{3.2}$$

$$q_t = \frac{(C_o - C_t)V}{W}, \tag{3.3}$$

where q_e and q_t are the adsorption density (mg/g) at equilibrium and at time t, respectively. C_o, C_t, and C_e represent the dye concentrations (mg/L) at initial, at time t, and at equilibrium,

respectively. V is the volume of solution (L), and W is the mass of adsorbent (g). The percentage removal of dye at time t was calculated using

$$\text{Removal (\%)} = \frac{100(C_o - C_t)}{C_o} \cdot \tag{3.4}$$

3.2.6 Adsorption Isotherms

The adsorption isotherm of a specific adsorbent represents its adsorptive characteristics which is very important for designing the adsorption processes (Absalan et al. 2011). The experimental equilibrium data of dye adsorption on alumina-silica NFs were analyzed using Langmuir (Langmuir 1916) and Freundlich (McKay 1981) isotherm models. The Langmuir model assumes monolayer coverage onto a surface with a finite number of identical sites which are homogeneously distributed over the adsorbent surface. The linearized form of Langmuir isotherm equation is expressed as

$$\frac{1}{q_e} = \frac{1}{q_m} + \frac{1}{q_m K_L} \cdot \frac{1}{C_e} \cdot \tag{3.5}$$

where q_m is the maximum adsorption capacity (mg/g) and K_L is the adsorption equilibrium constant. The values of q_m and K_L are determined from the slope and intercept of the linear plot of $1/q_e$ versus $1/C_e$.

The Freundlich isotherm is used to describe the surface heterogeneity of the sorbent. It considers multilayer adsorption with a heterogeneous energetic distribution of active sites, accompanied by interactions between adsorbed molecules (Mahapatra et al. 2013). A linear form of the Freundlich isotherm can be expressed by

$$\ln q_e = \ln K_F + \frac{1}{n} \ln C_e \cdot \tag{3.6}$$

where K_F and n are the constants representing the quantity of dye adsorbed on adsorbent for unit equilibrium concentration (*i.e.*, C_e = 1) and the adsorption intensity, respectively. The slope $1/n$ of the logarithmic plots is a measure of the sorption intensity or surface heterogeneity. A value of $1/n$ smaller than unity indicates a normal Langmuir isotherm, while $1/n > 1$ is indicative of cooperative adsorption (Fytianos et al. 2000).

3.2.7 Adsorption Kinetics

In order to examine the kinetic mechanism that controls the dye adsorption process, the experimental kinetic data were fitted to pseudo-first order, pseudo-second order, and intraparticle diffusion models.

The Lagergren's rate equation is one of the most widely used rate equations to describe the adsorption of adsorbate from the liquid phase. The first-order equation of Lagergren (Lagergren 1898) is generally expressed as

$$\frac{dq_t}{dt} = k_1(q_e - q_t) \tag{3.7}$$

where k_1 is the rate constant of pseudo-first-order sorption (h^{-1}). The integrated form of Eq. (3.7) becomes

$$\ln(q_e - q_t) = \ln q_e - k_1 t. \tag{3.8}$$

From the linear plot of $\ln(q_e - q_t)$ versus t, k_1 and q_e are calculated from the slope and intercept of the linear plot, respectively.

The pseudo-second-order kinetic rate equation can be expressed as (Ho and McKay 1998)

$$\frac{dq_t}{dt} = k_2(q_e - q_t)^2 \tag{3.9}$$

where k_2 (g/mg h) is the rate constant of the pseudo-second-order model. The integrated form of Eq. (3.9) becomes

$$\frac{t}{q_t} = \frac{1}{k_2 q_e^{\,2}} + \frac{1}{q_e} t. \tag{3.10}$$

If the second order kinetic equation of Eq. (3.10) is applicable, the plot of t/q_t against t should give a linear relationship. The q_e and k_2 can be determined from the slope and intercept of the plot.

The intraparticle diffusion model is expressed by the following Weber and Morris expression (Weber and Morris 1963):

$$q_t = k_i t^{0.5} + C \tag{3.11}$$

where k_i is the rate constant of the intraparticle diffusion (mg/g $h^{0.5}$) and C is a constant related to the thickness of the boundary layer. When only the intraparticle diffusion is the rate-limiting step, C becomes zero. On the contrary, when film diffusion is also taking place, non-zero value of C gives the idea on the thickness of the boundary layer (Nethajia et al. 2010).

3.3 Results and Discussion

3.3.1 TG-DSC Analysis

The TG-DSC curves of as-electrospun gel fiber at a heating rate of 20 °C/min are shown in Fig. 3.2. The TG profile indicates that there is about 73% weight loss up to ~ 800 °C, and further weight loss was small with further increase in temperature. The weight loss below 300 °C corresponds to the removal of absorbed water and surface hydroxyl, while that above 300 °C is ascribed to the decomposition of PVP, TEOS, organometallic aluminum compound (Sato et al. 1984), TX (Athanasiou et al. 2014), and removal of structural water and hydroxyl groups.

In the DSC curve, the endothermic peaks at about 90 and 260 °C are assigned to the removal of absorbed water and surface hydroxyl, respectively. Whereas, the exothermic peaks observed between 300 and 490 °C are due to the combustion of PVP, TX (Athanasiou et al. 2014; Mitsuda et al. 1989) and decomposition of organometallic aluminum compound (Sato et al. 1984). However, the gradual decrease of the weight in a wide temperature range from 450 to ~800 °C implies slow formation and the recombination of the crystal bonds of amorphous alumina-silica.

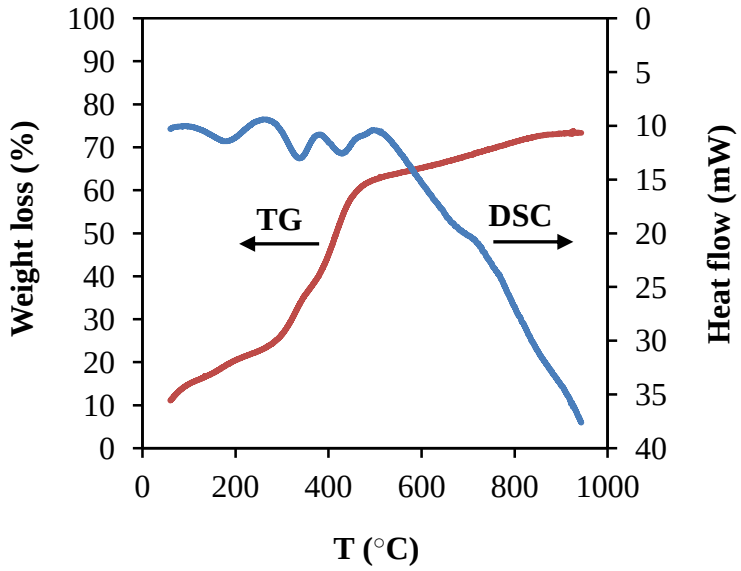

Fig. 3.2 The TG-DSC curves of the as-electrospun alumina-silica NFs at a heating rate of 20 °C/min.

3.3.2 Flexibility Analysis

Fig. 3.3 shows the optical images of the self-standing alumina-silica NF membrane obtained after the calcination at 800 °C. The length, width and thickness of the membrane were about 4.5 cm, 3.5 cm and 75 μm, respectively. No crack was observed in the NFs membrane upon bending (Fig. 3.3(b)) or winding on a tube of 5-mm diameter (Fig. 3.3(c)), indicating excellent flexibility of the calcined NF membrane. The tensile strength of the membrane was measured as 2.2 MPa. Because of its flexibility and thermal stability, the membrane has great potential application in high-temperature filtration, catalyst support and adsorption.

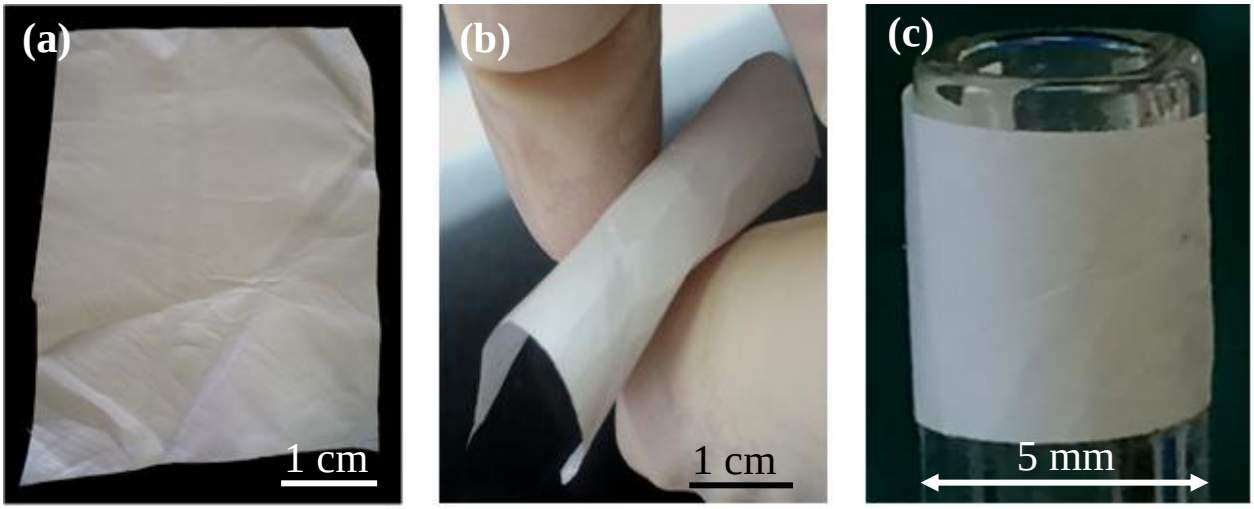

Fig. 3.3 Optical photographs of self-standing alumina-silica NF membrane calcined at 800 °C: (a) as prepared, (b) bent by fingers, and (c) wound on a tube 5 mm in diameter.

3.3.3 SEM and EDX Analysis

Figs. 3.4(a) and (b) show the SEM images of the alumina-silica NF membrane calcined at 800 °C. The NFs with an average diameter of ~ 95 nm were continuous and randomly arranged to form a net-like porous membrane.

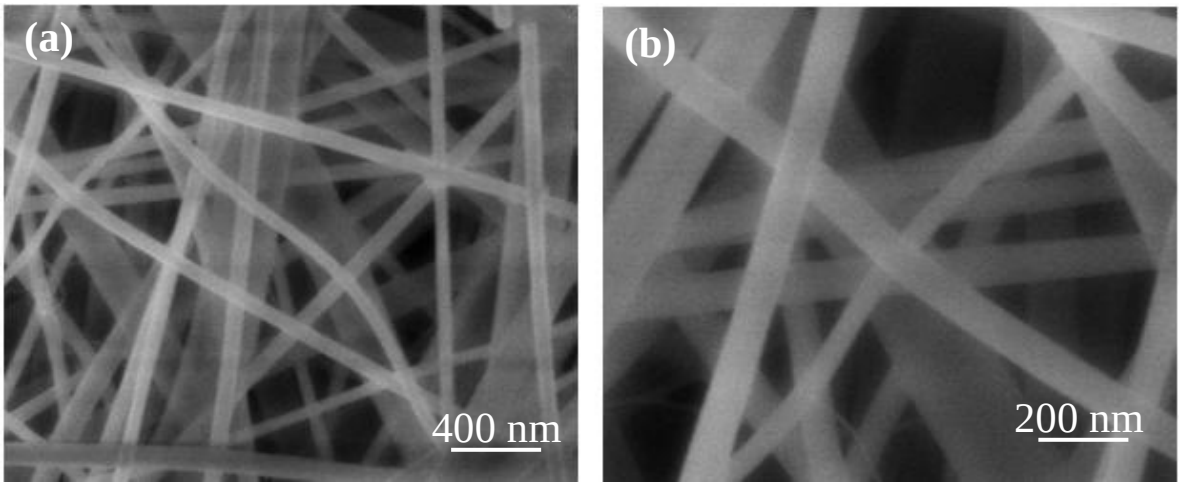

Fig. 3.4 SEM images of alumina-silica NF membrane calcined at 800 °C.

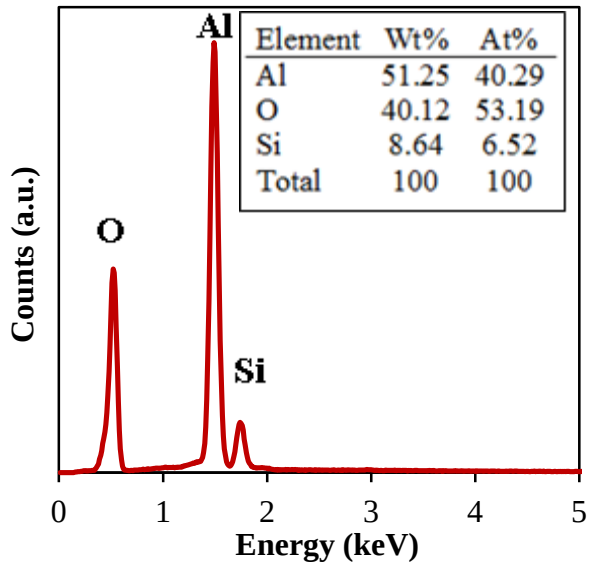

Fig. 3.5 EDX spectrum of alumina-silica NF membrane calcined at 800 °C.

The EDX spectrum shown in Fig. 3.5 indicates that the NFs calcined at 800 °C have an atomic ratio of Al:Si:O = 6.18:1:8.16. This implies that the obtained alumina-silica NFs is not a simple mixture of Al_2O_3 and SiO_2 (or SiO) with a molar ratio of 3.09:1, because the amount of oxygen atoms is much smaller than the estimated ratio of 11.27 (or 10.27 for SiO) for the simple mixture.

3.3.4 XRD and Raman Analysis

Fig. 3.6 shows the X-ray diffraction (XRD) pattern of the as-prepared alumina-silica NF membrane calcined at 800 and 900 °C. No distinct diffraction peak was observed, and the NFs were found to be amorphous. However, at the temperature range of 800–900 °C, the typical peaks of crystalline alumina generally appear (Sato et al. 1984; AN and GUO 2011). In our case, nonappearance of crystalline peaks may be due to addition of TEOS in alumina-silica precursor solution during preparation of spin dope (Timken 2005; Yoshida et al. 2002).

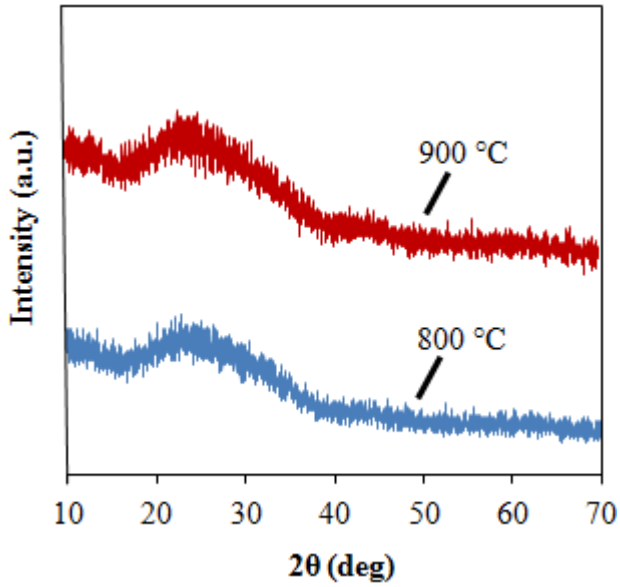

Fig. 3.6 XRD spectra of the alumina-silica NF membrane calcined at 800 °C and 900 °C.

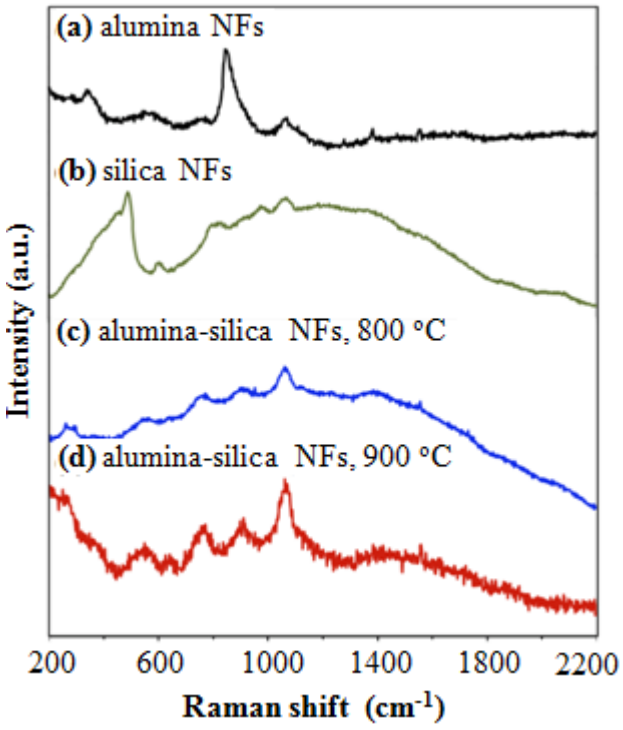

Fig. 3.7 Raman spectra of electrospun alumina, silica and alumina-silica nanofibers.

Fig. 3.7 shows the Raman spectra of electrospun alumina, silica and alumina-silica nanofibers. The alumina NF membrane was prepared using the same starting materials used for the preparation of alumina-silica NF membrane except TEOS, whereas silica NF

membrane was prepared by using the same method described in our previous paper (Mukhlish et al. 2017). The NF membranes of alumina and silica were calcined at 800 and 650 °C, respectively. However, the prepared alumina NF membrane was very fragile and collapsed into tiny pieces. On the contrary, silica NF membrane was flexible having sufficient mechanical strength, which might be related to the amorphous structure.

Table 3.2 Assignments of the Raman spectral bands in Figs. 3.7(a)–(d): [a] Alumina NFs; [b] Silica NFs; [c] Alumina-silica NFs (800 °C); [d] Alumina-silica NFs (900 °C)

Raman shifts (cm^{-1})	Assignments	References
400-530 [b]	Si-O-Si symmetric stretching bending mode	(Faulques et al. 2001; Kingma and Hemley 1994)
600[b]	Si-O stretching mode	(Richet et al. 1998)
810[b]	O-Si-O bending mode	(Malinovsky et al. 2000)
982[b]	Si-O stretching mode	(Peskova et al. 2011)
335[a]	Bending vibrations of AlO_4 and AlO_6 groups	(Thomas et al. 1989)
640[c,d]	Si-O-Al vibration mode	(Tlili et al. 1989)
542[a,c,d]	Al-O-Al bending mode	(Singha and Singh 2016)
770[a,c,d]	Condensed AlO_4 tetrahedra	(Thomas et al. 1989)
840[a]	Al-O vibration mode	(Schram et al. 1998)
914[c,d]	Si-O-Al stretching mode	(Singha and Singh 2016)
1068[a,b,c,d]	Al-O bending or Si-O stretching mode	(Cherepy et al. 2005; Peskova et al. 2011)

Table 3.2 presents the assignments of observed bands in the Raman spectra in Figs. 7(a)–(d). In the spectrum of Fig. 3.7(b) for silica NFs, the strongest bands in 400–530 cm^{-1} were observed, which involve the twisting and bending mode of Si-O-Si in silica tetrahedra or links between tetrahedra (Faulques et al. 2001; Kingma and Hemley 1994). However, the other peaks were relatively small compared with the large hump around 1200 cm^{-1} which shows amorphous characteristics. The small peaks near 600, 982 and 1068 cm^{-1} correspond to Si-O stretching mode (Richet et al. 1998; Peskova et al. 2011), whereas the peak around 810 cm^{-1} corresponds to O-Si-O bending vibrations (Malinovsky et al. 2000). For alumina

NFs in Fig. 3.7(a), the band around 335 cm^{-1} belongs to the bending vibrations of AlO_4 and AlO_6 groups (Thomas et al. 1989), whereas the large peak at 840 cm^{-1} stems from the Al-O vibration of AlO_4 tetrahedrons (Schram et al. 1998). The small peaks near 542 cm^{-1} and 770 cm^{-1} observed both for alumina and alumina-silica NFs (Figs. 3.7(a), (c) and (d)) arise from bending character of Al-O-Al and condensed AlO_4 tetrahedra, respectively (Singha and Singh 2016); Thomas et al. 1989; Cherepy et al. 2005).

The peaks for alumina-silica NFs of Fig. 3.7(c) grew by increasing the calcination temperature as Fig. 3.7(d). However, their spectral pattern was different from alumina NFs and silica NFs. The appearance of new peaks around 640 and 914 cm^{-1} in Figs. 3.7(c) and (d) implies the formation of new bond (Si-O-Al) between alumina and silica (Tlili et al. 1989; Singha and Singh 2016). The peaks appeared for silica NFs were not found for alumina-silica NFs except at around 1068 cm^{-1} which can be assigned to Al-O bending or Si-O stretching mode. Thus, it can be found that a partial crystallization occurred by the formation of new Si-O-Al bonds from the mixture of amorphous silica and alumina in the NFs.

3.3.5 Effect of Solution pH on Adsorption of RR-120 onto Alumina-Silica NFs

Fig. 3.8 shows the surface charge of the alumina-silica NFs as a function of solution pH. From Fig. 3.8, it is apparent that the surface charge of the NFs at pH 6.99 is zero. Hence the pH_{pzc} of alumina-silica nanofibrous adsorbent is 6.99. At pH < pH_{pzc}, the adsorbent surface is charged positively while at pH > pH_{pzc}, the surface is negatively charged.

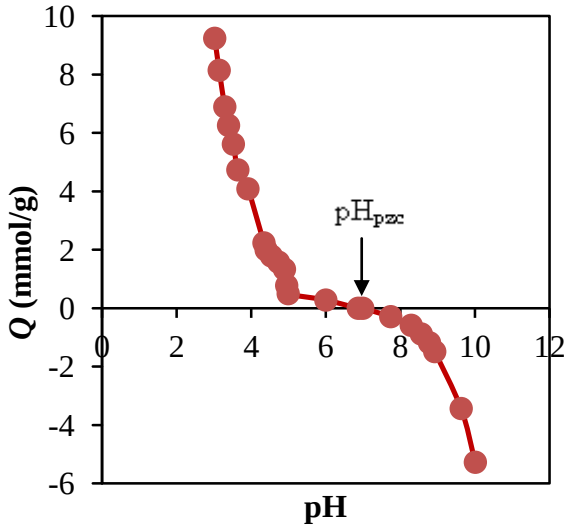

Fig. 3.8 Surface charge *Q* of alumina-silica NFs calcined at 800 °C as a function of pH.

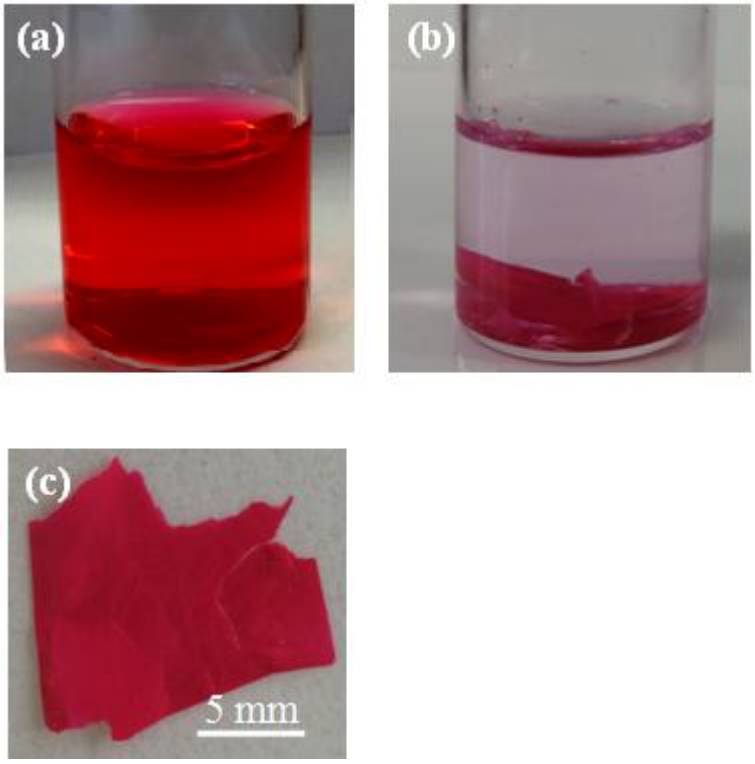

Fig. 3.9 Optical images taken (a) before and (b) after RR-120 dye adsorption by alumina-silica NFs, and (c) dye adsorbed NFs membrane. In (b) the dye-adsorbed membrane is sinking in the cleared water.

Figs. 3.9(a) and (b) show RR-120 dye solution (C_o: 74.26 mg/L, pH: 3) before and after adsorption, respectively. It can be seen from Fig. 3.9(b) that the dye containing water became clear and almost colorless after 80 hours of adsorption on alumina-silica NFs membrane. The NF membrane can be separated from the water more conveniently due to its flexible and self-standing nature compared to the conventional powdery form. Fig. 3.9(c) shows the NF membrane after dye adsorption. As shown in Fig. 3.9(c), the membrane totally became red which indicates that it has excellent adsorption capacity for RR-120 dye.

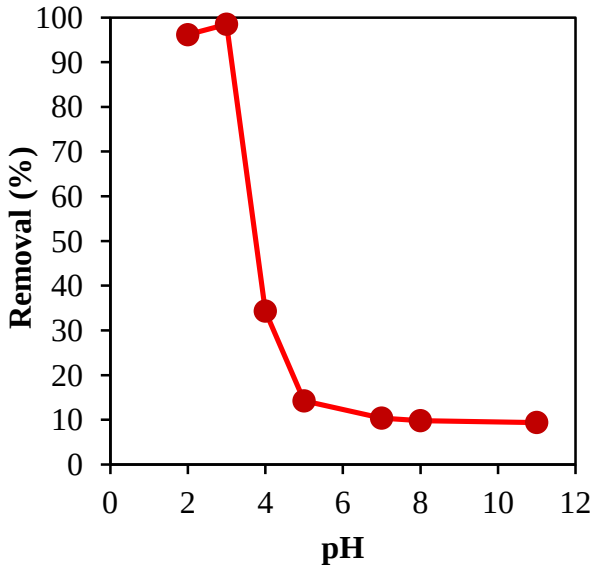

Fig. 3.10 Effect of initial pH of dye solution on the removal percentage of RR-120 onto alumina-silica NFs.

The uptake of dye is usually affected by the surface charge on the adsorbent, which in turn is influenced by the pH of dye solution. Fig. 3.10 shows the effect of initial pH of dye solution on the removal of RR-120 by alumina-silica NFs. As shown in Fig. 3.10, maximum removal percentage of dye was achieved in the pH range of 2–3. The adsorption decreased with the increase of pH rapidly from 98 to ~10%. The dye removal, however, remained nearly constant within the range of pH 7–11.

The RR-120 of which structure was shown in Fig. 3.1 is an anionic dye, which exists in aqueous solution as negatively charged species (R-SO_3^-) as

$$R\text{-}SO_3Na \rightarrow R\text{-}SO_3^- + Na^+ \qquad (3.12)$$

where R represents the rest of the dye molecule. On the other hand, in aqueous environment, aluminum oxide is covered with the hydroxyl group as Al-OH. At pH below and above pH_{pzc}, the protonation and deprotonation of alumina take place at the solid liquid interface according to the reactions shown in Eq. (3.13) and Eq. (3.14), respectively (Xu et al. 2001).

$$Al\text{-}OH + H^+ \leftrightarrow Al\text{-}OH_2^+ (positive surface) \qquad (3.13)$$

$$Al\text{-}OH + OH^- \leftrightarrow Al\text{-}O^- (negative\ surface) + H_2O \qquad (3.14)$$

At pH < pH_{pzc}, the adsorption primarily occurs due to the attractive electrostatic force between negatively charged sulfonic group ($R\text{-}SO_3^-$) of dye molecule and positively charged adsorbent surface ($Al\text{-}OH_2^+$). The abrupt decrease in the removal of dye in the pH range of 3–5 may be due to the decrease of positive charge density (Fig. 3.8) on the adsorbent surface with the increase of pH. On the contrary, at pH > pH_{pzc}, adsorption is not favorable due to the repulsive force developed between negatively charged adsorbent surface ($Al\text{-}O^-$) and dye anion ($R\text{-}SO_3^-$).

About 10% dye removal remained at pH 7–11 indicating that physical adsorption resulting from van der Waals attraction, hydrogen bonding, and inter-fibers porous structure of the NF membrane (Patel and Hota 2016; Tabak et al. 2010), or chemisorption also plays a role in the present adsorption process. RR-120, a dye-ligand molecule, is composed of two naphthalene rings, three aniline groups, and two triazine rings (Fig. 3.1). In basic medium, this offers the possibility of linking with aluminum atoms on the surface of alumina-silica NFs, by means of a nucleophilic substitution reaction between chloride of the triazine ring and deprotonated -OH group on alumina-silica NFs as shown in Eq. (3.15). Similar linkage by nucleophilic substitution reaction between chloride of triazine ring and reactive -OH group of polymer was reported by Li et al. (2014) and Bruckner (2002). The optimum solution of pH 3 was used for the subsequent experiments.

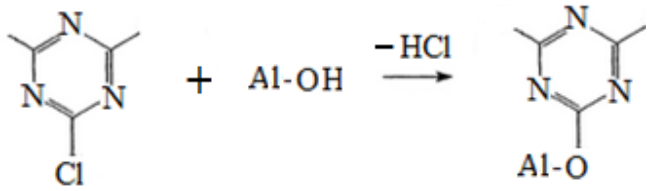

(3.15)

Chlorotriazine

3.3.6 Effect of Adsorbent (Alumina-Silica NFs) Dosage

Fig. 3.11 shows the effect of adsorbent dosage on the removal of RR-120. The percentage removal of dye increased from 93 to 98% with the increase of adsorbent dosage from 2.8 to 20 mg. This is because of the increased adsorbent surface area and greater number of adsorption sites at greater dosages of the adsorbent. Fig. 3.11 also reveals that the equilibrium adsorption density q_e, which is the adsorbed amount of dye per unit weight of adsorbent, decreased with the increase of adsorbent dosage. The decrease in q_e is due to the split in the flux or the concentration gradient of dye near the surface of the adsorbent. Similar trend has been reported in case of adsorption of crystal violet onto tea dust (Khan et al. 2016) and methylene blue (Uddin et al. 2009) onto jackfruit leaf powder.

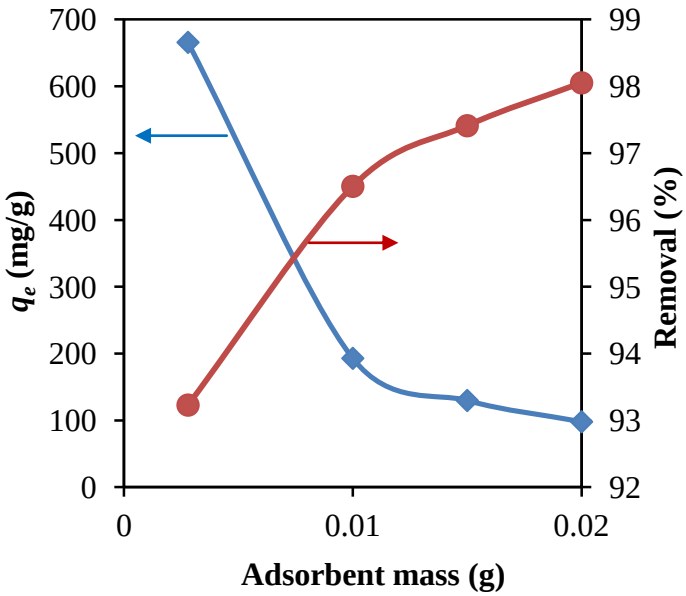

Fig. 3.11 Effect of adsorbent dosage on the adsorption density at equilibrium q_e and removal percentage of RR-120 by alumina-silica NFs.

3.3.7 Adsorption Isotherms

The adsorption equilibrium data obtained for sorption of dye onto alumina-silica NFs are fitted to Langmuir Eq. (3.5) and Freundlich Eq. (3.6) isotherm models. The fitted data is shown respectively in Figs. 3.12 and 3.13.

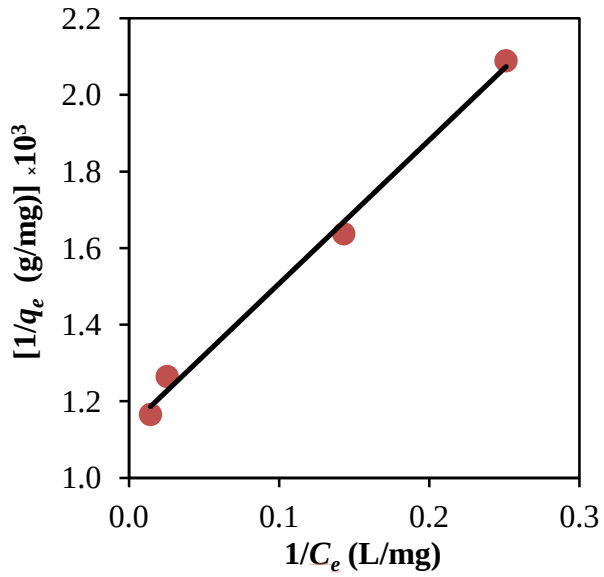

Fig. 3.12 Plots using Eq.(3.5) of Langmuir isotherm for the adsorption of RR-120 by alumna-silica NFs.

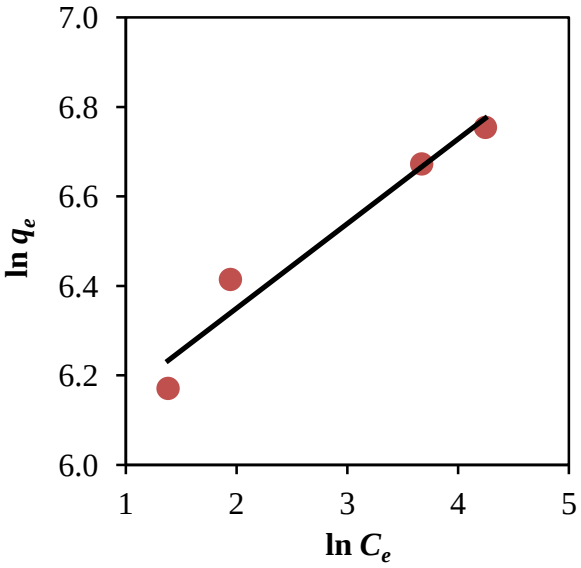

Fig. 3.13 Plots using Eq.(3.6) of Freundlich isotherm for the adsorption of RR-120 by alumina-silica NFs.

Table 3.3 Langmuir and Freudlich isotherm parameters and correlation coefficients for the adsorption of RR-120 by alumina-silica NFs

Langmuir isotherm			Freundlich isotherm		
q_m (mg/g)	K_L (L/mg)	R^2	K_F (mg/g)/(mg/L)$^{1/n}$	$1/n$	R^2
884.95	0.30	0.99	391.50	0.18	0.95

The isotherm parameters as well as correlation coefficients (R^2) are listed in Table 3.3. The R^2 values for Langmuir and Freundlich models were 0.99 and 0.95, respectively. This shows that the equilibrium data were fitted by the Langmuir isotherm equation better than the Freundlich equation implying the monolayer coverage of dye onto alumina-silica NFs. As calculated from the Langmuir model, the maximum adsorption capacity q_m of alumina-silica NFs for RR-120 is 884.95 mg dye/g NFs. In case of the Freundlich isotherm, the value of $1/n$ was estimated to be 0.18. The value smaller than unity indicates that the normal Langmuir isotherm is realized even when the model is adopted.

Table 3.4 Comparison of maximum adsorption capacity q_m of different adsorbents for RR-120 adsorption

Adsorbent	Adsorption capacity (mg/g)	References
Nanoparticles of Fe_3O_4	166.67	(Absalan et al. 2011)
Activated carbon powder	400	(Kharaisheh et al. 2002)
Spirogyra majuscule (alga) powder	273.3	(Celekli et al. 2013)
Commercial activated carbon	293.1	(Cardoso et al. 2010)
Pistachio husk powder	324.88	(Celekli et al. 2010)
Jute fiber carbon powder	200	(Senthilkumaar et al. 2006)
Cetylpyridinium-bentonite powder	81.97	(Tabak et al. 2010)
clay	29.94	(Errais et al. 2011)
Alumina-silica NFs	884.95	Present work

The monolayer adsorption capacity of several adsorbents for uptake of RR-120 dye from aqueous solution is summarized in Table 3.4. It is apparent that alumina-silica NF membrane in this study has several folds of higher adsorption capacity than the others. The above mentioned result demonstrated that the alumina-silica NFs can be used as effective adsorbent for RR-120 removal.

3.3.8 Adsorption Kinetics

Fig. 3.14 shows the adsorption of dye onto alumina-silica NFs as a function of contact time. As can be seen from the Fig. 3.14, the alumina-silica NFs continued to adsorb dye for a long time (~70 h). Similar trend was found for adsorption of 4-chlorophenol on dry biosolids (Monsalvo et al. 2012) and leachate materials on activated carbon (Zamora-Villafranco et al. 2014). The porous and dense NFs network in the membrane may be responsible for slow mass transfer and low adsorption rate.

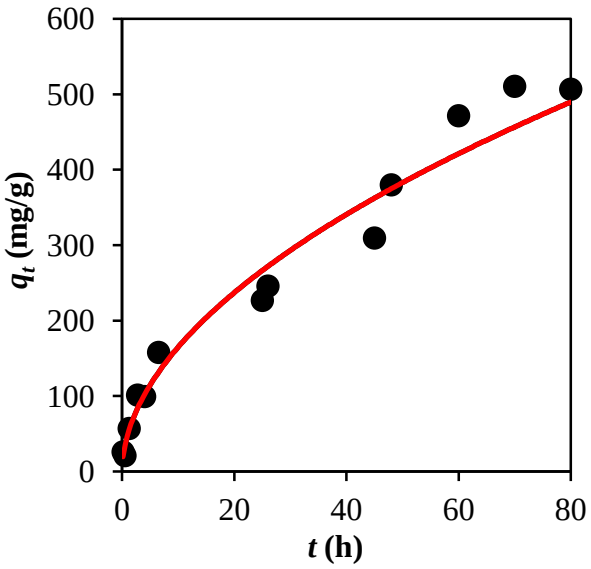

Fig. 3.14 Effect of contact time t on the adsorption density q_t of RR-120 by alumina-silica NFs.

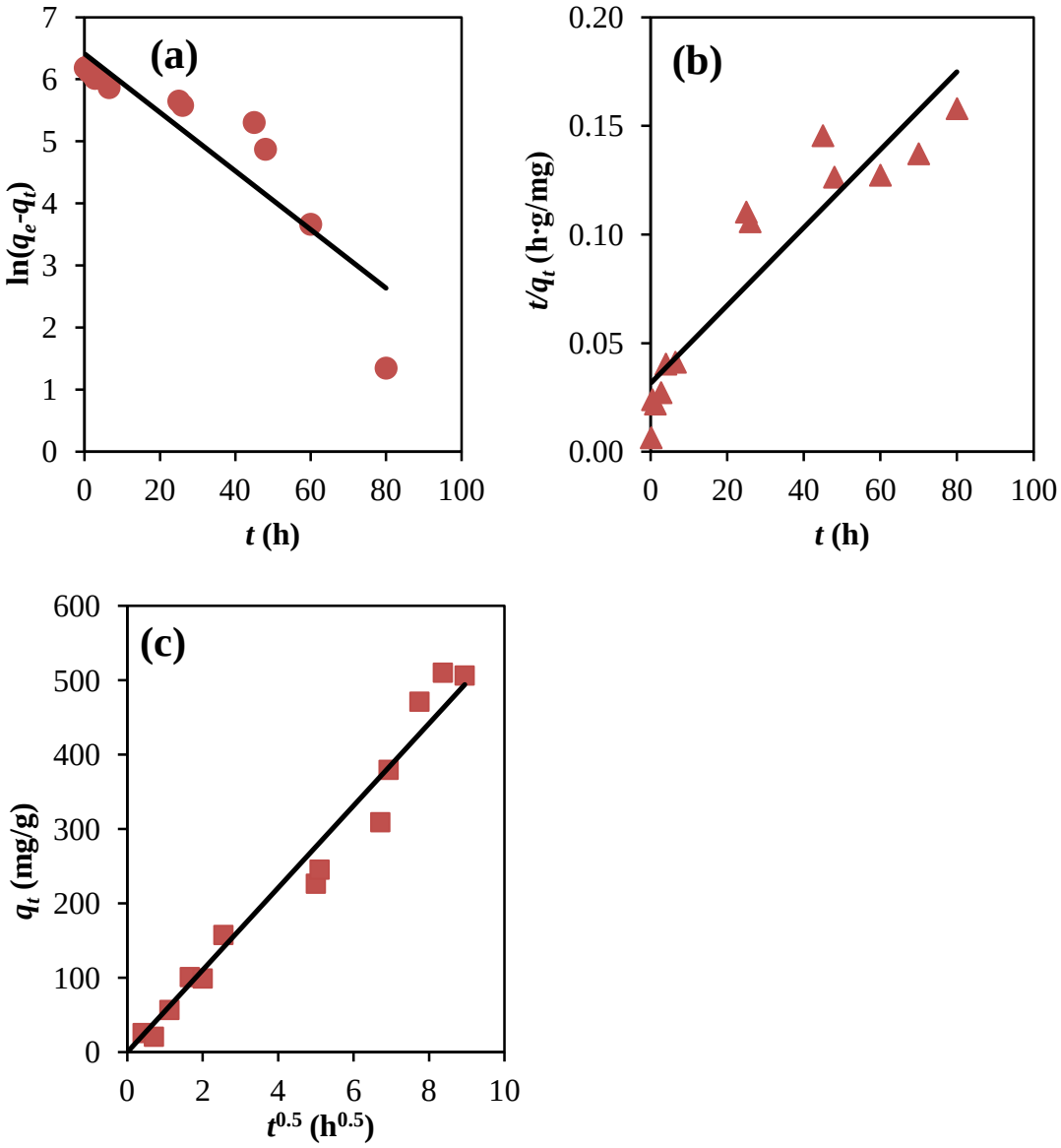

Fig. 3.15 Plots for pseudo-firstorder (a), pseudo-second-order (b), and intraparticle diffusion (c) with C_o = 74.26 mg/L and C_e = 3.34 mg/L for the adsorption of RR-120 by alumina-silica NFs using Eqs.(3.8), (3.10), and (3.11), respectively.

Figs. 3.15(a), (b) and (c) show the pseudo-first-order, pseudo-second-order and intraparticle diffusion plots for C_o = 74.26 mg/L and C_e = 3.34 mg/L based on Eqs. (3.8), (3.10), and (3.11), respectively. The calculated equilibrium adsorption capacity ($q_{e,\,calc}$) was also estimated from the fitted values of model parameters. The model parameters as well as R^2 values are presented in Table 3.5. Judging from the R^2 values, the intraparticle diffusion model in Fig. 3.15(c) showed the best fitting of the kinetic data among the three models. In addition, when the calculated q_e value ($q_{e,\,calc}$) was compared with the experimental q_e value

($q_{e,\ exp}$), the $q_{e,\ calc}$ was found to be much closer to the $q_{e,\ exp}$ for the intraparticle diffusion model.

Furthermore, as can be observed from Fig. 3.15(c), the plot of q_t versus $t^{0.5}$ results in a straight line passing through the origin, which indicates that the intraparticle diffusion is the sole rate-controlling step for the adsorption process, while the role of external film resistance is insignificant in determining the adsorption rate. A similar behavior was reported by Haitham et al. (2014) for adsorption of methyl orange on polyaniline-glass adsorbent. The intraparticle diffusion rate constant was found to be k_i = 55.266 mg/g $h^{0.5}$.

Table 3.5 Kinetic constants of RR-120 adsorption by alumina-silica NFs

Pseudo-first-order		Pseudo-second-order		Intraparticle diffusion	
$q_{e,\ exp}$ (mg/g)	506.59	$q_{e,\ exp}$ (mg/g)	506.59	$q_{e,\ exp}$ (mg/g)	506.59
$q_{e,\ calc}$ (mg/g)	608.38	$q_{e,\ calc}$ (mg/g)	555.55	$q_{e,\ calc}$ (mg/g)	494.26
k_1 (h^{-1})	0.0472	k_2 (g/mg h)	0.0001	k_i (mg/g $h^{0.5}$)	55.266
R^2	0.8259	R^2	0.8692	R^2	0.9716

3.3.9 Recovery of Dye and Reusability of Adsorbent

In order to investigate the potentiality of recovery of dye, desorption test was conducted. Initially, adsorption was performed at pH 3 (C_o = 50.176 mg/L, V= 20 mL, W= 20 mg), and the NF membrane was then withdrawn from the adsorption system and dried in air. Thereafter, desorption was carried out by contacting the dye adsorbed NF membrane with 20 mL distilled water adjusted to pH 10. After desorption, the amount of dye desorbed was obtained from the measurement of dye concentration in the solution. The recovery ratio was calculated using the following equation:

$$\text{Recovery ratio} = \frac{\text{Amount of dye desorbed}}{\text{Amount of dye adsorbed}} \tag{3.16}$$

It was estimated that the dye recovery ratio was 0.852, i.e., 85.2% of the adsorbed dye could be recovered by the swing of solution pH to 10. Because of the increase of the number of negatively charged species with high pH, the desorption of anionic dye molecules should be promoted by the electrostatic repulsion.

Furthermore, the reusability of the alumina-silica NF membrane has also been investigated. For the regeneration, the NF membrane after desorption test was washed with distilled water and thermally treated in air at 540 °C for 3h. Then the adsorption test was repeated using 20 mg of the regenerated NF mat and 20 mL of dye solution (C_o = 50.176 mg/L, pH 3). It was observed that the values of equilibrium adsorption capacity (q_e) were 46.99 and 46.28 mg/g for as-prepared and regenerated alumina-silica NF membrane, respectively. Thus, the alumina-silica NF membrane is suitable for practical application due to its reusability, and easy recovery of RR-120 dye from the dye-loaded NFs mat.

3.4 Conclusions

Self-standing nonwoven membrane of ultrafine alumina-silica NFs with excellent flexibility and mechanical strength has been fabricated via electrospinning and subsequent sintering with a partial crystallization from the mixture of amorphous silica and alumina in the NFs. Batch experiments were conducted for the removal of RR-120 dye from aqueous solution using the alumina-silica NF membrane as adsorbent. Adsorption study was carried out changing pH, adsorbent dosage and contact time. The sorption process was pH dependent and followed the Langmuir isotherm model. The maximum adsorption capacity of RR-120 dye by the NF membrane was observed as high as 884.95 mg/g, which was higher than that of the other adsorbents tried earlier by other workers. The kinetics of adsorption followed the intraparticle diffusion model. After adsorption, most of the dye could be recovered and the NF membrane could be reused as adsorbent. Because of the amorphous structure of the NFs, the mechanical properties of the membrane were improved keeping the sorption sites of aluminum atoms on the surface. Consequently, this membrane can be a practically applicable promising adsorbent material for removal and recovery of dye from aqueous solution.

References

Absalan, G., Asadi, M., Kamran, S., Sheikhian, L., & Goltz, D. M. (2011). Removal of reactive red-120 and 4-(2-pyridylazo) resorcinol from aqueous samples by Fe_3O_4 magnetic nanoparticles using ionic liquid as modifier. *Journal of Hazardous Materials*, 192, 476–484.

Aksu, Z. (2005). Application of biosorption for the removal of organic pollutants: a review. *Process Biochemistry,* 40, 997–1026.

Athanasiou, A., Mitsionis, A., Skouras, G., Todorova, N., Trapalis, C., & Vaimakis, T. (2014). Thermogravimetric study of the surfactant–diethanolamine–titanium isopropoxide system behavior. *Journal of Thermal Analysis and Calorimetry,* 116, 15–25.

Auta M. (2012). Batch adsorption of reactive red 120 from waste waters using activated carbon from waste tea. *International Journal of Advanced Engineering Technology,* III, 24–28.

Azad, A. M. (2006). Fabrication of transparent alumina (Al_2O_3) nanofibers by electrospinning. *Materials Science and Engineering: A,* 435–436, 468–473.

Bazrafshan, E., Mostafapour, F. K., Hosseini, A. R., Khorshid, A. R., & Mahvi, A. H. (2013). Decolorisation of reactive red 120 dye by using single-walled carbon nanotubes in aqueous solutions. *Journal of Chemistry,* 2013, 938374.

Bruckner, R. (2002). Advanced organic chemistry: reaction mechanisms (pp. 213–215). London: Academic Press.

Cardoso, N. F., Lima, E. C., Royer, B., Bach, M. V., Dotto, G. L., Pinto, L. A. A., & Calvete, T. (2010). Comparison of Spirulina platensis microalgae and commercial activated carbon as adsorbents for the removal of Reactive Res 120 dye from aqueous effluents. *Journal of Hazardous Materials,* 241, 146–153.

Celekli, A., Yavuzatmaca, M., & Bozkurt, H. (2010). Modeling the removal of reactive red 120 on pistachio husk. *Clean,* 38, 173 –180.

Celekli, A., İlgün, G., & Bozkurt, H. (2012). Sorption equilibrium, kinetic, thermodynamic, and desorption studies of reactive red 120 on Chara contraria. *Chemical Engineering Journal,* 191, 228–235.

Celekli, A., Yavuzatmaca, M., & Bozkurt, H. (2013). Binary adsorption of reactive red 120 and yellow 81 on Spirogyra majuscule. *Middle-East Journal of Scientific Research,* 13, 740–748.

Chakrabarty, P. K., Chatterjee, M., Naskar, M. K., Siladitya, & B., Ganguli, D. (2001). Zirconia fibre mats prepared by a sol-gel spinning technique. *Journal of the European Ceramic Society,* 21, 355–361.

Chen, M., Patra, P. K., Warner, S. B., & Bhowmick, S. (2007). Role of fiber diameter in adhesion and proliferation of NIH 3T3 fibroblast on electrospun polycaprolactone scaffolds. *Tissue Engineering,* 13, 579–87.

Cherepy, N. J., Shen, T. H., Esposito, A. P., & Tillotson, T. M. (2005). Characterization of an effective cleaning procedure for aluminum alloys: surface enhanced raman Spectroscopy and zeta potential analysis. *Journal of Colloid and Interface Science,* 282, 80–86.

Dabbagh, H. A., & Shahraki, M. (2013). Mesoporous nanorod-like γ-alumina synthesis using phenol–formaldehyde resin as a template. *Microporous Mesoporous Materials,* 175, 8–15.

Dai, H., Gong, J., Kim, H., & Lee, D, (2002). A novel method for preparing ultra-fine alumina-borate oxide fibres via an electrospinning technique. *Nanotechnology,* 13, 674–677.

Demarchi, C. A., Campos, M., & Rodrigues, C. A. (2013). Adsorption of textile dye reactive red 120 by the chitosan–Fe (III) crosslinked: batch and fixed-bed studies. *Journal of Environmental Chemical Engineering,* 1, 1350–1358.

Deng, D., Tang, R., Liao, X., & Shi, B. (2008). Using collagen fiber as a template to synthesize hierarchical mesoporous alumina fiber. *Langmuir,* 24, 368–370.

Dos Santos, J. M., Felsner, M. L., Almeida, C. A. P., & Justi, K. C. (2016). Removal of reactive orange 107 dye from aqueous solution by activated carbon from *Pinus elliottii* sawdust: a response surface methodology study. *Water, Air, & Soil Pollution,* 227, 300, 1–14.

Errais, E., Duplay, J., Darragi, F., M'Rabet, I., Aubert, A., Huber, F., & Morvan, G. (2011). Efficient anionic dye adsorption on natural untreated clay: kinetic study and thermodynamic parameters. *Desalination,* 275, 74–81.

Faulques, E., Fritsch, E., & Ostroumov, M. (2001). Spectroscopy of natural silica-rich glasses. *Journal of Mineralogical and Petrological Sciences*, 96(3), 120–128.

Fytianos, K., Voudrias, E., & Kokkalis, E. (2000). Sorption-desorption behavior of 2,4-dichlorophenol by marine sediments. *Chemosphere*, 40, 3–6.

Geethakarthi, A., & Phanikumar, B. R. (2011). Adsorption of reactive dyes from aqueous solutions by tannery sludge developed activated carbon: kinetic and equilibrium studies. *International Journal of Environmental Science and Technology,* 8, 561–570.

Gowri, R. S., Vijayaraghavan, R., & Meenambigai, P. (2014). Microbial degradation of reactive dyes–a review. *International Journal of Current Microbiology and Applied Sciences,* 3, 421–436.

Karcher, S., Kornmuller, A., & Jekel, M. (2001). Screening of commercial sorbents for the removal of reactive dyes. *Dyes and Pigments,* 51, 111–125.

Haitham, K., Razak, S., & Nawi, M. A. (2014). Kinetics and isotherm studies of methyl orange adsorption by a highly recyclable immobilized polyaniline on a glass plate. *Arabian Journal of Chemistry,* http://dx.doi.org/10.1016/j.arabjc.2014.10.010

Horiuchi, T., Osaki, T., Sugiyama, T., Suzuki, K., & Mori, T. (2001). Maintenance of large surface area of alumina heated at elevated temperatures above 1300 °C by preparing silica-containing pseudoboehmite aerogel. *Journal of Non-Crystalline Solids*, 291, 187–198.

Ho, Y. S., & McKay, G. (1998). Sorption of dye from aqueous solution by peat. *Chemical Engineering Journal*, 70, 115–124.

Hou, H., Zhou, R., Wu, P., & Wu, L. (2012). Removal of Congo red dye from aqueous solution with hydroxyapatite/chitosan composite. *Chemical Engineering Journal*, 211–212, 336–342.

Hu, J., Song, Z., Chen, L., Yang, H., Li, J., & Richards, R. (2010). Adsorption properties of MgO (111) nanoparticles for the dye pollutants from wastewater. *Journal of Chemical &*

Engineering Data, 55, 3742–3748.

Khan, M. M. R., Rahman, M. W., Ong, H. R., Ismail, A. B., & Cheng, C. K. (2016). Tea dust as a potential low-cost adsorbent forthe removal of crystal violet from aqueous solution. *Desalination and Water Treatment,* 57, 14728–14738.

Kharaisheh, M. A. M., Al Degs, Y. S, Allen, S. T., & Ahmad, M. N. (2002). Elucidation on controlling steps of reactive dye adsorption on activated carbon. *Industrial & Engineering Chemistry Research,* 41, 1651–1657.

Khoshhesab, Z. M., & Ahmadi, M. (2016). Removal of reactive blue 19 from aqueous solutions using NiO nanoparticles: equilibrium and kinetic studies. *Desalination and Water Treatment,* 57, 20037–20048.

Khoshkhan, Z., & Saleh, M. (2014). New method for preparation of nano alumina powder using aluminum (III) complexes by combustion synthesis without fuel. *Journal of Nanostructures,* 4, 443–448.

Kiefer, E., Sigg, L., & Schosseler, P. (1997). Chemical and spectroscopic characterization of algae surfaces. *Environmental Science* & *Technology,* 31, 759–764.

Kingma, K. J., & Hemley, R. J. (1994). Raman spectroscopic study of microcrystalline silica. *American Mineralogist,* 79, 269–273.

Kittinaovarat, S., Kansomwan, P., & Jiratumnukul, N. (2010). Chitosan/modified montmorillonite beads and adsorption reactive red 120. *Applied Clay Science,* 48, 87–91.

Lagergren, S. (1898). About the theory of so-called adsorption of soluble substance. *Kungliga Svenska Vetenskapsakademiens, Handlingar,* 24, 1–39.

Langmuir, I., (1916). The constitution and fundamental properties of solids and liquids. *Journal of the American Chemical Society,* 8, 2221–2295.

Li, D., McCann, J. T., Xia, Y., & Marquez, M. (2006). Electrospinning: a simple and versatile

technique for producing ceramic nanofibers and nanotubes. *Journal of the American Ceramic Society,* 89, 1861–1869.

Li, L., Kang, W., Zhao, Y., Li, Y., Shi, J., & Cheng, B. (2015). Preparation of flexible ultra-fine Al_2O_3 fiber mats via the solution blowing method. *Ceramics International,* 41, 409–415.

Liu, P., Feng, J., Zhang, X., Lin, Y., Evans, D. G., & Li, D. (2008). Preparation of high purity spherical γ-alumina using a reduction-magnetic separation process. *Journal of Physics and Chemistry of Solids,* 69, 799–804.

Li, Z., Cao, M., Zhang, W., Liu, L., Wang, J., Ge, W., Yuan, Y., Yue, T., Li, R., & Yu, W. W. (2014). Affinity adsorption of lysozyme with reactive red 120 modified magnetic chitosan microspheres. *Food Chemistry,* 145, 749–755.

Mahapatra, A., Mishra, B. G., & Hota, G. (2013). Adsorptive removal of Congo red dye from wastewater by mixed iron oxide–alumina nanocomposites. *Ceramics International,* 39, 5443–5451.

Malinovsky, V. K., Novikov, V. N., Surovtsev, N. V., & Shebanin, A. P. (2000). Investigation of amorphous states of SiO_2 by raman scattering spectroscopy. *Physics of the Solid State,* 42(1), 65–71.

McKay G. (1981). Design models for adsorption systems in wastewater treatment. *Journal of Chemical Technology* and *Biotechnology,* 31, 717–731.

Mitsuda, K., Kimura, H., & Murahashi, T. (1989). Evaporation and decomposition of Triton X-l00 under various gases and temperatures. *Journal of Materials Science,* 24, 413–419.

Monsalvo, V. M., Mohedano, A. F., & Rodriguez, J. J. (2012). Adsorption of 4-chlorophenol by inexpensive sewage sludge-based adsorbents. *Chemical Engineering Research and Design,* 90, 1807–1814.

Mukhlish, M. Z. B., Horie, Y., Higashi, K., Ichigi, A., Guo, S., & Nomiyama, T., (2017). Self-standing conductive ITO-silica nanofiber mats for use in flexible electronics and their

application in dye-sensitized solar cells. *Ceramics International,* 43, 8146–8152.

Nethajia, S., Sivasamya, A., Thennarasua, G., & Saravanan, S. (2010). Adsorption of malachite green dye onto activated carbon derived from Borassus aethiopum flower biomass. *Journal of Hazardous Materials,* 181, 271–280.

Noorimotlagh, Z., Soltani, R. D. C., Khataee, A., Shahriyar, S., & Nourmoradi, H. (2014). Adsorption of a textile dye in aqueous phase using mesoporous activated carbon prepared from Iranian milk vetch. *Journal of the Taiwan Institute of Chemical Engineers,* 45, 1783–1791.

Nourmoradi, H., Rahmati, Z., Javaheri, M., Moradnejadi, K., & Noorimotlagh, Z. (2015). Effect of praestol as a coagulant-aid to improve coagulation-flocculation in dye containing wastewaters. *Global NEST Journal,* 18, 38–46.

Patel, S., & Hota, G. (2016). Iron oxide nanoparticle-immobilized PAN nanofibers: synthesis and adsorption studies. *RSC Advances,* 6, 15402–15414.

Paul, J., Rawat, K. P., Sarma, K. S. S., & Sabharwal, S. (2011). Decoloration and degradation of reactive red-120 dye by electron beam irradiation in aqueous solution. *Applied Radiation and Isotopes,* 69, 982–987.

Peskova, S., Machovic, V., & Prochazka, P. (2011). Raman spectroscopy structural study of fired concrete. *Ceramics–Silikáty,* 55(4), 410–417.

Poursaberi, T., & Hassanisadi, M. (2013). Magnetic removal of reactive black 5 from wastewater using ionic liquid grafted-magnetic nanoparticles. *Clean: Soil Air Water,* 41, 1208–1215.

Richet, P., Mysen, B. O., & Ingrin, J. (1998). High-temperature X-ray diffraction and Raman spectroscopy of diopside and pseudowollastonite. *Physics and Chemistry of Minerals,* 25, 401–414.

Riera-Torres, M., Gutiérrez-Bouzán, C., & Crespi, M. (2010). Combination of coagulation–

flocculation and nanofiltration techniques for dye removal and water reuse in textile effluents. *Desalination,* 252, 53–59.

Sato, T., Ikoma, S., & Ozawa, F. (1984). Thermal decomposition of organic basic aluminium salts-formate and acetate. *Thermochimica Acta,* 75, 129–137.

Schram, T., De Laet, J., & Terryn, H. (1998). Nondestructive optical characterization of chemical conversion coatings on aluminum. *Journal of The Electrochemical Society,* 145(8), 2733–2739.

Senthilkumaar, S., Kalaamani, P., Porkodi, K., Varadarajan, P. R., & Subburaam, C. V. (2006). Adsorption of dissolved reactive red dye from aqueous phase onto activated carbon prepared from agricultural waste. *Bioresource Technology,* 97, 1618–1625.

Shi, C., Lv, C., Wu, L., & Hou, X. (2017). Porous chitosan/hydroxyapatite composite membrane for dyes static and dynamic removal from aqueous solution. *Journal of Hazardous Materials,* 338, 241–249.

Singha, M., & Singh, L. (2016). Vibrational spectroscopic study of muscovite and biotite layered phyllosilicates. *Indian Journal of Pure and Applied Physics,* 54, 116–122.

Tabak, A., Baltas, N., Afsin, B., Emirik, M., Caglar, B., & Eren, E. (2010). Adsorption of reactive red 120 from aqueous solutions by cetylpyridinium-bentonite. *Journal of Chemical Technology* and *Biotechnology,* 85, 1199–1207.

Tan, E. P. S., & Lim, C. T. (2004). Physical properties of a single polymeric nanofiber. *Applied Physics Letters,* 84, 1603–1605.

TAN, H., & GUO, C. (2011). Preparation of long alumina fibers by sol-gel method using malic acid. *Transactions of Nonferrous Metals Society of China,* 21, 1563−1567.

Thomas, P. V., Ramkrishnan, V., & Vaidyan, V. K. (1989). Oxidation studies of aluminum thin films by Raman spectroscopy. *Thin Solid Films,* 170(1), 35–40.

Timken, H. K. (2005). Method for preparing a highly homogeneous amorphous silica-alumina composition. Patent N0.: US 6,872,685 B2.
http://www.google.com/patents/US6872685. Accessed 30 Apr 2017.

Tlili, A., Smith, D. C., Beny, J. M., & Boyer, H. (1989). A Raman microprobe study of natural micas. *Mineralogical Magazine,* 53(370), 165–179.

Tsai, J. H., Chiang, H. M., Huang, G. Y., & Chiang, H. L. (2008). Adsorption characteristics of acetone, chloroform and acetonitrile on sludge-derived adsorbent, commercial granular activated carbon and activated carbon fibers. *Journal of Hazardous Materials,* 154, 1183–1191.

Uddin, M. T., Rukanuzzaman, M., Khan, M. M. R., & Islam, M. A. (2009). Jackfruit (Artocarpus Heterophyllus) leaf powder: An effective adsorbent for removal of methylene blue from aqueous solutions. *Indian Journal of Chemical Technology,* 16, 142–149.

Vijayaraghavan, J., Basha, S. J. S., & Jegan, J. (2013). A review on efficacious methods to decolorize reactive azo dye. *Journal of Urban and Environmental Engineering,* 7, 30–47.

Weber, W. J., & Morris, J. C. (1963). Kinetics of adsorption on carbon from solutions. *Journal Sanitary Engeering Division Proceedings. American Society of Civil Engineers,* 89, 31–60.

Wu, N., Wei, H., & Zhang, L. (2012). Efficient removal of heavy metal ions with biopolymer template synthesized mesoporous titania beads of hundreds of micrometers size. *Environtal Science and Technology,* 46, 419−425.

Xu, G.-R., Wang, J.-N., & Li, C.-J. (2012). Preparation of hierarchically nanofibrous membrane and its high adaptability in hexavalent chromium removal from water. *Chemical Engineering Journal,* 198–199, 310–317.

Xu, X., Liu, Y., Li, Z., Lv, Z., Song, J., He, M., Wang, Q., Yan, L., & Li, Z. (2014). Thermal study of boehmite nanofibers with controlled particle size. *Journal of Thermal Analysis and Calorimetry,* 115, 1111–1117.

Xu, Y.-H., Ohki, A., & Maeda, S. (2001). Adsorption and removal of antimony from aqueous solution by an activated alumina. *Toxicological & Environmental Chemistry,* 80, 133–144.

Yoshida, H., Matsushita, N., Kato, Y., & Hattori, T. (2002). Active sites in sol–gel prepared silica-alumina for photoinduced non-oxidative methane coupling. *Physical Chemistry Chemical Physics*, 4, 2459–2465.

Zafar, M. S., Tausif, M., Mohsin, M., Ahmad, S. W., & Zia-ul-Haq, M. (2015). Potato starch as a coagulant for dye removal from textile wastewater. *Water, Air, & Soil Pollution,* 226, 244, 1–11.

Zamora-Villafranco, E., Barceló-Quintal, I. D., Gomez-Salazar, S., Barceló-Quintal, M., Solís-Correa, H. E., & Soriano-Rodríguez, J. M. (2014). Adsorption kinetics of matter contained in a leachate using eggshell and activated carbon. *Journal of Environmental Protection,* 5, 608–619.

Zhang, P., Chen, D., & Jiao, X. (2012). Fabrication of flexible α-alumina fibers composed of nanosheets. *European Journal of Inorganic Chemistry,* 2012, 4167–4173.

CHAPTER 4

FLEXIBLE ALUMINA-SILICA/IRON OXIDE CORE-SHEATH NANOFIBROUS MEMBRANES AND THEIR STRONG REACTIVE RED-120 DYE REMOVAL PERFORMANCES

4.1 Introduction

Dye and dye stuffs are extensively used in various industries such as textile, plastic, leather, food, cosmetic, printing and paper. Release of dye containing wastewaters generated from these industries into water resources causes damage to ecological balance and affects photosynthetic activity (Absalan et al. 2011). Moreover, reactive azo dyes are potentially carcinogenic, toxic and mutagenic compounds, also recalcitrant and highly persistent in natural environment. Consequently, their discharge into the environment poses a serious risk to the human health and aquatic organisms (Noorimotlagh et al. 2014; Celekli et al. 2012). In addition, this type of dyes tends to pass through conventional treatment systems unaffected. Therefore, it is crucial to remove the residual dyes from the wastewater before it is discharged.

A variety of ways have been investigated for removing reactive dyes from colored wastewaters, such as biological treatment, chemical coagulation, membrane filtration, electrocoagulation and adsorption (Arıca and Bayramoglu 2007; Zafar et al. 2015; Hou et al. 2012; Shi et al. 2017; Alinsafi et al. 2005). Among these techniques for dyes removal, adsorption is considered as the most promising method due to its simple operation, low cost, and high efficiency. Moreover, it does not produce harmful substances (Absalan et al. 2011).

Nanostructured powder adsorbents have been employed as attractive candidates in the field of adsorption (Ghaedi et al. 2012; Absalan et al. 2011; Hu et al. 2010; Moussavi et al. 2009) due to their high surface area compared to their bulk counterpart. But powder like nano-adsorbents tend to aggregate easily to reduce their surface area and surface energy. In addition, it is found to be very difficult or energetically cost-ineffective to separate the dye loaded powder adsorbents from the wastewater after use, which causes secondary environmental pollution. The above features of powdered adsorbents limit their scope for practical applications (Shi et al. 2017; Motlagh et al. 2014). In contrast to powder materials, self-standing and nonwoven nanofibrous membrane can be an effective alternative, which can easily overcome the drawbacks of powder adsorbents, while retaining high sorption

performance together with easy separation property (Xu et al. 2012; Mukhlish et al. 2017).

Among various metal oxides, the oxides of aluminum and iron have large advantages because of their low cost, extensive availability, thermal stability and remarkable adsorption capacity (Mahapatra et al. 2013). Consequently, iron oxide and aluminum oxide or their combinations have gained much attention for adsorptive removal of pollutant from wastewaters. For example, Tchieda et al. (2016) studied the adsorption of arsenic ions on alumina particle, Li et al. (2011) reported the adsorption of arsenic and lead ions on α-FeOOH microsphere, Mahapatra et al. (2013) investigated the adsorption of Congo red dye on mixed iron oxide–alumina nanoparticles, and Khosravi et al. (2014) prepared iron oxide nanospheres for the removal of reactive dyes such as reactive orange and reactive yellow.

Reactive Red-120 (RR-120) is one of the frequently used dyes in textile industries and is a potential threat to the aquatic environment due to its poor biodegradability (Paul et al. 2011). In order to investigate sorption efficiency for removing of RR-120, different adsorbents such as *Chara contraria* (alga) powder (Celekli et al. 2012), *Lentinus sajor-caju* (fungus) biomass (Arıca and Bayramoglu 2007), pistachio husk (Celekli et al. 2010), activated oil palm ash (Hameed et al. 2009), metal hydroxide sludge (Netpradit et al. 2003), clay (Errais et al. 2011), Fe_3O_4 nanoparticles (Absalan et al. 2011), single-walled carbon nanotubes (Bazrafshan et al. 2013), and activated carbon powder (Kharaisheh et al. 2002) have been used. But these adsorbents showed poor adsorption performance and the adsorption capacity was less than 500 mg/g.

With the aim of enhanced adsorption, we developed alumina-silica nanofibrous membrane in our previous study which exhibited adsorption capacity of 884.95 mg/g for RR-120 dye removal (Mukhlish et al. 2017). For further improvement of adsorption performance, we have proposed porous iron oxide sheath layer on the alumina-silica nanofibers (NFs). The porous iron oxide sheath layer will provide active sites for adsorption, whereas alumina-silica core will act as support for sheath layer. In addition, the surface of the core part exposed to the pores will also take part in adsorption. Xu et al. (2012) prepared TTEP (thermal plastic elastomer ester) supported iron oxide NFs and used for adsorption of chromium from water. Patel and Hota (2016) fabricated PAN (Polyacrylonitrile)/iron oxide (IO) composite membrane and iron oxide coated PAN NF membrane, and used for congo red dye adsorption from aqueous solution. To our best knowledge, there is no report on the preparation of alumina-silica/iron oxide core-sheath NFs as well as their application in adsorption of dye.

In the present study, we have prepared nonwoven membranes of coaxial NFs of alumina-silica core and iron oxide sheath with different sheath morphology by

electrospinning method, and studied their effect on the adsorption of RR-120 dye from aqueous solution. The self-standing membranes will exhibit interesting characteristics such as high porosity, high specific surface area, and interconnected open pore structures which facilitate mass transfer and provide sufficient active sites for dye adsorption. In addition, the self-standing and flexible nature of the membranes will facilitate post-adsorption separation from the liquid phase. The adsorption experiments such as effect of pH, adsorbent dose and contact time on the sorption of RR-120 dye were investigated in batch experiments as those in Chapter 3. The adsorption thermodynamic, isotherm and kinetic studies were also conducted to explore the adsorption mechanism. In order to reveal the possibility of recovery of adsorbent and adsorbate, desorption studies were carried out.

4.2 Materials and Methods

4.2.1 Materials

Polyvinyl pyrrolidone (PVP, M_w = 360,000), formic acid (98.0%), acetic acid (97.7%), hydrochloric acid (HCl), sodium hydroxide (NaOH), aluminum powder, iron (II) chloride tetrahydrate ($FeCl_2.4H_2O$) and iron (III) chloride hexahydrate ($FeCl_3.6H_2O$) were obtained from Wako. PVP (M_w = 1,300,000), tetra ethyl ortho silicate (TEOS, 98%), poly(ethylene glycol)-block-poly(propylene glycol)-block-poly(ethylene glycol) (PEG-PPG-PEG, pluronic P-123, molar mass, M_n = 5800 g/mol) and Reactive Red-120 (RR-120) dye were purchased from Sigma-Aldrich whereas triton X-100 (TX) was obtained from Alfa Aesar. The stock solutions of RR-120 (500 mg/L) were prepared in distilled water, and working solutions were obtained by appropriate dilution. The RR-120 ($C_{44}H_{24}C_{l2}N_{14}Na_6O_{20}S_6$) is an anionic dye, which exists in aqueous solution as negatively charged species ($R\text{-}SO_3^-$) as:

$$R\text{-}SO_3Na \rightarrow R\text{-}SO_3^- + Na^+ \quad (4.1)$$

where R represents the rest of the dye molecule (Mukhlish et al. 2017). Pluronic P-123 (Poly(ethylene glycol)-block-poly(propylene glycol)-block-poly(ethylene glycol)) is a triblock copolymer used as pore forming agent.

4.2.2 Preparation of Alumina-Silica/Iron Oxide Core-Sheath NF Membrane

(a) Preparation of core solution (spin dope for alumina-silica)

The spin dope for alumina-silica core was prepared following the same method used for the preparation of alumina-silica NFs (Mukhlish et al. 2017) except the change in the amount of TX. In brief, at first, formic acid, acetic acid and water were mixed at a volume ratio of 1:1:3 (solution A). Then, 30 mL of solution A and 1.0 g of aluminum powder was mixed and heated at 85 $^{\circ}$C under reflux for about 72 h. In order to remove a small amount of residual impurities, the solution was filtered and the obtained filtrate solution (solution B) was used as precursor for the preparation of spin dope for alumina-silica core. The spin dope for alumina-silica core was obtained by the addition of 2.5 mL solution B, 0.1 mL TEOS, 0.25 g PVP (M_w = 360,000), and 0.2 mL TX (20% aqueous) followed by stirring for 2 h.

(b) Preparation of sheath solution (spin dope for iron oxide)

In order to prepare the sheath solution for iron oxide, at first, PVP solution (solution C) and P-123 solution (solution D) were prepared by adding 1.0 g PVP (M_w = 1,300,000) to 7.0 mL ethanol, and 1.0 g Pluronic P-123 to 4 mL distilled water, respectively. Then, 0.5 g $FeCl_3.6H_2O$ and 0.5 g $FeCl_2.4H_2O$ were dissolved in 2 mL distilled water followed by the addition of 1.0 mL solution D and stirring for 12 h (solution E). Finally, 4.0 g solution C and 1.0 ml TX (20% aqueous) was added to the solution E followed by stirring for 5 h to get spin dope for iron oxide.

(c) Preparation of core-sheath NFs

Fig. 4.1 shows the basic mechanism of coaxial electrospinning for the preparation of core-sheath NFs. The core solution for alumina-silica and the sheath solution for iron oxide were transferred into two syringes equipped with a coaxial nozzle (core needle: 27 gauge) made of stainless steel, and three nanofibrous membranes designated as CS-1, CS-2 and CS-3 were prepared by an electrospinning apparatus (MECC NANON-05) on flat pieces of aluminum foil. The electrospinning process was carried out in air under applied voltage 25 kV, humidity < 30% and nozzle tip to aluminum foil collector distance 15 cm, while the feed rate of core solution was maintained at 0.4 mL/h and that of sheath solution was varied as shown in

Table 4.1. The as-spun nanofibrous membrane on the aluminum foil was immediately put in an oven for drying, because the wet gel NFs can easily join each other forming thick connections which may become centers of crack formation during subsequent calcination (Chakrabarty et al. 2001).

Table 4.1 Samples compared in this study together with the feed rates of core and sheath solutions during electrospinning

Sample name	Feed rate (mL/h)	
	Core solution	Sheath solution
Core	0.4	–
CS-1	0.4	1.5
CS-2	0.4	2.5
CS-3	0.4	4.0

The flexible and self-standing core-sheath membranes of alumina-silica/iron oxide NFs were achieved after calcination in a furnace at 600 °C for 2h at a heating rate of 2 °C/min. During calcination, solvents and organic components of the as-electrospun composite NFs were removed and inorganic NFs were obtained. The alumina-silica core NF membrane without sheath layer designated as Core was also prepared by using the same method setting the feed rate of sheath solution to be zero during the electrospinning.

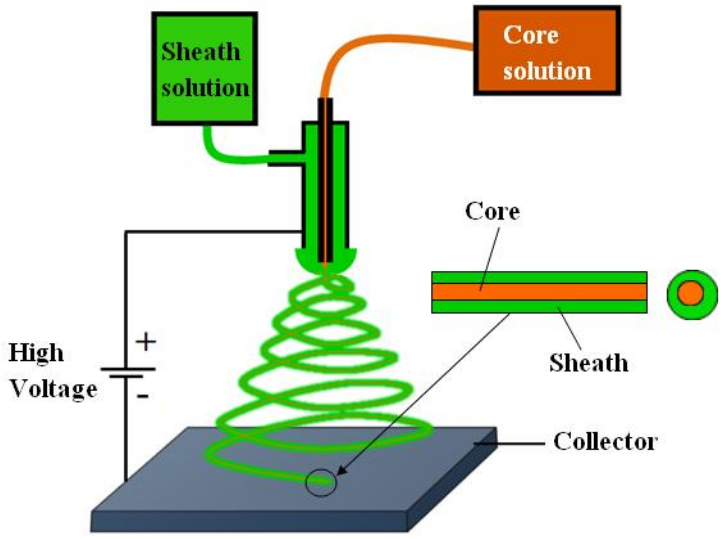

Fig. 4.1 Schematic diagram of core-sheath electrospinning.

4.2.3 Characterization of NF Membrane

The morphology and phase of the alumina-silica/iron oxide NF membranes were observed by field-emission scanning electron microscope (FE-SEM, Hitachi SU-70), Transmission electron microscope (TEM, JEOL JEM-3010) and X-ray diffractometer (XRD, PANalytical X'Pert PRO MPD). The elemental compositions of the fibers were obtained by energy-dispersive X-ray (EDX, Hitachi SU-70) spectroscopy analysis. A UV-visible spectrophotometer (Hitachi U-3900) was used for measuring absorbance of dye solution.

4.2.4 Determination of Surface Charge and pH at the Point of Zero Charge

The titration method reported by Kiefer et al. (1997) was used to determine the pH at the point of zero charge (pH_{pzc}) of the alumina-silica/iron oxide NF membrane (CS-1) in aqueous phase and also the surface charge *Q* at different pH. The experimental conditions and procedure were same as discussed in Chapter 3 (Section 3.2.4). The surface charge *Q* of alumina-silica/iron oxide NFs was calculated from the experimental titration data using the equation (Kiefer et al. 1997),

$$Q = \frac{1}{w}(C_A - C_B - [\mathrm{H^+}] - [\mathrm{OH^-}]) \qquad (4.2)$$

where *w* is the dry weight of adsorbent in aqueous system (g/L), C_A is the concentration of added acid in aqueous system (mol/L), C_B is the concentration of added base in aqueous system (mol/L), $[H^+]$ and $[OH^-]$ are the concentration (mol/L) of H^+ and OH^- at different equilibrium pH of the system, respectively.

4.2.5 Batch Sorption Experiments

The adsorption tests were performed by batch technique at average room temperature of 25 $^{\circ}$C using the same procedure mentioned in Chapter 3 (Section 3.2.5).

The effect of initial dye solution pH on the adsorptive removal of dye was studied over the pH range of 3 to 9. In this study, the pH of initial dye solution (100 mg/L) was maintained at a desired value by the addition of 0.1 M HCl or NaOH, and the adsorbent (CS-1) mass was maintained at 2.8 mg for 20 mL dye solution. The effect of the adsorbent mass was studied by contacting 20 mL dye solution of initial concentration 100 mg/L and pH 3

with different amount of CS-1 (0.8–5.6 mg) till the equilibrium was achieved. In case of thermodynamic studies, the adsorption experiments were performed with 2.8 mg CS-1 adsorbent at temperatures of 25 °C, 40 °C and 65 °C. The initial dye solution concentration and pH were fixed at 400 mg/L and 3, respectively.

The adsorption equilibrium experiments were conducted by soaking 2.8 mg alumina-silica/iron oxide NFs (either CS-1, CS-2 or CS-3) into 20 mL dye solution with various initial concentrations of 100–500 mg/L at pH of 3. Each experiment was carried out for 100 h for the attainment of adsorption equilibrium, and the residual dye concentration in the supernatant solution was measured as mentioned earlier.

The batch kinetic tests were performed by adding 2.8 mg of adsorbent (either CS-1, CS-2, CS-3 or Core) in 20 mL dye solution with an initial concentration of 100 mg/L at pH of 3. The aqueous samples were withdrawn at different time intervals. The concentrations of dye were then measured.

The adsorption density defined as the amount of dye (RR-120) adsorbed per unit weight of adsorbent (alumina-silica/iron oxide NFs) was evaluated by using the following equations:

$$q_e = \frac{(C_o - C_e)V}{W}, \tag{4.3}$$

$$q_t = \frac{(C_o - C_t)V}{W}, \tag{4.4}$$

where q_e and q_t are the adsorption density (mg/g) at equilibrium and at time t, respectively. C_o, C_t, and C_e represent the dye concentrations (mg/L) at initial, at time t, and at equilibrium, respectively. V is the volume of solution (L), and W is the mass of adsorbent (g). The percentage removal of dye at time t was calculated using

$$\text{Removal}\ (\%) = \frac{100(C_o - C_t)}{C_o}. \tag{4.5}$$

4.2.6 Thermodynamic Study

The thermodynamic parameters, like change in Gibbs free energy (ΔG^o, kJ/mol), enthalpy (ΔH^o, kJ/mol), and entropy (ΔS^o, J/mol K) associated with the sorption process can be used to deduce the sorption mechanism. These parameters were estimated using the following equations (Chatterjee et al. 2005; Hameed et al. 2009):

$$\Delta G^o = -RT \ln K_d \tag{4.6}$$

$$\ln K_d = \frac{\Delta S^o}{R} - \frac{\Delta H^o}{RT} \tag{4.7}$$

where R (= 8.314 J mol^{-1} K^{-1}) is the universal gas constant, T (K) is the absolute solution temperature and K_d is the distribution coefficient defined as:

$$K_d = \frac{q_e}{C_e} \tag{4.8}$$

where q_e (mg/g) is the amount dye adsorbed on adsorbent at equilibrium and C_e (mg/L) is the equilibrium dye solution concentration. The values of ΔH^o and ΔS^o can be determined from the slope and intercept of the linear plot of lnK_d versus 1/T.

4.2.7 Adsorption Isotherms

The adsorption isotherm is the equilibrium relationship between the amount of adsorbate per unit of adsorbent (q_e) and its equilibrium concentration (C_e) at a constant temperature. In general, the adsorption isotherm plays an important role in the predictive modeling procedures for the analysis of an adsorption system (Agcaoili et al. 2017). In the present study, the experimental equilibrium data of dye adsorption on alumina-silica/iron oxide NFs were analyzed using Langmuir (Langmuir 1916) and Freundlich (McKay 1981) isotherm models given by the following equations, respectively,

Langmuir: $$q_e = \frac{q_m K_L C_e}{1 + K_L C_e} \tag{4.9}$$

Freuindlich: $$q_e = K_F C_e^{\frac{1}{n}} \tag{4.10}$$

where q_m is the maximum adsorption capacity (mg/g) and K_L is Langmuir constant related to the free energy of adsorption. K_F and n are Freuindlich constants representing the quantity of dye adsorbed on adsorbent for unit equilibrium concentration (*i.e.*, C_e =1) and the adsorption intensity, respectively.

The Langmuir model is valid for monolayer adsorption onto a surface with a finite number of identical sites which are homogeneously distributed over the adsorbent surface.

The linearized form of Langmuir isotherm equation can be written as

$$\frac{1}{q_e} = \frac{1}{q_m} + \frac{1}{q_m K_L} \cdot \frac{1}{C_e} \cdot \tag{4.11}$$

The values of q_m and K_L are calculated from the slope and intercept of the straight line of plot of $1/q_e$ versus $1/C_e$.

The Freundlich model is an empirical equation used to describe the surface heterogeneity of the sorbent. It assumes multilayer adsorption with a heterogeneous energetic distribution of active sites, accompanied by interactions between adsorbed molecules (Mahapatra et al. 2013). A linear form of the Freundlich isotherm can be expressed as

$$\ln q_e = \ln K_F + \frac{1}{n} \ln C_e \cdot \tag{4.12}$$

The slope $1/n$ of the logarithmic plots is a measure of the sorption intensity or surface heterogeneity. A value of $1/n$ smaller than unity indicates a normal Langmuir isotherm, while $1/n > 1$ is indicative of cooperative adsorption (Fytianos et al. 2000).

4.2.8 Adsorption Kinetics

Kinetic models are used to explore the rate of the adsorption process and potential rate-controlling step. In the present work, the experimental kinetic data have been analyzed by using pseudo-first-order, pseudo-second-order, and intraparticle diffusion models.

The Langergren pseudo-first-order rate equation can be expressed as (Lagergren 1898):

$$\frac{dq_t}{dt} = k_1(q_e - q_t) \tag{4.13}$$

where k_1 is the rate constant of pseudo-first-order sorption (h^{-1}). The integrated form of Eq. (4.13) becomes

$$\ln(1 - \frac{q_t}{q_e}) = -k_1 t. \tag{4.14}$$

A plot of $\ln(1 - \frac{q_t}{q_e})$ versus t should give a straight line with slope k_1, and if pseudo-first-order model is valid, this linear plot should pass through the origin (Uddin et al. 2009).

The pseudo-second-order sorption kinetics includes the whole sorption process, involving external diffusion, surface sorption, and internal diffusion (Cheng et al. 2017). The rate equation of pseudo-second-order kinetic model can be expressed as (Ho and McKay 1998):

$$\frac{dq_t}{dt} = k_2(q_e - q_t)^2 \tag{4.15}$$

where k_2 (g/mg h) is the rate constant of the pseudo-second order model. The integrated form of Eq. (4.15) becomes

$$\frac{t}{q_t} = \frac{1}{k_2 q_e^{\,2}} + \frac{1}{q_e} t. \tag{4.16}$$

If the second-order kinetic equation of Eq. (4.16) is valid, the plot of t/q_t against t should give a linear relationship. The q_e and k_2 can be calculated from the slope and intercept of the plot.

The intraparticle diffusion model can be expressed by the Weber and Morris equation (Weber and Morris 1963; Wei et al. 2017) as:

$$q_t = k_i t^{0.5} + C_i \tag{4.17}$$

where k_i (mg/g $h^{0.5}$) is the rate constant of the stage i that can be obtained from slop of the linear plot of q_t versus $t^{0.5}$; the C_i value can be estimated from the intercept of stage i, and represents a constant depicting resistance to mass transfer in the boundary layer. Usually the larger value of C_i, the thicker the boundary layer, and the greater boundary layer effect (Wei et al. 2017). The validity of this model can be verified by the linearity of the plot of q_t versus $t^{0.5}$. If intraparticle diffusion is solely the rate limiting step, the linear plot of q_t against $t^{0.5}$ passes through the origin. On the other hand, when more than one mechanism is involved in the sorption process, the linear line does not pass through the origin (Han et al. 2017; Nethajia et al. 2010).

4.3 Results and Discussions

4.3.1 Flexibility of Alumina-Silica/Iron Oxide NF Membranes

The optical images presented in Figs. 4.2(a)–(c) show the flexibility of the alumina-silica/iron oxide NF membranes. Upon bending no crack was found in any of the three membranes of CS-1, CS-2 and CS-3 with different feed rate of sheath layer, indicating their flexible and self-standing nature. However, the iron oxide NF membrane prepared separately was very fragile and could not be freestanding. Therefore, the amorphous alumina-silica core may facilitate the stress during bending and retains the integrity of the membrane.

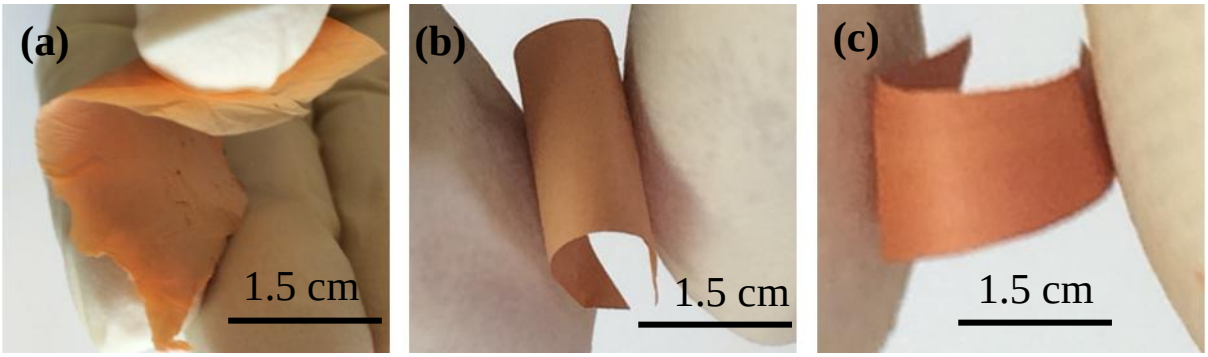

Fig. 4.2 Optical images of self-standing and flexible alumina-silica/iron oxide NF membranes after bending: (a) CS-1, (b) CS-2 and (c) CS-3.

4.3.2 Morphology of Core and Core-Sheath NFs

Figs. 4.3(a) and (b) show the SEM images of the alumina-silica core NF membrane and individual core NF, respectively, whereas Fig. 4.3(c) shows the TEM image of the alumina-silica core NF. It is apparent from Figs. 4.3(a)–(c) that the alumina-silica core NF with average ~125 nm diameter exhibits smooth surface of which roughness $\lesssim$ 1 nm. The morphology and composition of alumina-silica/iron oxide core-sheath NFs were investigated by SEM, TEM and EDX analysis, and the results were presented in Fig.4.4 to Fig. 4.10. The elemental compositions of CS-1, CS-2 and CS-3 membranes obtained from EDX analysis are presented in Table 4.2. As shown in Table 4.2, the atomic ratio of Fe:(Al + Si) in the CS-1, CS-2 and CS-3 membranes were 0.76, 1.07 and 1.42, respectively. From the SEM images of NF membranes shown in Fig. 4.4(a), Fig. 4.6(a) and Fig. 4.8(a), it is apparent that the NFs in

the membranes are randomly oriented forming nonwoven structures.

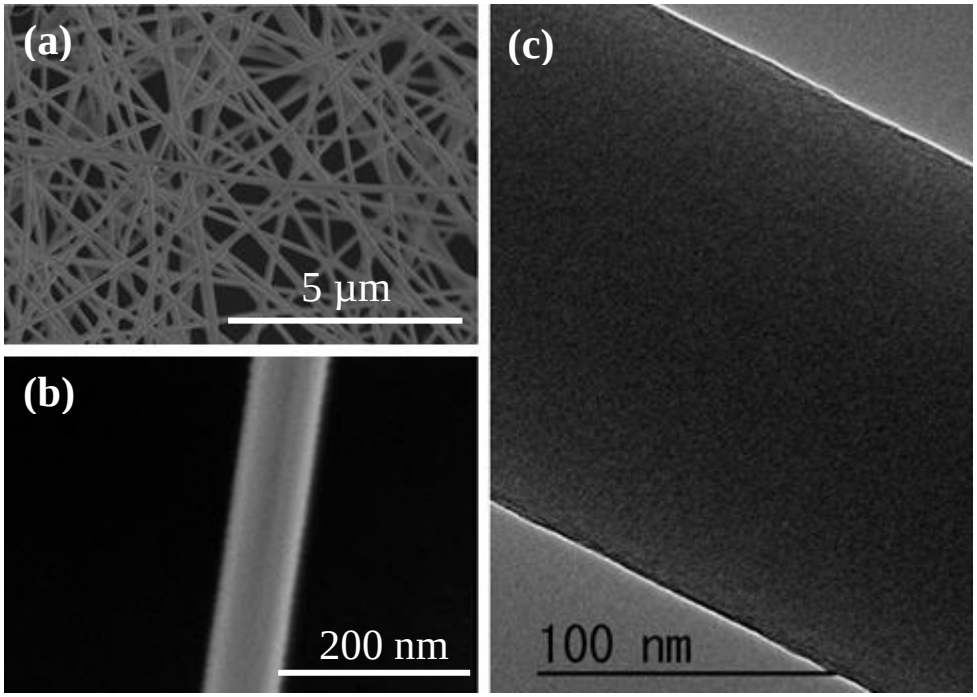

Fig. 4.3 Images of alumina-silica core NFs without sheath layer: SEM image of NF membrane (a), SEM image of a NF (b), and TEM image of a NF (c).

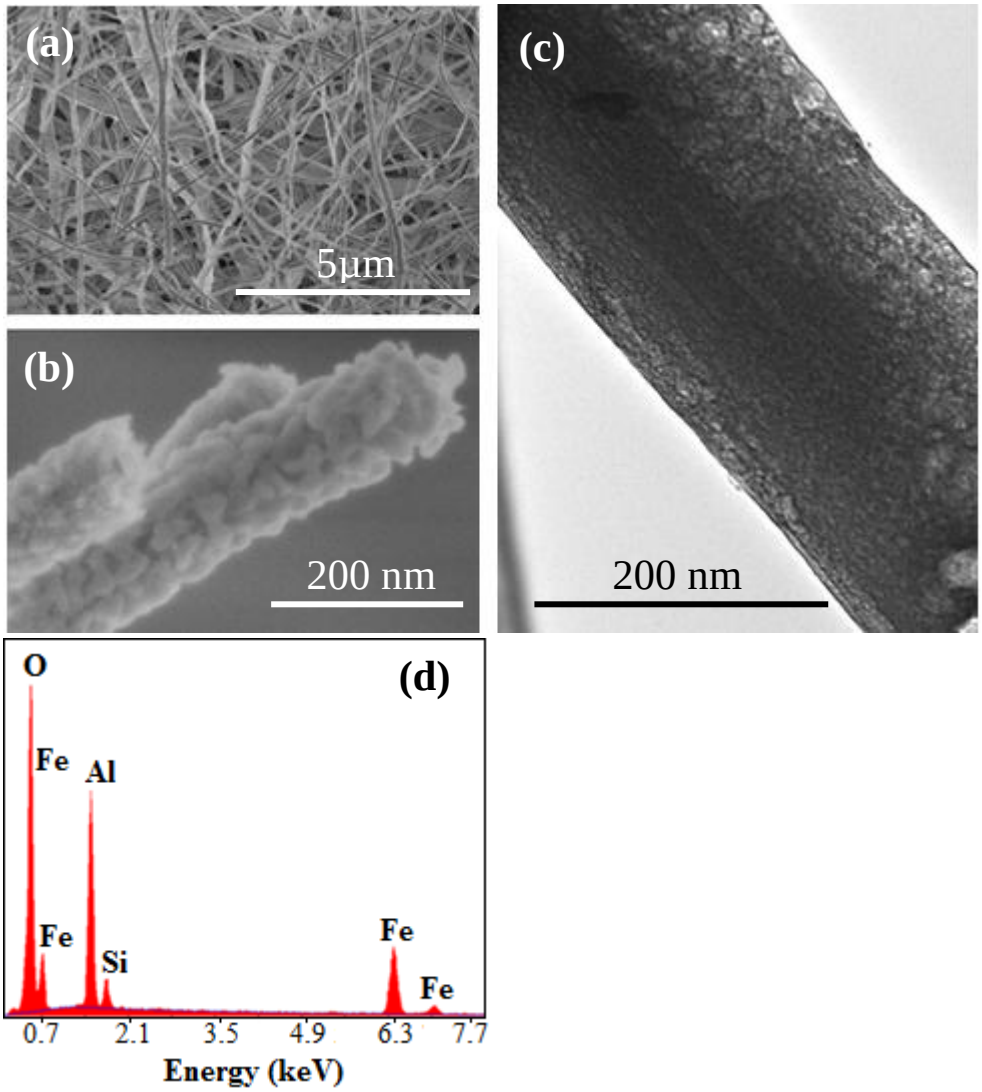

Fig. 4.4 Images of alumina-silica/iron oxide core-sheath NFs (CS-1): SEM image of NF membrane (a), SEM image of NFs (b), and TEM image of a NF (c); EDX spectrum of CS-1 membrane (d).

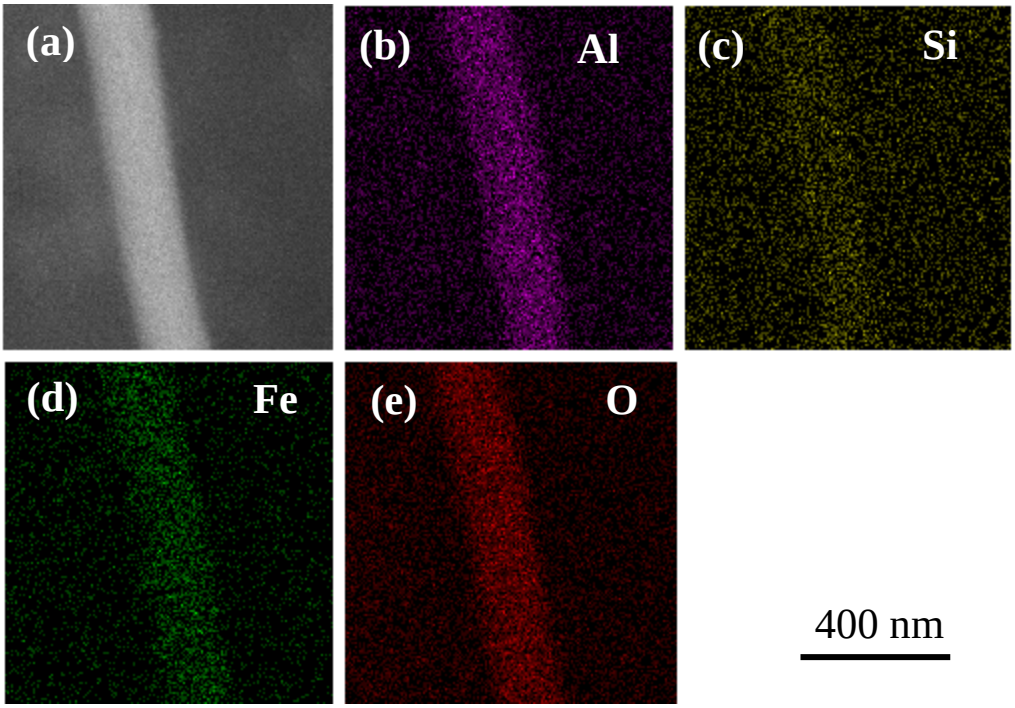

Fig. 4.5 SEM image of CS-1 NF (a), and the corresponding EDX elemental mapping of Al (b), Si (c), Fe (d) and O (e).

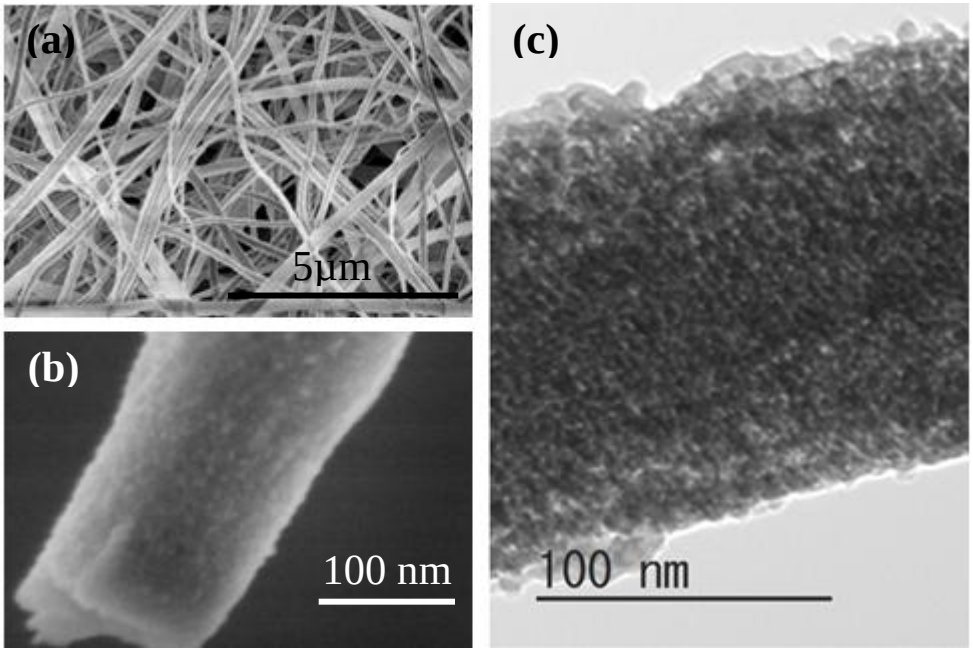

Fig. 4.6 Images of alumina-silica/iron oxide core-sheath NFs (CS-2): SEM image of NF membrane (a), SEM image of a NF (b), TEM image of a NF (c).

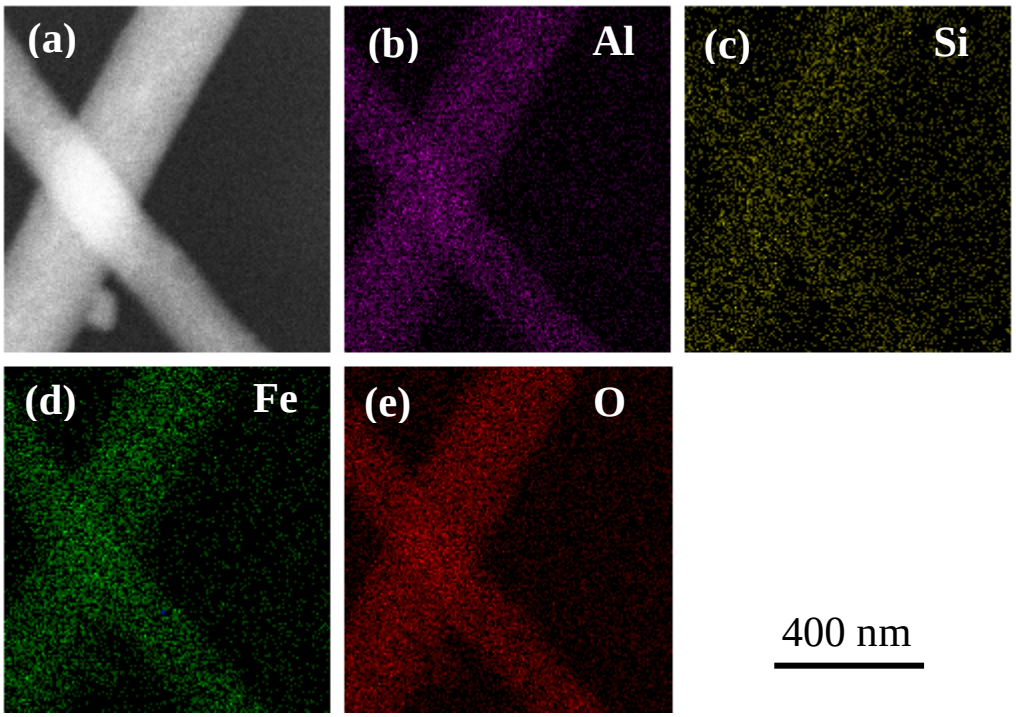

Fig. 4.7 SEM image of CS-2 NF (a), and the corresponding EDX elemental mapping of Al (b), Si (c), Fe (d) and O (e).

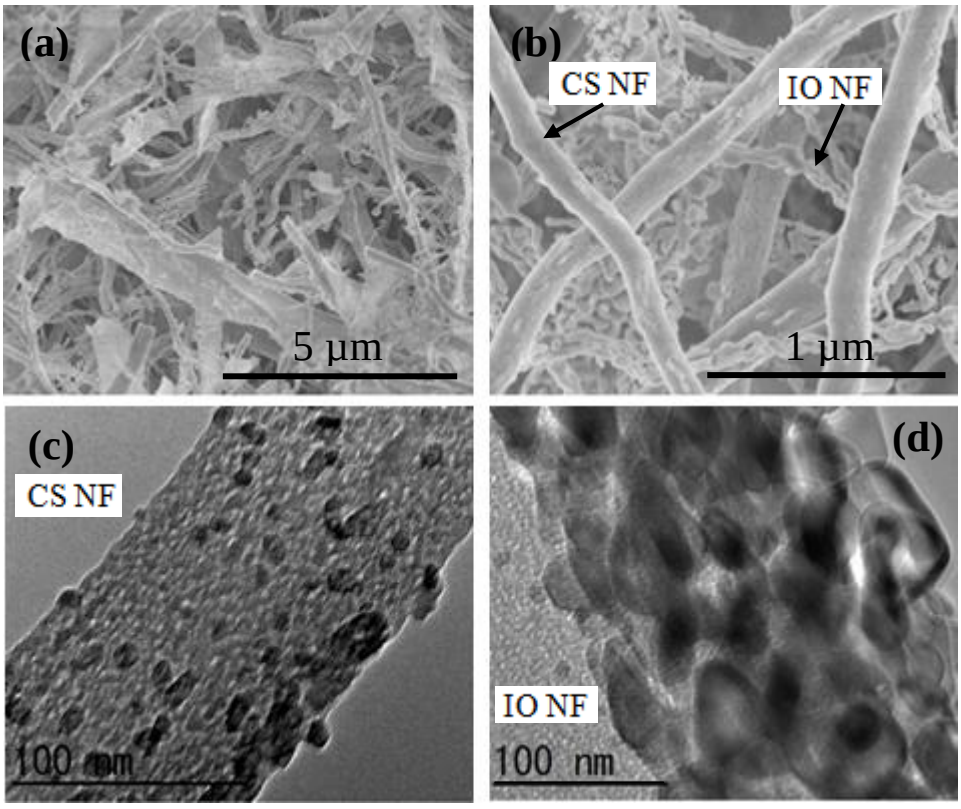

Fig. 4.8 SEM images of CS-3 NF membrane (a) and (b); TEM images of core-sheath (CS) NF (c) and iron oxide (IO) NF (d) observed in CS-3 membrane.

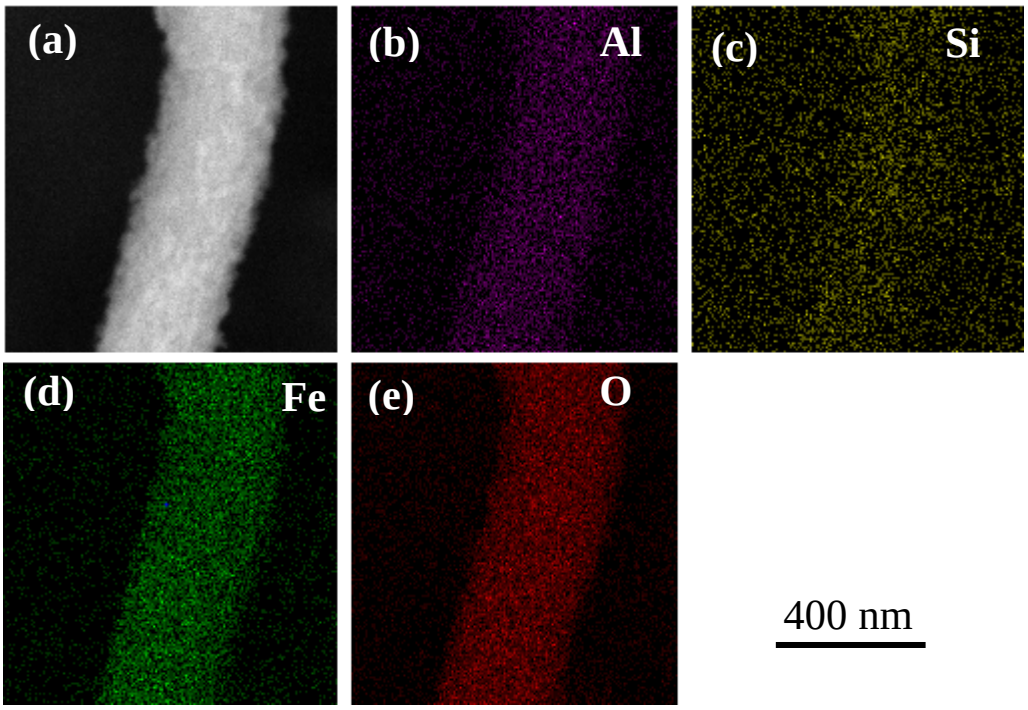

Fig. 4.9 SEM image of Core-sheath (CS) NF observed in CS-3 membrane (a), and the corresponding EDX elemental mapping of Al (b), Si (c), Fe (d) and O (e).

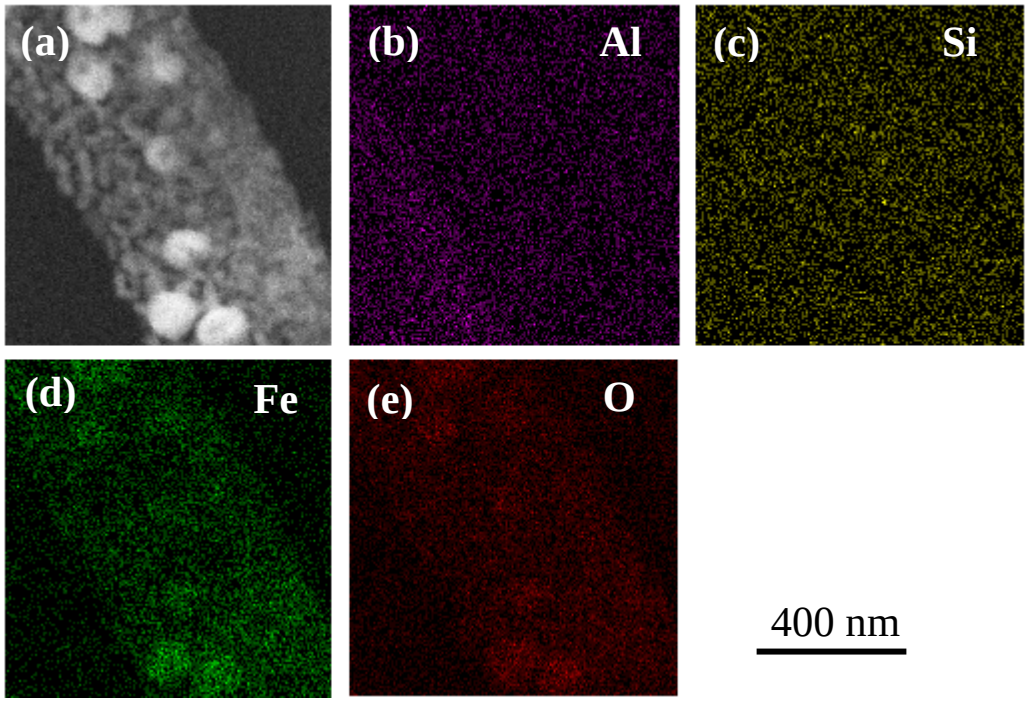

Fig. 4.10 SEM image of Iron oxide (IO) NF observed in CS-3 membrane (a), and the corresponding EDX elemental mapping of Al (b), Si (c), Fe (d) and O (e).

Table 4.2 Elemental compositions of CS-1, CS-2 and CS-3 membranes obtained from EDX analysis

At%	CS-1	CS-2	CS-3
O	55.39	54.12	53.61
Al	22.24	19.48	16.87
Si	3.06	2.68	2.31
Fe	19.31	23.72	27.22
Total	100	100	100
Fe/(Al + Si)	0.76	1.07	1.42

The TEM images in Fig. 4.4(c), Fig. 4.6(c) and Fig. 4.8(c) apparently showed that the surface morphology of core-sheath NFs were different from that of simple alumina-silica core NF (Fig. 4.3(c)). In contrast to the smooth surface on alumina-silica core NF, the rough surfaces with a large number of particles indicate the formation of iron oxide crystallites on the surface of core NFs

In the case of CS-1, it can be clearly observed from the SEM (Fig. 4.4(b)) and TEM (Fig. 4.4(c)) that the NF was composed of a thin and porous sheath layer of iron oxide covering the alumina-silica core surface. In case of CS-2 NF, small iron oxide nanoparticles were densely arranged to form a thick and porous sheath layer as shown in the SEM (Fig. 4.6 (b)) and the TEM (Fig. 4.6 (c)) images.

In the case of CS-3, the whole surface of NF's core was covered with iron oxide sheath layer as observed from TEM (Fig. 4.8 (c)) and EDX mapping (Fig. 4.9) images. However, the CS-3 membrane in Figs. 4.8(a) and (b) consisted of two types of NFs, of core-sheath (CS) and iron oxide (IO) differently from CS-1 and CS-2. This was confirmed by the TEM images (Figs. 4.8 (c) and (d)) and EDX mapping images (Fig. 4.9 and Fig. 4.10). The IO NF of CS-3 membrane was mainly formed by relatively larger iron oxide particles as shown in TEM (Fig. 4.8 (d)) and EDX mapping (Fig. 4.10) images.

4.3.3 XRD Analysis

XRD was used to investigate the phase structure of alumina-silica/iron oxide NF membranes. Figs. 4.11 (a), (b) and (c) respectively show the XRD spectra of the three membranes (CS-1,

CS-2 and CS-3) calcined at 600 °C. All the diffraction peaks observed for CS-1, CS-2 and CS-3 can readily be assigned to rhombohedral phase α-Fe_2O_3 (hematite) (Joya et al. 2013; Morris et al. 1981). An additional peak found for CS-3 at 2θ ~ 33.03° can be indexed to (220) of Fe_3O_4 (magnetite). The values of the interplanar spacing and lattice parameter matched well with the standard data. No diffraction peak was found for the alumina-silica because at the temperature 600 °C, alumina-silica exists as amorphous phase (Mukhlish et al. 2017).

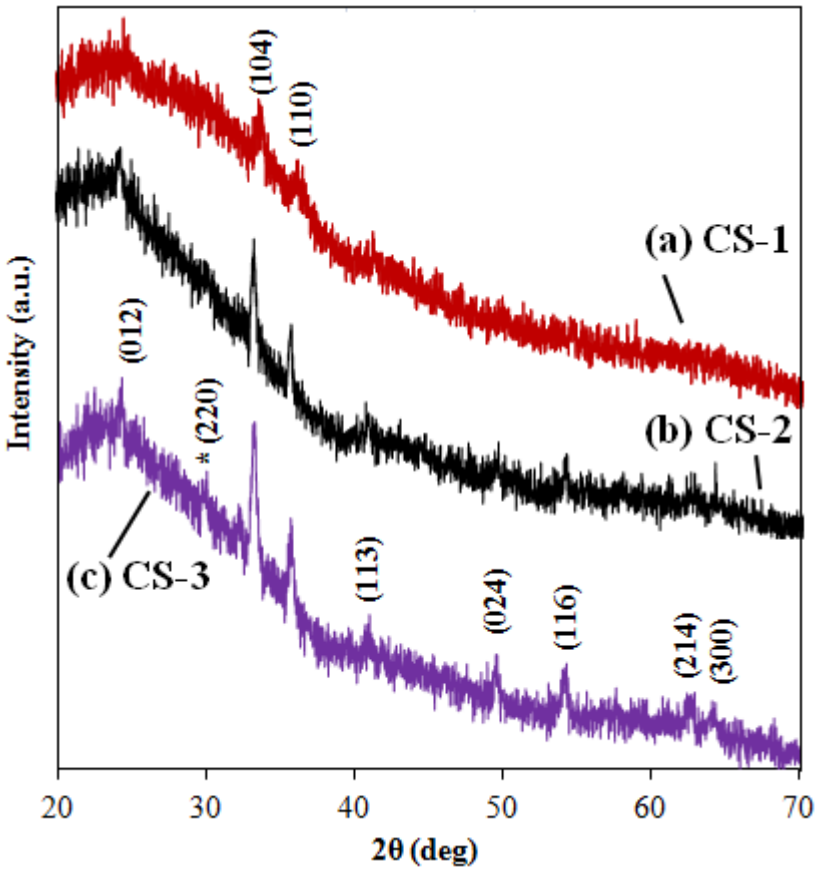

Fig. 4.11 XRD spectra of the alumina-silica/iron oxide NF membranes calcined at 600 °C: (a) CS-1, (b) CS-2 and (c) CS-3.

4.3.4 Effect of pH for Adsorption of RR-120 onto CS-1 NF Membrane

The surface charge of the alumina-silica/iron oxide NF membrane (CS-1) as a function of solution pH is shown in Fig. 4.12. As observed from Fig. 4.12, the surface charge of the membrane was zero at pH 5.85. Therefore, the pH_{pzc} of alumina-silica/iron oxide nanofibrous membrane (CS-1) is 5.85. In aqueous solution at pH < pH_{pzc}, the NF surface was charged

positively due to protonation of aluminum hydroxide or iron hydroxide according to the following reactions:

$$M\text{-}OH + H^{+} \leftrightarrow M\text{-}OH_2^{+}\,(positive\,surface),\ \text{where}\ M = Al\ \text{or}\ Fe, \tag{4.18}$$

whereas at pH > pH_{pzc}, the NF surface is negatively charged as a result of deprotonation of M-OH:

$$M\text{-}OH + OH^{-} \leftrightarrow M\text{-}O^{-}\,(negative\ surface) + H_2O. \tag{4.19}$$

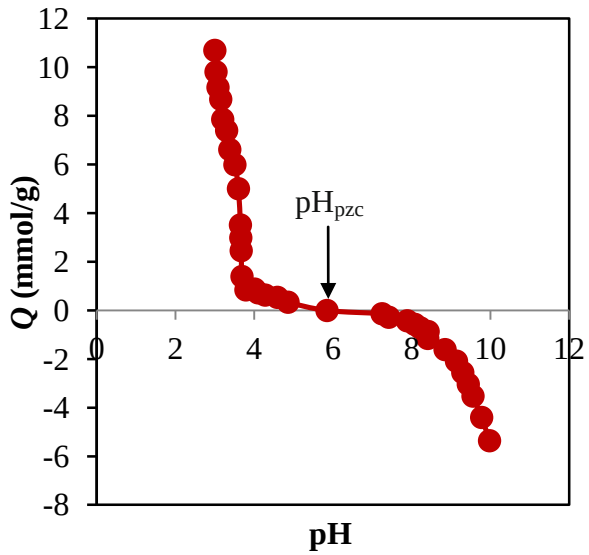

Fig. 4.12 Surface charge *Q* of CS-1 NF membrane as a function of pH.

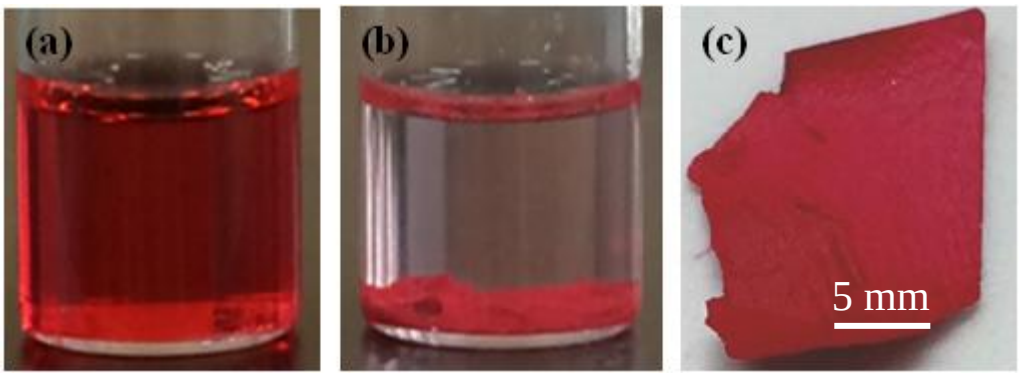

Fig. 4.13 Optical images taken (a) before and (b) after RR-120 dye adsorption on CS-1 membrane, where the membrane has been immersed in dye solution, and (c) dye-adsorbed NF membrane.

The optical images of RR-120 dye solution (C_o = 100 mg/L, pH 3) before and after the adsorption with CS-1 membrane are shown in Figs. 4.13(a) and (b), respectively. The colored water of C_o = 100 mg/L (Fig. 4.13(a)) became almost colorless and transparent (C_e = 5.70 mg/L) after adsorption as a result of dye uptake by the CS-1 membrane as shown in 4.13 (b). The dye-loaded membrane could be easily separated from the liquid phase due to its self-standing nature compared to the conventional powdery form. Moreover, the color of the dye-adsorbed NF membrane shown in Fig. 4.13(c) apparently reveals the excellent sorption affinity of the membrane towards RR-120 dye.

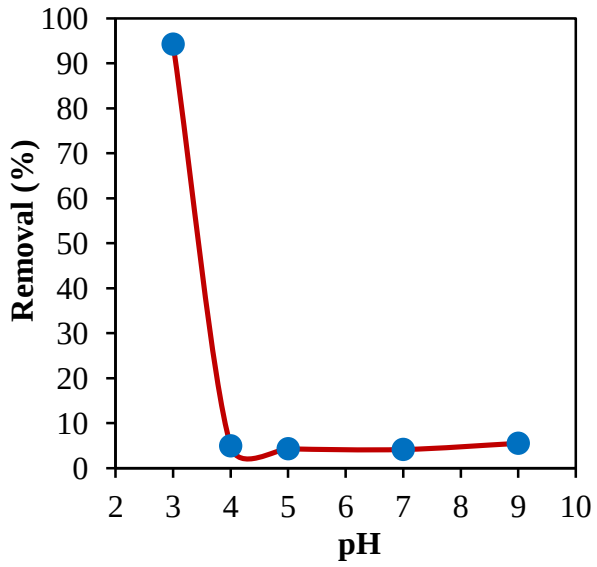

Fig. 4.14 Effect of initial pH of dye solution on the removal percentage of RR-120 onto alumina-silica/iron oxide NF membrane (CS-1).

The influence of initial pH of dye solution on the adsorption of RR-120 by alumina-silica/iron oxide membrane (CS-1) is shown in Fig. 4.14. As observed from Fig. 4.14, the dye removal performance of the membrane was highly influenced by the pH of initial dye solution. At pH 3, maximum dye removal (~94%) was achieved. The dye removal dropped rapidly to ~5% with the increase of initial dye solution pH (4–9). The adsorption, however, remained almost constant within the range of pH 4–9. The high adsorption performance at pH 3 may be due to high positive charge density on the adsorbent surface (Fig. 4.12) which bind negatively charged dye molecules through electrostatic attraction between M-OH_2^+ of adsorbent and R-SO_3^- of dye.

The adsorption was not favorable at higher pH (4–9) due to poor attraction or even

repulsion between adsorbent surface and dye anion, because adsorbent surface existed in either poorly positively charged (at pH 4–5.85) or even negatively charged (at pH 5.85–9) as shown in Fig. 4.12. About 5% dye removal observed at pH 4–9 may arise from physical adsorption resulting from van der Waals attraction, hydrogen bonding and inter-fibers porous structure of the NF membrane (Patel and Hota 2016; Tabak et al. 2010).

4.3.5 Effect of Adsorbent (CS-1 Membrane) Dosage

Fig. 4.15 shows the effect of adsorbent (CS-1) dosage on the removal of RR-120. As shown in Fig. 4.15, the percent of dye removal increased with increasing the adsorbent dosage, which might be due to the increased number of active sites at greater dosages of adsorbent. Fig. 4.15 also shows that the equilibrium adsorption density q_e increased initially with the increase in adsorbent dosage up to a certain limit. For instance, the q_e value increased from 516.59 mg/g to 667.98 mg/g with the increase in adsorbent mass from 0.0008 g to 0.0028 g. On further increase in adsorbent dosage, the q_e value decreased. Similar adsorption trend was reported by Celekli et al. (2012) and Khan et al. (2014). The highest q_e value was obtained for adsorbent mass of 0.0028 g, and this dosage was selected for further adsorption studies.

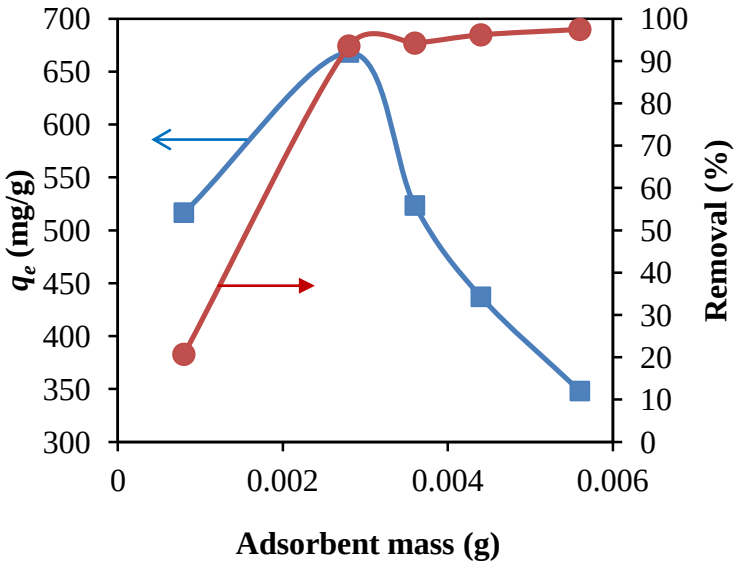

Fig. 4.15 Effect of adsorbent dosage on the adsorption density at equilibrium q_e and removal percentage of RR-120 by alumina-silica/iron oxide NFs (CS-1).

4.3.6 Adsorption Thermodynamics

Fig. 4.16 shows the linear plot of lnK_d versus 1/T with correlation coefficient value of R^2 = 0.9981. The values of ΔH^o and ΔS^o were calculated from the slope and the intercept of the straight line, respectively, whereas the ΔG^o value was calculated from Eq. (4.6). The thermodynamic parameters are summarized in Table 4.3.

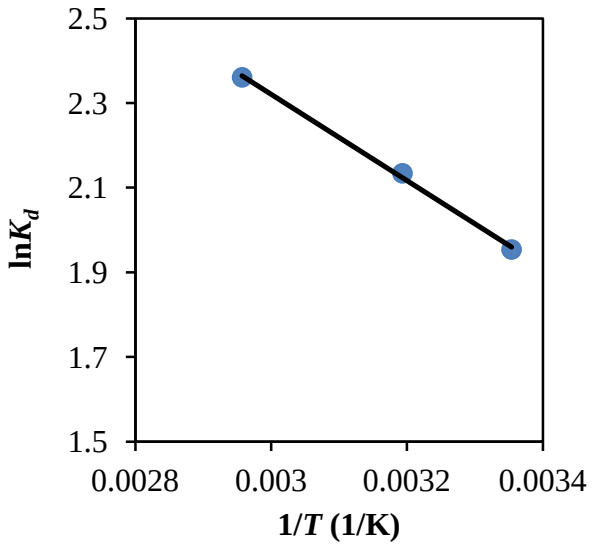

Fig. 4.16 Plot of lnK_d versus 1/T for the adsorption of RR-120 onto alumina-silica/iron oxide NF membrane (CS-1).

Table 4.3 Thermodynamic parameters for the adsorption of RR-120 onto alumina-silica/iron oxide NF membrane (CS-1) at different temperatures

T (K)	ΔG^o (kJ/mol)	ΔH^o (kJ/mol)	ΔS^o (J/(mol K))
298.15	–4.84	8.48	44.75
313.15	–5.55		
338.15	–6.63		

As shown in Table 4.3, the negative values of ΔG^o imply the feasibility of the process and spontaneous nature of adsorption. Further, the positive value of ΔH^o shows the adsorption to be endothermic (Hameed et al. 2009). The positive value of ΔS^o indicates that the adsorption process goes to a state of higher disorder, possibly due to the redistribution of energy between

the adsorbent and adsorbate during the adsorption process. In addition, both positive values for ΔH^o and ΔS^o imply that the adsorption of the system is spontaneous at normal and high temperatures (Agcaoili et al. 2017). Similar results were reported for the adsorption of RR-120 on activated oil palm ash (Hameed et al. 2009) and on ionic liquid modified iron oxide nanoparticles (Absalan et al. 2011).

4.3.7 Adsorption Isotherms

The experimental equilibrium data for RR-120 dye adsorption onto three alumina-silica/iron oxide NF membranes (CS-1, CS-2 and CS-3) were fitted to Langmuir Eq. (4.11) and Freundlich Eq. (4.12) isotherm models. The fitted Langmuir and Freuindlich curves are shown in Figs. 4.17 and 4.18, respectively. The isotherm parameters as well as correlation coefficients (R^2) are shown in Table 4.4. Based on R^2 values, the sorption equilibrium data were better fitted by Langmuir isotherm model than Freundlich isotherm model. As estimated from the Langmuir model, the maximum dye sorption capacity q_m for CS-1, CS-2 and CS-3 are 1478.85, 1860.81 and 851.28 mg/g, respectively. However, the degree of favor of the adsorption system is estimated through R_L (Weber and Chakkravorti 1974), which is a dimensionless equilibrium parameter known as separation factor:

$$R_L = \frac{1}{(1 + K_L C_o)} \tag{4.20}$$

where K_L (L/mg) is the Langmuir constant and C_o (mg/L) is the initial concentration of dye solution. The value of R_L predicts the adsorption process to be either irreversible (R_L = 0), favorable (0 < R_L < 1), linear (R_L = 1) or unfavorable (R_L > 1). The calculated R_L values for different initial RR-120 concentrations were found to be in the range of 0.065–0.017, 0.070–018, 0.25–0.17 for CS-1, CS-2 and CS-3, respectively. This shows that the adsorption process was favorable under the experimental conditions in the present study.

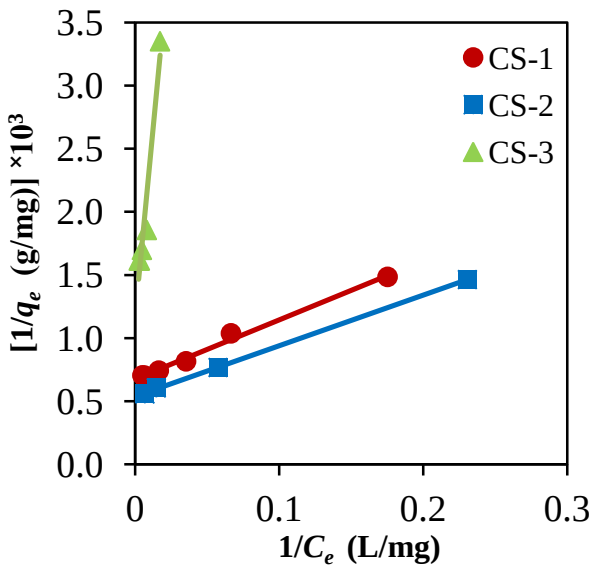

Fig. 4.17 Plots using Eq. (4.11) of Langmuir isotherm for the adsorption of RR-120 by alumna-silica/iron oxide NF membranes (CS-1, CS-2 and CS-3).

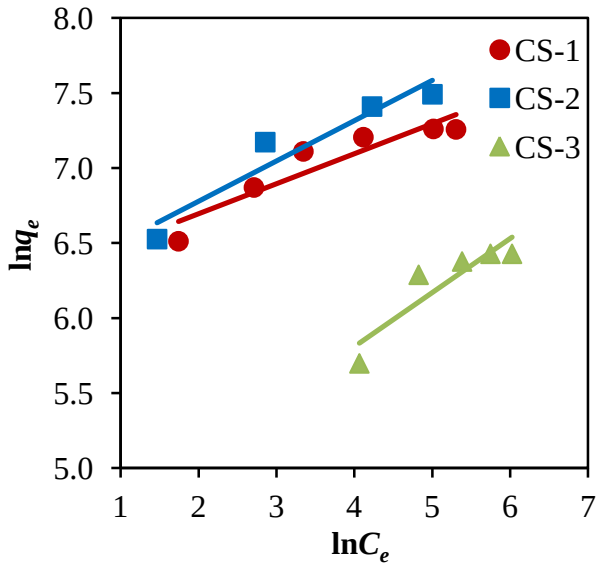

Fig. 4.18 Plots using Eq. (4.12) of Freundlich isotherm for the adsorption of RR-120 by alumna-silica/iron oxide NF membranes (CS-1, CS-2 and CS-3).

Table 4.4 Langmuir and Freudlich isotherm parameters and correlation coefficients for the adsorption of RR-120 by alumina-silica/iron oxide NF membranes (CS-1, CS-2 and CS-3)

	Langmuir isotherm			Freundlich isotherm		
Sample	q_m (mg/g)	K_L (L/mg)	R^2	K_F (mg/g)/(mg/L)$^{1/n}$	$1/n$	R^2
CS-1	1478.85	0.1442	0.9926	541.7475	0.2003	0.8655
CS-2	1860.81	0.1338	0.9998	513.3716	0.2686	0.9152
CS-3	851.28	0.00975	0.9469	78.6966	0.3607	0.8231

The monolayer adsorption capacity of several adsorbents for RR-120 dye uptake from aqueous solution is summarized in Table 4.5, which clearly reveals that the alumina-silica/iron oxide NF membrane is an excellent adsorbent for the removal of RR-120 dye. As shown in Table 4.5, the q_m of 1860.81 mg/g for CS-2 is the highest among adsorbents ever reported in the literature.

Table 4.5 Comparison of different adsorbents in the adsorption of textile dye RR-120. Maximum adsorption capacity was calculated with the Langmuir model

Adsorbent	Maximum adsorption capacity q_m (mg/g)	References
Chara contraria (alga) powder	112.83	(Celekli et al. 2012)
Lentinus sajor-caju (fungus) biomass	117.8	(Arica and Bayramoglu 2007)
Pistachio husk	324.88	(Celekli et al. 2010)
Activated oil palm ash	200.12	(Hameed et al. 2009)
Metal hydroxide sludge	48.31	(Netpradit et al. 2003)
Clay	29.94	(Errais et al. 2011)
Fe_3O_4 nanoparticles	166.67	(Absalan et al. 2011)
Single-walled carbon nanotubes	426.49	(Bazrafshan et al. 2013)
Activated carbon powder	400	(Kharaisheh et al. 2002)
Alumina-silica NFs	884.95	(Mukhlish et al. 2017)
Alumina-silica/iron oxide NFs (CS-2)	1860.81	Present work

4.3.8 Adsorption Kinetics

Fig. 4.19 shows the effect of contact time *t* on the adsorption of dye onto CS-1, CS-2, CS-3 and Core membranes. As shown in Fig. 4.19, the membranes continued to adsorb dye for a long time and finally reached to saturation stage. Similar behavior was observed for adsorption of leachate materials on activated carbon (Zamora-Villafranco et al. 2014). The slow mass transfer of dye molecules can be linked to porous and dense NFs network in the membranes.

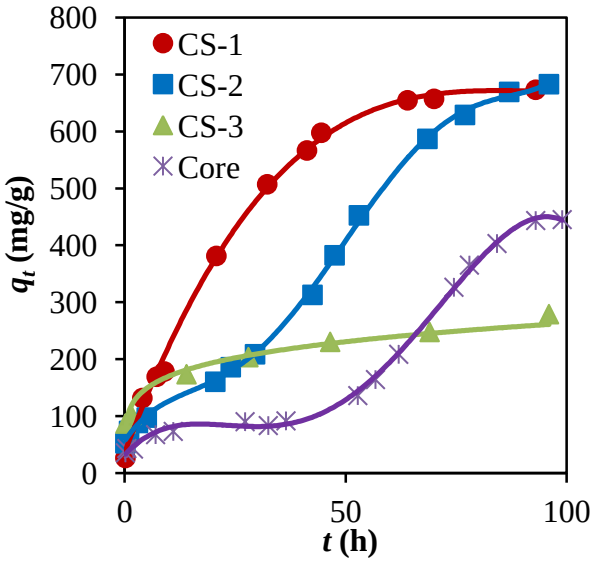

Fig. 4.19 Effect of contact time *t* on the adsorption density q_t for RR-120 (C_o = 100 mg/L) sorption onto alumina-silica/iron oxide core-sheath NF membranes (CS-1, CS-2 and CS-3) and alumina-silica NF membrane (Core).

Based on the observations reported in the literature (Badruzzaman et al. 2004; Nethajia et al. 2010; Li et al. 2016), it can be proposed that the dynamics of adsorption on nanofibrous adsorbent may follow four consecutive steps: (i) diffusion of dye molecules through bulk liquid to the boundary layer film (a film of solvent) surrounding the adsorbent (bulk diffusion); (ii) transport of dye molecules through the boundary layer to the exterior surface of the NF membrane (film or boundary layer diffusion); (iii) intraparticle diffusion of dye molecules within the pores of the nanofibers network as well as the inner pores of the NFs, (iv) adsorption of dye molecules on the interior solid surfaces of the membrane. In the second step, small amount of dye can also be adsorbed on the external surface of the membrane. Dye molecules can reach to an adsorption site in the pores of adsorbent either by

a diffusion process through the liquid-filled pores or by a solid-surface diffusion mechanism (Cheunga et al. 2007). Generally, the bulk diffusion and adsorption steps are rapid and consequently not rate-limiting. Film diffusion and intraparticle diffusion are the key factors that control the rate of adsorption of an adsorbate from the solution by a porous adsorbent, and these two adsorption mechanisms work in series. The slower one in the two processes will be a rate-limiting step (Kumar et al. 2008).

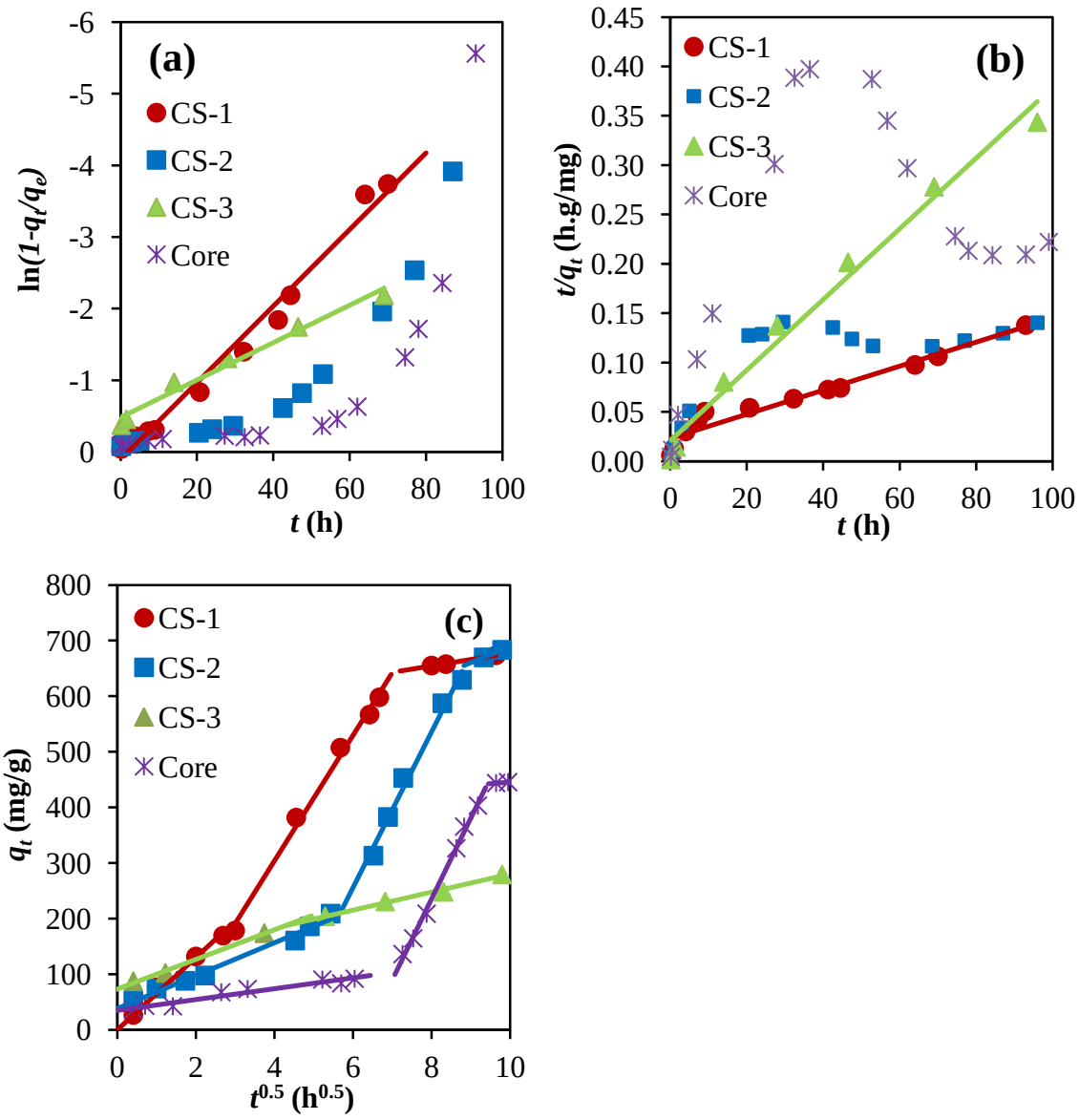

Fig. 4.20 Plots for models of pseudo-first-order (a), pseudo-second-order (b), and intraparticle diffusion (c) with C_o = 100 mg/L for the adsorption of RR-120 by NF membranes (CS-1, CS-2, CS-3 and Core) using Eqs.(4.14), (4.16), and (4.17), respectively.

Table 4.6 Kinetic constants of RR-120 adsorption by CS-1, CS-2, CS-3 and Core for pseudo-first-order and pseudo-second-order models. For CS-2 and Core, the plots did not fit to the models

	$q_{e,\,exp}$ (mg/g)	Pseudo-first-order model			Pseudo-second-order model		
		$q_{e,\,calc}$ (mg/g)	k_1 (h^{-1})	R^2	$q_{e,\,calc}$ (mg/g)	k_2 (g/mg h)	R^2
CS-1	673.51	747.39	0.0535	0.9838	833.33	0.000062	0.9467
CS-2	683.31	–	–	–	–	–	–
CS-3	279.36	172.708	0.0261	0.9793	277.78	0.000629	0.9841
Core	445.45	–	–	–	–	–	–

Table 4.7 Kinetic constants of RR-120 adsorption by CS-1, CS-2, CS-3 and Core for intraparticle diffusion model. The k_a, k_b and k_c are intraparticle diffusion rate constants for the first, second, and third stage of the intraparticle diffusion plot, respectively, whereas the C_a, C_b and C_c are intercept of first, second, and third stage, respectively

Intraparticle diffusion plot	Model constants	CS-1	CS-2	CS-3	Core
First stage	k_a (mg/g $h^{0.5}$)	65.03	29.61	26.54	9.75
	C_a (mg/g)	0	38.42	73.59	35.03
	R^2	0.9858	0.9847	0.9948	0.9418
Second stage	k_b (mg/g $h^{0.5}$)	112.96	140.11	16.26	145.19
	C_b (mg/g)	–148.29	–584.57	117.67	–925.82
	R^2	0.9937	0.9868	0.9894	0.9962
Third stage	k_c (mg/g $h^{0.5}$)	11.57	28.88	–	5.57
	C_c (mg/g)	561.68	400.35	–	389.99
	R^2	0.9923	1	–	1
	$q_{e,\,exp}$ (mg/g)	673.51	683.31	279.36	445.45
	$q_{e,\,calc}$ (mg/g)	673.29	683.31	276.97	445.44

The experimental kinetic data for adsorption of RR-120 (C_o = 100 mg/L) onto alumina-silica/iron oxide NF membranes (CS-1, CS-2 and CS-3) and alumina-silica NF membrane (Core) were treated with pseudo-first-order Eq. (4.14), pseudo-second-order Eq. (4.16) and intraparticle diffusion Eq. (4.17), and the corresponding kinetic plots were presented in Figs. 4.20(a), (b) and (c), respectively. From the fitted values of pseudo-first-order and pseudo-second-order model parameters, the calculated equilibrium adsorption

capacity ($q_{e,\ calc}$) was evaluated. For intraparticle diffusion model, $q_{e,\ calc}$ was estimated using the model parameters obtained for the last linear section of fitted plot. The model parameters, R^2 values, experimental q_e values ($q_{e,\ exp}$) as well as q_e values for pseudo-first-order and pseudo-second-order models are shown in Table 4.6 and those for intraparticle diffusion model are presented in Table 4.7.

As shown in Fig. 4.20(a), the plots using the pseudo-first-order model were not on a straight line for CS-2 and Core, and the lines obtained for CS-1 and CS-3 did not pass through the origin for any of adsorbent samples. Moreover, the values of $q_{e,\ calc}$ did not agree with those of $q_{e,\ exp}$ (Table 4.6). Therefore, it was apparent that the adsorption of dye on CS-1, CS-2, CS-3 and Core did not follow the first order kinetic model. Furthermore, it was apparent from Fig. 4.20(b) that the pseudo-second-order model did not fit well for CS-2 and Core. In addition, the $q_{e,\ calc}$ was different from the experimental q_e value ($q_{e,\ exp}$) for CS-1 (Table 4.6). For CS-3, the pseudo-second-order model fitted the kinetic data well and $q_{e,\ calc}$ was much closer to $q_{e,\ exp}$ (Table 4.6), which suggested that the sorption process passed through multiple stages involving transport of the adsorbate from the aqueous phase to the adsorbent surface and diffusion of the adsorbate into the interior of the adsorbent pores (Ramachandran et al. 2011). However, the R^2 value of pseudo-second-order model for CS-3 was lower than that of the intraparticle diffusion model mentioned below.

As shown in Fig. 4.20(c) and Table 4.7, for all the four samples, the intraparticle diffusion model fitted well with good R^2 values, and the $q_{e,\ calc}$ values were also close to the experimental $q_{e,\ exp}$ values, while the plots q_t *vs.* $t^{0.5}$ exhibited two (for CS-3) or three (for CS-1, CS-2 and Core) linear sections with different slope. The intraparticle diffusion rate constants for the three sections are denoted by k_a, k_b and k_c. The first linear section is due to the film diffusion with k_a, where dye molecules travel towards the external surface of the adsorbent. The second liner region represents the intraparticle diffusion of dye molecules into the membrane and NFs with k_b. The third portion with smaller slope and k_c represents the equilibrium stage where intraparticle diffusion starts to slowdown may be due to extremely low dye concentrations in the solution (Wei et al. 2017; Li et al. 2016).

It is apparent from Fig. 4.20(c) that the linear line in the first stage of CS-1 passed through the origin but those in the second and third stages did not pass through the origin. This deviation from the origin might be due to the difference in the mass transfer rate in different stages of adsorption. It implies that the film diffusion may be a part of the rate determining step besides the intraparticle diffusion in the adsorption process for CS-1 (Tan et al. 2009; Cheunga et al. 2007). For CS-2, CS-3 and Core, the intraparticle diffusion plots did

not pass through the origin suggesting that both film diffusion and intraparticle diffusion were the rate-limiting steps in dye sorption on the membranes. It is noteworthy that the multiple-linearity does not indicate that the film diffusion and intraparticle diffusion happened separately, but shows that a predominant process exists in a certain period (Li et al. 2016). Similar multi-linear pattern of intra-particle diffusion plot can be found in many cases (Wei et al. 2017; Han et al. 2017; Li et al. 2016; Haitham et al. 2014). As shown in Table 4.7, the rate constants of second stage (k_b) for CS-1, CS-2 and Core were much higher than those in the first stage (k_a), indicating that the intraparticle diffusion in the second stage was faster compared to the film diffusion in the first stage. On the other hand, k_a was larger than k_b for CS-3, implying that film diffusion in the first zone was faster compared to the intraparticle diffusion in the second stage. In the third region, the rate constants (k_c) were found to be the lowest among the three stages for CS-1, CS-2 and Core.

4.3.9 Recovery of Dye and Reusability of Adsorbent

Desorption experiments were carried out to explore the possibility of dye recovery from dye-adsorbed NF membranes of CS-1, CS-2 and CS-3. Adsorption test was first conducted with 2.8 mg membrane and 20 mL dye solution (C_o = 100 mg/L, pH = 3) for 100 h. After the adsorption, the dye-adsorbed NF membrane was separated from the adsorption system and further immersed in 20 mL distilled water preadjusted to pH 10 for the desorption of dye. The amount of dye desorbed was achieved from the measurement of dye concentration in the solution. The recovery ratio was calculated using the following equation:

$$\text{Recovery ratio} = \frac{\text{Amount of dye desorbed}}{\text{Amount of dye adsorbed}} \tag{4.21}$$

The calculated recovery ratios were 0.904, 0.898 and 0.739 for CS-1, CS-2 and CS-3, respectively. At high pH, desorption of anionic dye occurs due to the electrostatic repulsion between dye anion and hydroxyl ion.

In order to study the potential reuse of the membrane, the NF membrane obtained after the desorption was regenerated by washing with distilled water followed by calcination in air at 540 °C for 3h. Then the adsorption test was repeated using the same dye solution with pH 3. Fig. 4.21 represents the equilibrium adsorption capacity (q_e) in the first and the second adsorption cycle using fresh and regenerated NF membranes, respectively. The

regenerated core-sheath NF membranes of CS-1 and CS-2 exhibited good adsorption property with the equilibrium adsorption capacity q_e larger than 600 mg/g. Therefore, the alumina-silica/iron oxide NF membranes are fit for practical application due to their regeneration and recyclable properties.

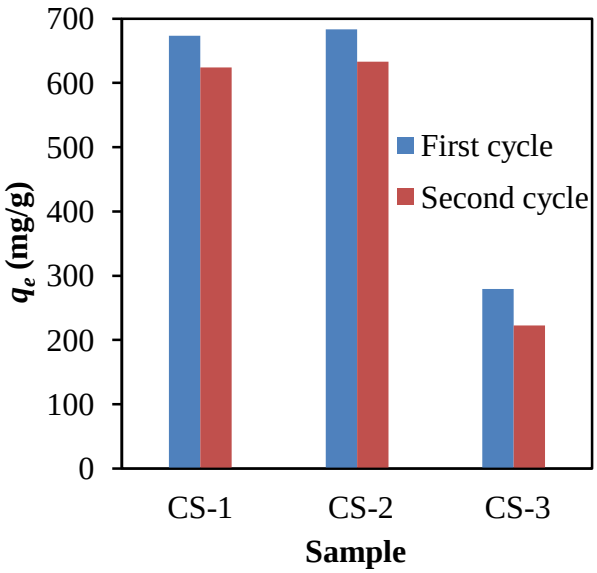

Fig. 4.21 Equilibrium adsorption capacity q_e for RR-120 dye adsorption using fresh (first cycle) and regenerated (second cycle) membranes of CS-1, CS-2 and CS-3.

4.4 Conclusions

We have successfully prepared self-standing nonwoven membranes of CS-1, CS-2 and CS-3 of alumina-silica/iron oxide core-sheath NFs with excellent flexibility via electrospinning followed by calcination in air at 600 °C. The surface morphology of the NFs was investigated by SEM, TEM and EDX analysis. The surface morphology of the NF changed with the feed rate of sheath solution during the electrospinning. The prepared NF membranes were used as adsorbent for the removal of RR-120 dye from aqueous solution. Adsorption experiments were conducted changing pH, adsorbent dosage and contact time. The adsorption process was pH dependent, and the equilibrium adsorption data was observed to follow the Langmuir isotherm model, indicating that the process was governed by the homogenous monolayer adsorption. The maximum adsorption capacity of 1860.81 mg/g was obtained for the NF membrane of CS-2 in which small iron oxide nanoparticles were densely arranged to form a thick and porous sheath layer. This adsorption capacity was the highest for RR-120 exhibited

by an adsorbent ever reported in the literature. Thermodynamic parameters revealed that the sorption process was spontaneous and endothermic. The intraparticle diffusion model was found to be suitable for describing the kinetics of RR-120 dye adsorption. After adsorption, most of the dyes could be recovered from the dye-loaded membranes, and the NF membranes could be regenerated and reused as adsorbent. Consequently, the alumina-silica/iron oxide core-sheath NF membranes could be considered as exceptionally promising nanoadsorbents for the removal and recovery of RR-120 dye form wastewaters.

References

Absalan, G., Asadi, M., Kamran, S., Sheikhian, L., & Goltz, D. M. (2011). Removal of reactive red-120 and 4-(2-pyridylazo) resorcinol from aqueous samples by Fe_3O_4 magnetic nanoparticles using ionic liquid as modifier. *Journal of Hazardous Materials,* 192, 476–484.

Agcaoili, A. R., Herrera, M. U., Futalan, C. M., & Balela, M. D. L. (2017). Fabrication of polyacrylonitrile-coated kapok hollow microtubes for adsorption of methyl orange and Cu (II) ions in aqueous solution. *Journal of the Taiwan Institute of Chemical Engineers,* 78, 359–369.

Alinsafi, A., Khemis, M., Pons, M. N., Leclerc, J. P., Yaacoubi, A., Benhammou, A., & Nejmeddine, A. (2005). Electro-coagulation of reactive textile dyes and textile wastewater. *Chemical Engineering and Processing,* 44, 461–470.

Arica, M. Y., & Bayramoglu, G. (2007). Biosorption of reactive red-120 dye from aqueous solution by native and modified fungus biomass preparations of Lentinus sajorcaju. *Journal of Hazardous Materials,* 149, 499–507.

Badruzzaman, M., Westerhoff, P., & Knappe, D. R. U. (2004). Intraparticle diffusion and adsorption of arsenate onto granular ferric hydroxide (GFH). *Water Research,* 38, 4002–4012.

Bajpai, S. K., & Jain, A. (2010). Sorptive removal of crystal violet from aqueous solution using spent tea leaves: Part I optimization of sorption conditions and kinetic studies. *Acta Chimica Slovenica,* 57, 751–757.

Bazrafshan, E., Mostafapour, F. K., Hosseini, A. R., Khorshid, A. R., & Mahvi, A. H. (2013). Decolorisation of reactive red 120 dye by using single-walled carbon nanotubes in aqueous solutions. *Journal of Chemistry,* 2013, 938374. http://dx.doi.org/10.1155/2013/938374

Celekli, A., İlgün, G., & Bozkurt, H. (2012). Sorption equilibrium, kinetic, thermodynamic, and desorption studies of reactive red 120 on Chara contraria. *Chemical Engineering Journal,* 191, 228–235.

Celekli, A., Yavuzatmaca, M., & Bozkurt, H. (2010). Modelling for removing of reactive red 120 on pistachio husk. *Clean: soil, air, water,* 38, 173–180.

Chakrabarty, P. K., Chatterjee, M., Naskar, M. K., Siladitya, B., & Ganguli, D. (2001). Zirconia fibre mats prepared by a sol-gel spinning technique. *Journal of the European Ceramic Society,* 21, 355–361.

Cheunga, W. H., Szeto, Y. S., & McKay, G. (2007). Intraparticle diffusion processes during acid dye adsorption onto chitosan. *Bioresource Technology,* 98, 2897–2904.

Chatterjee, S., Chatterjee, S., Chatterjee, B. P., Das, A. R., & Guha, A. K. (2005). Adsorption of a model anionic dye, eosin Y, from aqueous solution by chitosan hydrobeads. *Journal of Colloid and Interface Science*, 288, 30–35.

Cheng, G., Sun, M., Ge, X., Ou Y., Xu, X., Lin Q., & Lou, L. (2017). Adsorption-desorption characteristics of nonylphenol on two different origins of black carbon. *Water, Air, & Soil Pollution,* 228(8), 228–311.

Errais, E., Duplay, J., Darragi, F., M'Rabet, I., Aubert, A., Huber, F., & Morvan, G. (2011). Efficient anionic dye adsorption on natural untreated clay: kinetic study and thermodynamic parameters. *Desalination,* 275, 74–81.

Fytianos, K., Voudrias, E., & Kokkalis, E. (2000). Sorption-desorption behavior of 2,4-dichlorophenol by marine sediments. *Chemosphere,* 40, 3–6.

Ghaedi, M., Sadeghian, B., Pebdani, A. A., Sahraei, R., Daneshfar, A., & Duran, C. (2012). Kinetics, thermodynamics and equilibrium evaluation of direct yellow 12 removal by adsorption onto silver nanoparticles loaded activated carbon. *Chemical Engineering Journal,* 187, 133–141.

Haitham, K., Razak, S., & Nawi, M. A. (2014). Kinetics and isotherm studies of methyl orange adsorption by a highly recyclable immobilized polyaniline on a glass plate. *Arabian Journal of Chemistry,* http://dx.doi.org/10.1016/j.arabjc.2014.10.010

Hameed, B. H., Ahmad, A. A., & Aziz, N. (2009). Adsorption of reactive dye on palm-oil industry waste: equilibrium, kinetic and thermodynamic studies. *Desalination,* 247, 551–560.

Han, S., Liu, K., Hu, L., Teng, F., Yu, P. & Zhu Y. (2017). Superior adsorption and regenerable dye adsorbent based on flower-like molybdenum disulfide nanostructure. *Scientific Reports,* 7, 43599. doi:10.1038/srep43599

Ho, Y. S., & McKay, G. (1998). Sorption of dye from aqueous solution by peat. *Chemical Engineering Journal,* 70, 115–124.

Hou, H., Zhou, R., Wu, P., & Wu, L. (2012). Removal of Congo red dye from aqueous solution with hydroxyapatite/chitosan composite. *Chemical Engineering Journal,* 211–212, 336–342.

Hu, J., Song, Z., Chen, L., Yang, H., Li, J., & Richards, R. (2010). Adsorption properties of MgO (111) nanoparticles for the dye pollutants from wastewater. *Journal of Chemical & Engineering Data,* 55, 3742–3748.

Joya, M. R., Baron-Jaimez, J., & Barba-Ortega, J. (2013). Preparation and characterization of Fe_2O_3 nanoparticles. *Journal of Physics: Conference Series,* 466, 012004. doi:10.1088/1742-6596/466/1/012004

Khan, M. M. R., Mukhlish, M. Z. B., Mazumder, M. S. I., Ferdous, K., Prasad, D. M. R., & Hassan, Z. (2014). Uptake of Indosol Dark-blue GL dye from aqueous solution by water hyacinth roots powder: adsorption and desorption study. *International Journal of*

Environmental Science and Technology, 11, 1027–1034.

Kharaisheh, M. A. M., Al-Degs, Y. S, Allen, S. T., & Ahmad, M. N. (2002). Elucidation on controlling steps of reactive dye adsorption on activated carbon. *Industrial & Engineering Chemistry Research,* 41, 1651–1657.

Khosravi, M., & Azizian, S. (2014). Adsorption of anionic dyes from aqueous solution by iron oxide nanospheres. *Journal of Industrial and Engineering Chemistry,* 20 (4), 2561–2567.

Kiefer, E., Sigg, L., & Schosseler, P. (1997). Chemical and spectroscopic characterization of algae surfaces. *Environmental Science & Technology,* 31, 759–764.

Kumar, E., Bhatnagar, A., Ji, M., Jung, W., Lee, S. H., Kim, S. J., Lee, G., Song, H., Choi, J. Y., Yang, J. S. & Jeon, B. H. (2008). Defluoridation from aqueous solutions by granular ferric hydroxide (GFH). *Water Research,* 43(2), 490–498.

Lagergren, S. (1898). About the theory of so-called adsorption of soluble substance. *Kungliga Svenska Vetenskapsakademiens, Handlingar,* 24, 1–39.

Langmuir, I., (1916). The constitution and fundamental properties of solids and liquids. *Journal of the American Chemical Society,* 8, 2221–2295.

Li, W., Zhu, A., Stewart, A., Liu, Z., Cheng, Y.-B., Zhao, Z., & He, H. (2016). Solvent effects on adsorption kinetics, dye monolayer, and cell performance of porphyrin-sensitized solar cells. *RSC Advances,* 6, 114037–114045.

Li, H., Li, W., Zhang, Y., Wang, T., Wang, B., Xu, W., Jiang, L., Song, W., Shu, C., & Wang, C. (2011). Chrysanthemum-like [small alpha]-FeOOH microspheres produced by a simple green method and their outstanding ability in heavy metal ion removal. *Journal of Materials Chemistry,* 21, 7878–7881.

Mahapatra, A., Mishra, B. G., & Hota, G. (2013). Adsorptive removal of congo red dye from wastewater by mixed iron oxide–alumina nanocomposites. *Ceramics International,* 39, 5443–5451.

McKay G. (1981). Design models for adsorption systems in wastewater treatment. *Journal of Chemical Technology* and *Biotechnology,* 31, 717–731.

Morris, M. C., McMurdie, H. F., Evans, E. H., Paretzkin, B., Parker, H. S., & Panagiotopoulos, N. C. (1981). Standard X-ray Diffraction Powder Patterns, Section 18, *International Centre for Diffraction Data,* p. 37.

Motlagh, M. M., Hassanzadeh-Tabrizib, S. A., & Saffar-Teluri, A. (2014). Influence of Mn_2O_3 content on the textural and catalytic properties of $Mn_2O_3/Al_2O_3/SiO_2$ nanocatalyst. *Ceramics International,* 40, 16177–16181.

Moussavi, G., & Mahmoudi, M. (2009). Removal of azo and anthraquinone reactive dyes from industrial wastewaters using MgO nanoparticles. *Journal of Hazardous Materials,* 168, 806–812.

Mukhlish, M. Z. B., Horie, Y. & Nomiyama, T. (2017). Flexible alumina-silica nanofibrous membrane and its high adaptability in reactive red-120 dye removal from water. *Water Air Soil Pollut,* 228: 371. https://doi.org/10.1007/s11270-017-3546-7

Nethajia, S., Sivasamya, A., Thennarasua, G., & Saravanan, S. (2010). Adsorption of malachite green dye onto activated carbon derived from Borassus aethiopum flower biomass. *Journal of Hazardous Materials,* 181, 271–280.

Netpradit, S., Thiravetyan, P., & Towprayoon, S. (2003). Application of ‘waste’ metal hydroxide sludge for adsorption of azo reactive dyes. *Water Research,* 37, 763–772.

Noorimotlagh, Z., Soltani, R. D. C., Khataee, A., Shahriyar, S., & Nourmoradi, H. (2014). Adsorption of a textile dye in aqueous phase using mesoporous activated carbon prepared from Iranian milk vetch. *Journal of the Taiwan Institute of Chemical Engineers,* 45, 1783–1791.

Patel, S., & Hota, G. (2016). Iron oxide nanoparticle-immobilized PAN nanofibers: synthesis and adsorption studies. *RSC Advances,* 6, 15402–15414.

Paul, J., Rawat, K. P., Sarma, K. S. S., & Sabharwal, S. (2011). Decoloration and degradation of reactive red-120 dye by electron beam irradiation in aqueous solution. *Applied Radiation and Isotopes,* 69, 982–987.

Ramachandran, P., Vairamuthu, R. & Ponnusamy, S. (2011). Adsorption isotherms, kinetics, thermodynamics and desorption studies of reactive orange 16 on activated carbon derived from Ananas comosus (L.) carbon. *ARPN Journal of Engineering and Applied Sciences,* 6 (11), 15–26.

Shi, C., Lv, C., Wu, L., & Hou, X. (2017). Porous chitosan/hydroxyapatite composite membrane for dyes static and dynamic removal from aqueous solution. *Journal of Hazardous Materials,* 338, 241–249.

Tabak, A., Baltas, N., Afsin, B., Emirik, M., Caglar, B., & Eren, E. (2010). Adsorption of reactive red 120 from aqueous solutions by cetylpyridinium-bentonite. *Journal of Chemical Technology* and *Biotechnology,* 85, 1199–1207.

Tan, I. A. W., Ahmad, A. L., & Hameed B. H. (2009). Adsorption isotherms, kinetics, thermodynamics and desorption studies of 2,4,6-trichlorophenol on oil palm empty fruit bunch-based activated carbon. *Journal of Hazardous Materials,* 164, 473–482.

Tchieda, V. K., D'Amato, E., Chiavola, A., Parisi, M., Chianese, A., Amamra, M., & Kanaev, A. (2016). Removal of arsenic by alumina: effects of material size, additives, and water contaminants. *Clean Soil Air Water,* 44 (5), 451–586.

Uddin, M. T., Islam, M. A., Mahmud, S., & Rukanuzzaman, M. (2009). Adsorptive removal of methylene blue by tea waste. *Journal of Hazardous Materials,* 164, 53–60.

Weber, T. W., & Chakkravorti, R. K. (1974). Pore and solid diffusion models for fixed bed adsorbers. *American Institute of Chemical Engineers Journal*, 20, 228–238.

Weber, W. J., & Morris, J. C. (1963). Kinetics of adsorption on carbon from solutions. *Journal Sanitary Engeering Division Proceedings. American Society of Civil Engineers,* 89, 31–60.

Wei, C., Song, X., Wang, Q., & Hu Z. (2017). Sorption kinetics, isotherms and mechanisms of PFOS on soils with different physicochemical properties. *Ecotoxicology and Environmental Safety,* 142, 40–50.

Xu, G.-R., Wang, J.-N., & Li, C.-J. (2012). Preparation of hierarchically nanofibrous membrane and its high adaptability in hexavalent chromium removal from water. *Chemical Engineering Journal*, 198–199, 310–317.

Zafar, M. S., Tausif, M., Mohsin, M., Ahmad, S. W., & Zia-ul-Haq, M. (2015). Potato starch as a coagulant for dye removal from textile wastewater. *Water, Air, & Soil Pollution,* 226, 244, 1–11.

Zamora-Villafranco, E., Barceló-Quintal, I. D., Gomez-Salazar, S., Barceló-Quintal, M., Solís-Correa, H. E., & Soriano-Rodríguez, J. M. (2014). Adsorption kinetics of matter contained in a leachate using eggshell and activated carbon. *Journal of Environmental Protection,* 5, 608–619.

CHAPTER 5

SUMMARY OF THE DISSERTATION

It is now well-known fact that energy production and environmental challenges constitute dominant issues for the 21st century. Consequently, limited fossil fuel resources and strict environmental regulations induce the search for sustainable, efficient and environmentally friendly energy sources. On the other hand, acute problems related to the treatment of hazardous reactive dye contaminated water have emerged as international priority. The current PhD research was focused and aimed on the fabrication of flexible inorganic nanofiber (NF) membranes by electrospinning method, and their successful application to flexible and heat-resistive NF substrate in dye-sensitized solar cells (DSSCs) and adsorptive removal of dye contamination from water.

Chapter 1 consists of a general feature introduction of the entire studies. At first, the background of the studies has been discussed. After that, the history, principle, basic parameters and application of electrospinning technique have been described. In addition, the structure of DSSC as well as research trend on its different parts, working principle of DSSC, and basic principle of adsorption method have been illustrated for the adsorptive removal of dye. Finally, the objectives of the studies have been discussed.

Chapter 2 deals with the fabrication of ITO-silica complex NF mats and their application in DSSC. Two approaches were applied to make the ITO-silica NF mats: electrospun silica NF mats drop coated by ITO and hybrid mats composed of ITO NF and silica NF fabricated by the dual-spinneret electrospinning technique. The self-standing ITO-silica NF mats with excellent flexibility and thermal durability (>400 $^{\circ}$C) were successfully fabricated with the sheet resistance of 15–113 Ω/sq. The ITO-silica NF mats were successfully applied to the thermally stable light-weight substrates to produce working electrodes of DSSCs, and the problems in the existing application were highlighted.

Chapter 3 deals with the fabrication of nonwoven membrane of ultrafine alumina-silica NFs and its high adaptability for the removal of Reactive Red-120 (RR-120) dye pollutant from aqueous solution. We have successfully prepared the NF membrane by electrospinning, and also characterized the membrane by using by TG-DSC, FE-SEM, EDX, XRD and Raman spectroscopy. The membrane, consisting of continuous and randomly arranged NFs with an average diameter of ~ 95 nm, was self-standing, amorphous, and mechanically flexible. Batch experiments for the removal of RR-120 dye from the aqueous

solution were carried out changing pH, adsorbent dosage and contact time. Adsorption equilibrium and kinetic studies were also carried out. The sorption process was pH dependent and followed the Langmuir isotherm model. The maximum adsorption capacity of the NF membrane for RR-120 dye was observed as high as 884.95 mg/g. After the adsorption, the membrane could be separated from the liquid phase conveniently due to its flexible and self-standing nature. Moreover, most of the dye could be recovered from the dye-loaded membrane and the NF membrane could be reused as adsorbent. Consequently, this membrane can be a practically applicable promising adsorbent material for the removal and recovery of dye from the aqueous solution.

Chapter 4 illustrates the preparation of alumina-silica/iron oxide core-sheath nanofiber membranes and their enhanced adsorption performances. The core-sheath nanofiber membranes with net-like porous structure were successfully prepared by electrospinning method. The sorption characteristics of RR-120 dye from aqueous solution were investigated as the same manner with alumina-silica NF membrane. The equilibrium study revealed that one of the alumina-silica/iron oxide NF membranes had a maximum RR-120 dye sorption capacity of 1860.81 mg/g, and this was the highest adsorption capacity for RR-120 exhibited by an adsorbent ever reported in the literature. Moreover, most of the dyes could be recovered from the dye-loaded membranes after adsorption and the membranes could be reused as adsorbent. Thus, the alumina-silica/iron oxide NFs membranes are practically applicable potential adsorbent for the removal of RR-120 dye.

ACKNOWLEDGEMENTS

I would like to express my sincere gratitude to a number of people who have been involved, directly or indirectly to conduct this research work. First of all I would like to thank the Ministry of Education, Culture, Sports, Science and Technology (MONBUKAGAKUSHO) of the Japanese Government for providing MEXT Scholarship to carry out my PhD. This work was supported by JSPS KAKENHI Grant Numbers 23360042 and 16K04901. I would sincerely like to show gratitude to my supervisor Professor Dr. Yuji Horie, Department of Electrical and Electronics Engineering, Kagoshima University, Japan, for giving me the valuable opportunity to come to Kagoshima University as a PhD student to his laboratory. I sincerely thank my supervisor for his continuous support, encouragement, and insightful guidance during the course of my doctoral studies. I enjoyed working with him and learned a lot from his broad knowledge and vast experience. I express my heartfelt respect and deepest sense of gratitude to my research co-supervisors Professor Dr. Norio Terada and Professor Dr. Toshifumi Yoshidome, Kagoshima University, for their valuable suggestions and inspiration, useful discussions and constructive criticisms during the research tenure. I would like to give special thank to Assistant Professor Teruaki Nomiyama of our laboratory for his encouragement, support and suggestion during my research work. I would like to thank former and present co-workers of our laboratory, especially Kousei Higashi and Akimasa Ichigi for their kind help and supports. In a general manner I would like to thank all members of our laboratory for their generosity and cooperation, and for maintaining a very friendly environment in the laboratory. I deeply thank my parents for their unconditional love, support and prayer, without which I would not have been able to succeed in this endeavor. I would like to express my heartfelt love and gratitude to my brothers, sister, brother-in-law, father-in-law, mother-in-law and other relatives for their prayer and encouragement to carry out this research work in aboard. Finally, I thank my wife for her incredible understanding and patient during my PhD work.

LIST OF PUBLICATIONS

1. Mukhlish, M. Z. B., Horie, Y., Higashi, K., Ichigi, A., Guo, S., & Nomiyama, T., (2017). Self-standing conductive ITO-silica nanofiber mats for use in flexible electronics and their application in dye-sensitized solar cells. *Ceramics International,* 43, 8146–8152.

2. Mukhlish, M. Z. B., Horie, Y. & Nomiyama, T. (2017). Flexible alumina-silica nanofibrous membrane and its high adaptability in reactive red-120 dye removal from water. *Water Air Soil Pollut,* 228: 371. https://doi.org/10.1007/s11270-017-3546-7

3. Guo, S., Horie, Y., Imada, S., Mukhlish, M. Z. B., & Nomiyama, T. (2017). Enhancement of carrier-collection by electrospun Nb-doped TiO_2 nanofiber-network in photoelectrode of dye-sensitized solar cells. *Journal of Materials Science: Materials in Electronics*, 28, 13084–13093.

CONFERENCE PRESENTATIONS

1. Mukhlish, M. Z. B., Horie, Y., Ichigi, A., & Nomiyama, T. (2017). Flexible alumina nanofibrous membrane and its high adaptability in reactive red-120 dye removal from aqueous solution. The 15th International Conference on Advanced Materials (IUMRS-ICAM 2017), August 27–September 01, 2017 at Kyoto, Japan. A8-P28-010

2. Mukhlish, M. Z. B., Horie, Y., Higashi, K., A., & Nomiyama, T. (2016). Application of self-standing conductive Silica-ITO nanofiber mat to dye sensitized solar cells. The 63rd JSAP Spring Meeting, 2016, March 19 (Sat.)–22 (Tue.), 2016 at Tokyo Institute of Technology, Japan. 20p-P7-14

3. Mukhlish, M. Z. B., Horie, Y., Higashi, K., A., & Nomiyama, T. (2015). Electrospinning and characterization of flexible self-standing alumina-silica ceramic nanofibers and their application. The 25th Annual Meeting of MRS-J, 2015, December 8 (Tue.)–10 (Thu), 2015 at Yukohama, Japan. A1-P8-008

4. Ichigi, A., Mukhlish, M. Z. B., Horie, Y., & Nomiyama, T. (2017). Electrospun ITO-SiO_2 nanofiber mat for flexible conductive substrate. The 15th International

Conference on Advanced Materials (IUMRS-ICAM2017), August 27–September 01, 2017 at Kyoto, Japan. D4-P30-013

5. 一木 晃雅, Mukhlish, M. Z. B., 東 宏誠, 野見山 輝明, 堀江 雄二(2016). ITO-SiO_2 複合ナノファイバ不織布の色素増感太陽電池への応用, (2016) 応用物理学会九州支部学術講演会 講演予稿集 3Aa-6